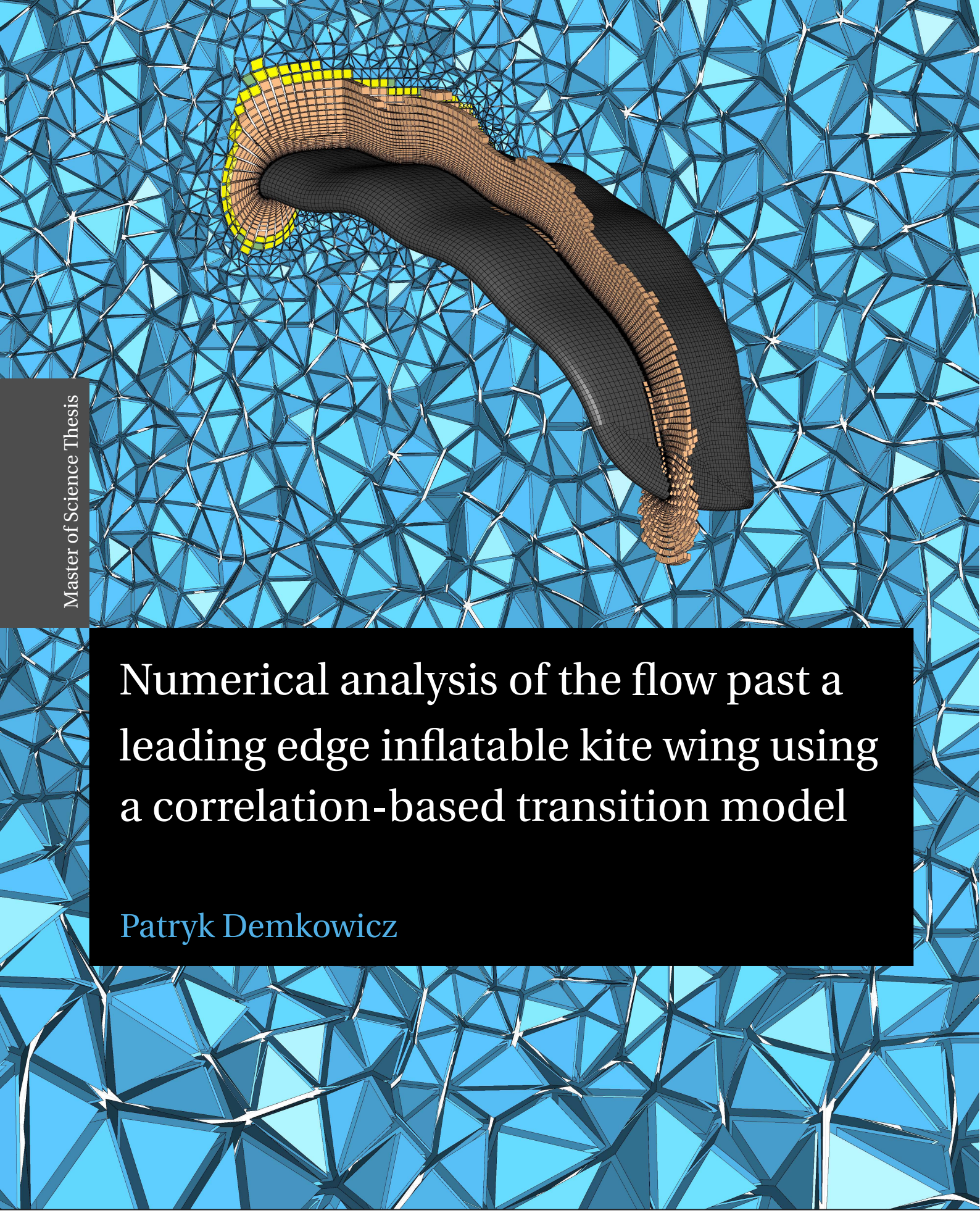

Master of Science Thesis

Numerical analysis of the flow past a leading edge inflatable kite wing using a correlation-based transition model

Patryk Demkowicz

Aerodynamics

Faculty of Aerospace Engineering

TU Delft

Delft University of Technology

Numerical analysis of the flow past a leading edge inflatable kite wing using a correlation-based transition model

Master of Science Thesis

To obtain the degree of Master of Science in Aerospace Engineering
at Delft University of Technology

Patryk Demkowicz

December 19, 2019

Wind Energy Group, Faculty of Aerospace Engineering, Delft University of Technology

Delft University of Technology

DELFT UNIVERSITY OF TECHNOLOGY
DEPARTMENT OF AERODYNAMICS

The undersigned hereby certify that they have read and recommend to the Faculty of Aerospace Engineering for acceptance the thesis entitled **"Numerical analysis of the flow past a leading edge inflatable kite wing using a correlation-based transition model"** by **Patryk Demkowicz** in fulfillment of the requirements for the degree of **Master of Science**.

Dated: December 19, 2019

Supervisors:

Dr. ir. A. Viré

Dr.-Ing. R. Schmehl

Dr. ir. A. H. van Zuijlen

MSc. M. Folkersma

Preface

I would like to thank my supervisor Dr. ir. Axelle Viré for introducing me to the topic and for all the guidance and help she provided me from start to finish of my thesis work. I would also like to express my gratitude to Dr.-Ing. Roland Schmehl for continuous support, numerous thoughtful discussions and especially for helping me finalise the report.

Thank you Mikko for patiently answering my endless streams of questions about meshing, carrying out the simulations and post-processing. Your input really did accelerate my progress significantly.

Special thanks to Valentin and Yuyang for the countless discussions and regular conversations we have had over the past year. Finally, I would also like to thank my sister and my parents for supporting my decisions and always being there.

Summary

Thorough understanding of flexible wing structural and aerodynamic properties is crucial to reduce uncertainties in the design process of energy generating kite systems. A flexible leading edge inflatable (LEI) tethered kite connected to a drum-generator module is currently being developed by the Airborne Wind Energy research group at TU Delft jointly with its commercial spin-off Kitepower. During each energy generation cycle, the kite experiences persistent regions of flow separation, which combined with the bowed shape of the kite and its low aspect ratio cause multiple 3D flow phenomena. Furthermore, a kite is a lightweight and flexible structure and there exists very strong coupling between the aerodynamic loads and its structural dynamics, forming an intricate aeroelastic problem.

Due to computational limitations of today's hardware, it is difficult and expensive to numerically solve the coupled aeroelastic problem in detail. As such, the focus of this thesis is to resolve and characterise one side of the problem, which is the LEI kite aerodynamics. Kitepower LEI V3A kite, modelled as a rigid geometry, has been analysed for various Reynolds numbers and angles of attack using a steady-state Computational Fluid Dynamics solver. A high quality, hybrid mesh has been generated. The $\gamma - \widetilde{\mathrm{Re}}_{\theta t}$ transition model has been used to improve the accuracy of the results at low Reynolds numbers and to assess the significance of transition at high Reynolds numbers.

Obtained force coefficients for a range of angles of attack are in general agreement with the values used in existing numerical models and measurements from experiments. The results indicate that flow transition is important to take into account for Reynolds numbers at least up to 3 million in order to accurately predict the stall angle. Large amounts of cross flow have been observed over the span of the kite that may affect the integral drag coefficient. The employed methodology is only applicable to the traction phase of the pumping cycle, as the steady-state and rigid geometry assumptions do not hold during the retraction phase, where the kite experiences severe deformation.

Table of Contents

List of Figures

List of Tables

Nomenclature

Abbreviations

AWE	Airborne Wind Energy
CAD	Computer Aided Design
CFD	Computational Fluid Dynamics
DNS	Direct Numerical Simulation
FSI	Fluid-Structure Interaction
GAMG	Geometric Agglomerated Algebraic Multigrid
HAWT	Horizontal Axis Wind Turbine
KCU	Kite Control Unit
LE	Leading Edge
LEI	Leading Edge Inflatable
LES	Large Eddy Simulation
NURBS	Non-Uniform Rational Basis Spline
RANS	Reynolds-Averaged Navier-Stokes
SIMPLE	Semi-Implicit Method for Pressure Linked Equations
SST	Shear Stress Transport
TE	Trailing Edge
URANS	Unsteady Reynolds-Averaged Navier-Stokes
VLM	Vortex Lattice Method

Greek Symbols

α	Angle of attack	$[^\circ]$
μ	Dynamic viscosity	$[kg\ m^{-1}\ s^{-1}]$
ν	Kinematic viscosity	$[m^2\ s^{-1}]$
ν_T	Eddy viscosity	$[m^2\ s^{-1}]$
ρ	Density	$[kg\ m^{-3}]$

τ_w	Wall shear stress	$[kg\ m^{-1}\ s^{-2}]$

Latin Symbols

A_{eff}	Effective area of the bridle line system	$[m^2]$
A_{ref}	Reference area	$[m^2]$
C_D	Drag coefficient	$[-]$
$C_{Dbridle}$	Drag coefficient of the bridle line system	$[-]$
C_{Dcyl}	Drag coefficient of a cylinder	$[-]$
$\widehat{C}_D$	Normalised drag coefficient	$[-]$
C_{Dp}	Parasite drag coefficient	$[-]$
C_f	Skin friction coefficient	$[-]$
C_L	Lift coefficient	$[-]$
$\widehat{C}_L$	Normalised lift coefficient	$[-]$
c_{ref}	Reference chord	$[m]$
d	Bridle line diameter	$[m]$
D_{bridle}	Drag force on the bridle line system	$[N]$
k	Turbulent kinetic energy	$[m^2\ s^2]$
L/D	Lift-to-drag ratio, aerodynamic efficiency	$[-]$
L_{tot}	Total length of the bridle line system	$[m]$
p	Pressure	$[kg\ m^{-1}\ s^{-2}]$
Re	Reynolds number	$[-]$
Tu	Turbulence intensity	$[\%]$
u^*	Friction velocity	$[m\ s^{-1}]$
U_i	Velocity of the fluid in the i-direction	$[m\ s^{-1}]$
U_∞	Freestream velocity	$[m\ s^{-1}]$
U_n	Velocity component normal to the bridle line system	$[m\ s^{-1}]$
y^+	Non-dimensional wall distance	$[-]$

Chapter 1

Introduction

Energy harvesting through vehicles operating at high altitudes is a very promising concept for electricity generation in the future. This field of wind energy technology is called Airborne Wind Energy (AWE). One of its advantages over conventional horizontal axis wind turbines (HAWT) is the increased wind energy potential at higher altitudes [1]. Since the first concept of airborne devices harvesting energy from the wind was developed in the 1980 [2], numerous development teams around the world continue to explore various designs. Many of those share a common working principle, which is a tethered wing or aircraft connected to a generator. The tethered surface does fast crosswind motions, thus extracting energy from the wind.

One of the possible harvesting concepts is to use a flexible leading edge inflatable (LEI) tethered kite connected to a drum-generator module, which had been developed by the AWE research group at TU Delft jointly with its commercial spin-off Kitepower. The concept is based on an operation of the wing in pumping cycles [3] to generate energy. Optimizing such a system is a complex problem consisting of many variables, and as such requires thorough understanding of the kite's structural and aerodynamic properties. The kite experiences Reynolds numbers of up to tens of millions and persistent regions of flow separation at all angles of attack, while the characteristic kite geometry (low aspect ratio, high anhedral angle) causes significant 3D non-linear flow effects. The flight conditions also dynamically change as the kite is performing various manoeuvres. Since a kite is a lightweight and flexible structure, there exists very strong coupling between the aerodynamic loads and its structural dynamics, forming an intricate aeroelastic problem.

Due to computational limitations of today's hardware, it is difficult and expensive to numerically solve the coupled aeroelastic problem in detail. As such, the focus of this thesis is to resolve and characterise one side of the problem – LEI kite aerodynamics. This objective

is motivated by the lack of reference data for aerodynamics of a LEI kite. The goal is to refine the approach used by Deaves [4] by expanding the methodology used by Folkersma et al [5] to three dimensions and apply it the to Kitepower LEI V3A kite. The main limitations of previous projects include two-dimensional flow representation only, inaccurate flow separation prediction and lack of validation against experimental data. This project aims at applying a correlation-based transition model to a 3D steady-state Reynolds-Averaged Navier-Stokes (RANS) simulation and validating the obtained results against experimental measurements gathered in-situ on a full-scale flying kite [6], thus rectifying the shortcomings of previous works. The results obtained from the simulation will be evaluated in the context of analysis of the 3D non-linear flow phenomena and development of robust methodology for future kite aerodynamic analyses.

The work undertaken to achieve this objective is structured as follows. Chapter 2 presents a literature review on the subject of AWE and explores methodologies used for aerodynamic analysis of kites and flexible membranes in the past. A review of numerical modelling methods and discretisation schemes used in this project is done in Chapter 3. Chapter 4 explains the mesh generation approach, evaluates mesh quality metrics and presents the outcome of the mesh sensitivity study. Simulation results are discussed in detail and compared with literature in Chapter 5. Finally, Chapter 6 summarises conclusions from the work achieved by this thesis and suggests recommendations for future work.

Chapter 2

Literature Review

2.1 Airborne Wind Energy concepts

This section outlines the basics of energy generation using airborne vehicles, their advantages and disadvantages and typical flight conditions experienced by LEI kites. For any further insights the reader is referred to excellent textbooks that cover various aspects of AWE [7, 8].

2.1.1 AWE potential

Energy harvesting by airborne vehicles is a promising concept that is actively being developed by various AWE communities around the world that try to bring the technology into commercial use. The concept demonstrates a few principal advantages over conventional wind turbines that show the immense potential of AWE generation.

The theoretical generation of conventional wind energy applications is already much higher than world's electricity demand [9]. Wind speeds and wind power density generally increase with the altitude [1] and studies have shown that high-altitude airborne devices, collectively, could potentially extract over four times more energy than wind turbines[10]. The overall costs of scaling the AWE systems are expected to be much lower than in case of HAWTs [11], since a massive support structure of a wind turbine is replaced by a tether. Flying kites or energy harvesting drones can fly higher in steadier winds and are much more aerodynamically efficient than wind turbine rotor blades. All those factors lead to up to four times lower energy cost, as well as higher capacity factor and lower intermittency [12], making the power production more uniform and robust. These advantages demon-

strate that high-altitude airborne devices have the unique potential to supplement HAWTs in energy production and eventually become the most reliable abundant renewable energy source.

2.1.2 Crosswind energy generation

The first idea for a tethered device that extracts energy from airborne wind energy was conceived by Loyd in 1980 [2]. His paper describes two concepts for utilizing airborne wind energy using high lift devices – drag power production and lift power production. The drag power is produced by increasing the drag of the kite by equipping it with air turbines, while the lift power is produced by lift force creating tension in the tether and pulling the tether out of a generator located on the ground. In both of these energy production modes it is important to note that the device is steered to perform fast crosswind motions, such that its speed through the air is higher than the wind speed, increasing the forces and power generated. These concepts are visualised on Figure 2.1.

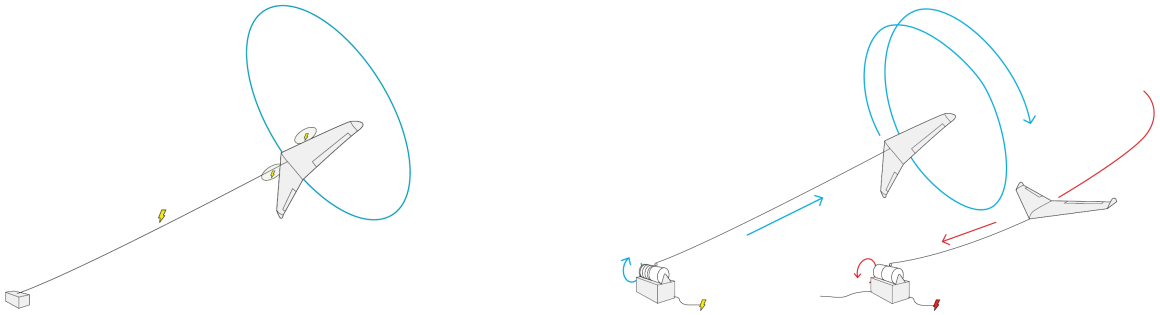

(a) Drag power production.

(b) Lift power production.

Figure 2.1: Visualisation of drag (a) and lift (b) power production concepts developed by Loyd. The lift power cycle consists of tether reel-out and reel-in phases (reproduced from [12]).

The focus of this project is a kite system operating in the lift power production mode with the generator located on the ground. Such a system possesses a few advantages over a system with on-board power generation, such as much lower weight per square meter of the airborne vehicle and no requirement for a high voltage tether. Energy generation in lift mode consists of two phases, namely the traction and retraction phases. The traction phase (also called reel-out phase) is when power production happens. During this phase, the kite is manoeuvred to perform fast crosswind motions at high angles of attack that increase the lift on the kite and tension in the tether, turning the electrical generator. Afterwards, the kite needs to be brought back during the retraction (reel-in) phase, when the kite performs manoeuvres such that the force in the tether is lowered, minimizing the energy investment. It is achieved by lowering the angle of attack and de-powering the kite, thus minimizing the aerodynamic loads [13]. This cycle, called the pumping mode, is then repeated for continued energy generation. Typical energy generation during traction and retraction phases can be seen on Figure 2.2.

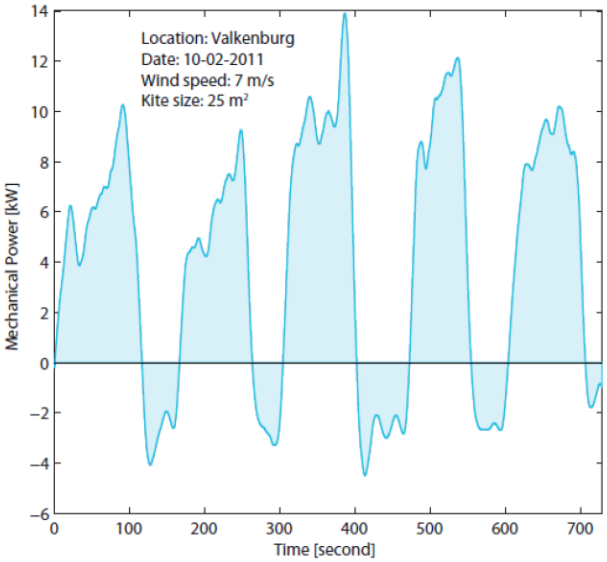

Figure 2.2: Power production during kite pumping mode (reproduced from [13]).

Loyd [2] estimated that under idealised assumptions, the maximum power that can be generated by the kite system is given by:

$$P = \frac{2}{27}\rho A_{ref} U_{\infty}^{3} C_L \left(\frac{C_L}{C_D}\right)^2, \tag{2.1}$$

where ρ is the density of air, A_{ref} is the surface area of the kite, C_L and C_D are lift and drag coefficients of the system, respectively, and U_{∞} is the wind speed. This maximum power occurs when the reel-out velocity of the tether is equal to one third of the wind velocity, $v_{ro} = \frac{1}{3} v_w$ [2]. According to the Eq. (2.1), the power is proportional to the square of lift-to-drag ratio C_L/C_D, and as such it is a very important property of crosswind AWE systems. It is important to note that the tether and bridle lines add significant amount of drag to the system and can even be considered the primary limitation to power production [14]. For detailed calculations regarding limits to energy generation of AWE systems the reader is referred to [15] and [16].

The kite used by the TU Delft Kitepower research group and its commercial spin-off is a LEI kite. It is composed of a canopy, pressurized inflatable tubes forming the leading edge and struts, which increase the structural stiffness. These components, together with the Kite Control Unit (KCU) or the control pod, steering and power lines and the tether are shown on Figure 2.3.

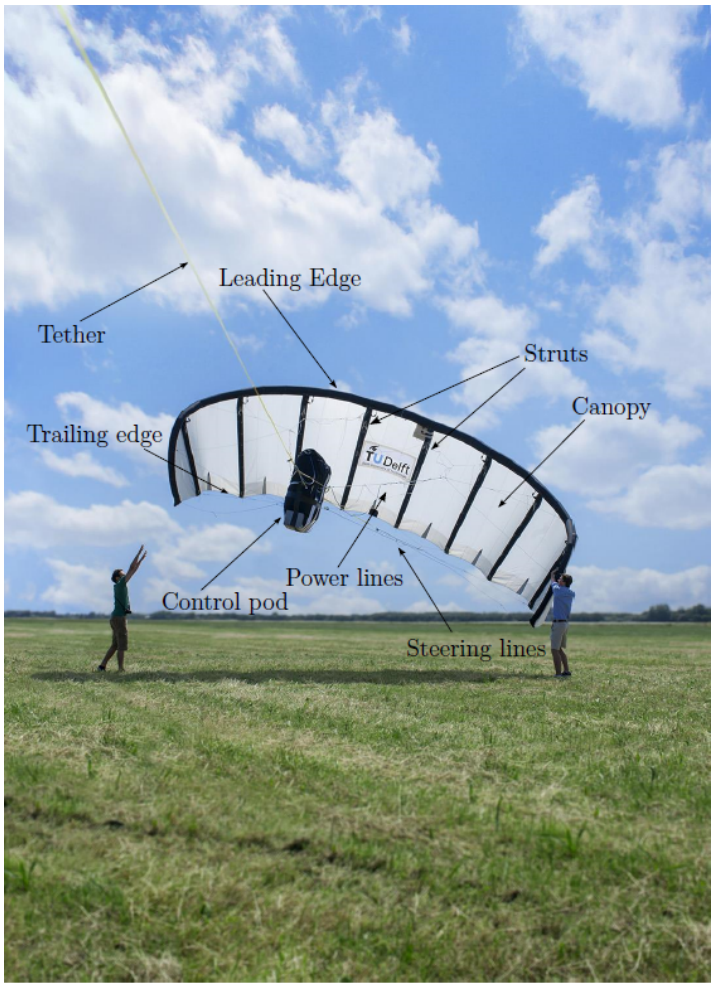

Figure 2.3: Kitepower kite system components (reproduced from [17]).

The KCU is a remote-controlled robot that can alter the geometry of the kite by actuating the bridle lines. Thanks to two integrated electrical winches, the kite geometry can be altered for steering and for angle of attack independently [18]. For example, pulling one of the steering lines makes the kite yaw, due to asymmetric deformation of the kite [3]. Actuating both steering lines symmetrically allows to influence the pitch angle of the kite, altering the angle of attack and its power setting. This is visualized on Figure 2.4. Kites in AWE systems are usually manoeuvred in a figure of eight (see Figure 2.5), which prevents twisting of the kite bridle lines.

2.1.3 Kite conditions during flight

During standard operation kites fly at altitude between 100 and 500 meters throughout the traction and retraction phase and the conditions vary a lot during each cycle [20]. During the traction phase, the apparent wind velocity and Reynolds number are high and the kite

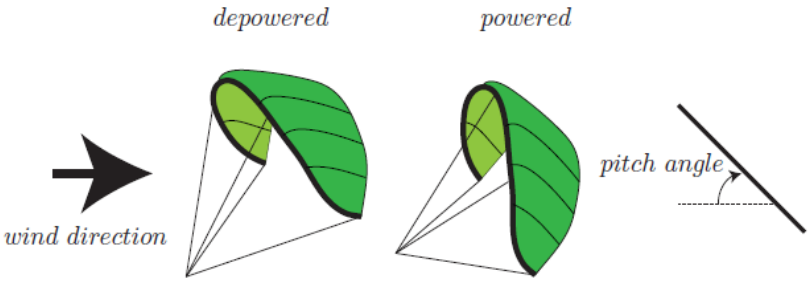

Figure 2.4: Kite power settings adjustable by power and steering lines (reproduced from [19]).

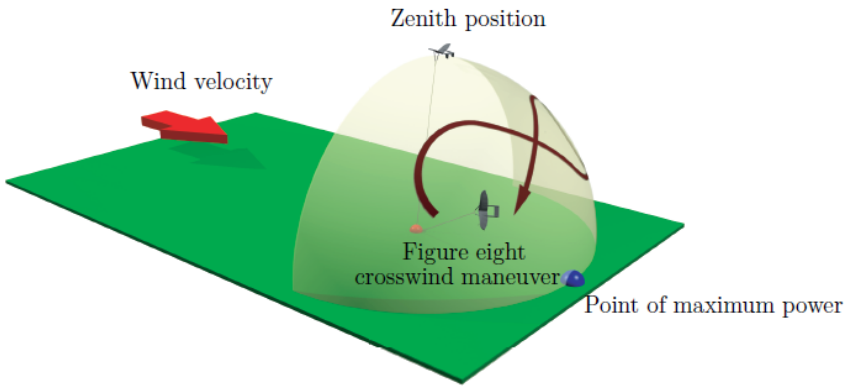

Figure 2.5: Figure of eight crosswind manoeuvre (reproduced from [3]).

is oriented at high angle of attack to maximize the lift and traction force. During retraction phase the kite is depowered and experiences low Reynolds numbers and angles of attack. A study by Ruppert done in 2012 [13] reports very high range of angles of attack during traction phase, up to $30°$, as well as large variations of sideslip angle, up to $\pm 15°$. However, recent experimental results obtained by Oehler et al [6], using in-situ measurements of the relative flow, show that the angle of attack is limited to a small range of $6°$ to $16°$ during the traction phase. The side slip angle is shown to vary by about $\pm 10°$ during sharp turning manoeuvrers only. The differences can be attributed to different definitions of the angle of attack. The in-situ measurements also show apparent flow speeds of about 18 m/s during the traction phase and lower than 15 m/s during the retraction phase. This indicates typical chord-based Reynolds number range of less than 1 million to about 8 million for LEI kites of 20-30 m^2 flat surface area.

Another variable that varies during cyclic operation is the relative power setting, which describes the symmetric actuation of the rear suspension lines of the kite [6]. Its maximum is 1, obtained during the traction phase and drops to below 0.55 during retraction phase, as seen on Figure 2.6. It can be observed that lift-to-drag ratio is generally higher during traction phase than during retraction phase, due to higher angle of attack and power setting. It has been shown through experimental studies that aerodynamic coefficients of a

LEI kite depends on many variables [21], not only on the angle of attack, as in case of rigid airfoils. The dependency of lift-to-drag ratio on angle of attack is shown on Figure 2.7. The periodic drops in lift-to-drag ratio observed on Figure 2.6 can be associated with steering manoeuvres and deformation of the kite, inducing additional drag force [22].

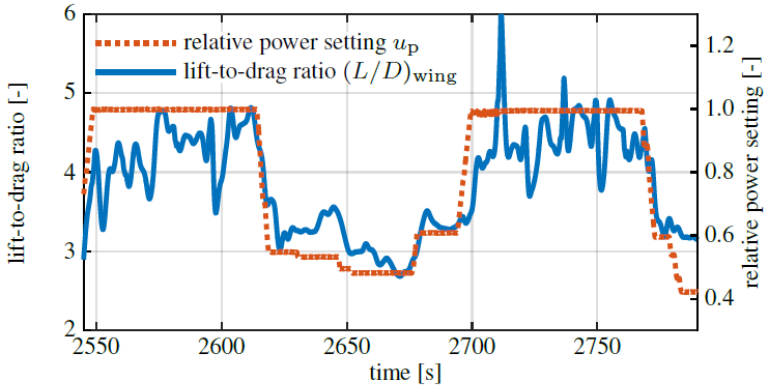

Figure 2.6: Relative power setting and lift-to-drag ratio during pumping cycle (reproduced from [6]).

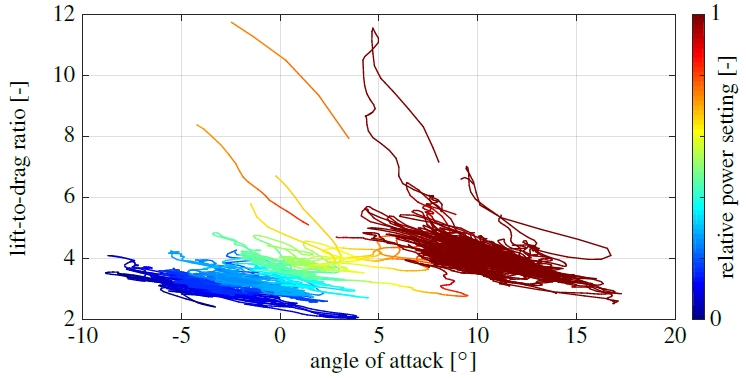

Figure 2.7: Lift-to-drag ratio as a function of angle of attack (reproduced from [6]).

From this information it is clear that energy harvesting kite system is a very complex problem, in both aerodynamic and mechanical sense. The kite performs various manoeuvrers during flight that drastically alter its flight conditions in a periodic manner. It also undergoes frequent deformation which influences its aerodynamic properties. Optimizing power generation is a complicated problem involving many variables. Aerodynamics of a kite system depend on kite projected area, lift-to-drag ratio, maximum wing loading, depower capability and tether drag. The mechanical performance of the system is additionally influenced by system and cycle efficiency, reel-out and reel-in speeds, average height of the kite during reel-out, tether elevation angle, wind speed and many other variables. For detailed study on kite system efficiency the reader is referred to [23].

2.2 Kite aerodynamic analyses

The airfoil of the LEI kite is composed of an inflated tube acting as a leading edge, and a thin canopy. Such a structure, with circular leading edge and a flexible membrane, is called a sailwing. Flexible sailwings have been extensively studied since early 1960s [24]. Many wind tunnel tests investigated the lift, drag and stability characteristics of sailwings [25] and it was found that they can achieve lift-to-drag ratios as high as rigid wings. Their circular leading edge would lead to higher lift coefficient at a cost of reduced lift-to-drag ratio.

The sailwing airfoil is an aerodynamically complex problem, since even though the flow on the suction side remains similar to a conventional airfoil, the leading edge tube will create a recirculation zone on the pressure side (see Figure 2.8). Moreover, the effect of boundary layer transition on LEI kite airfoils is unclear and poses another challenge to aerodynamic modelling of the kite. A cylinder is known to experience drag crisis, which happens when its total drag coefficient significantly decreases with increased Reynolds number [26]. This phenomenon can be relevant to LEI kite aerodynamics, since boundary layer transition on the circular leading edge may affect the size of the recirculation zone on the pressure side. Given the airfoil shape and typical Reynolds numbers experienced by the kite, the flow separation can occur from a laminar boundary layer on the suction side [5]. Bot et al [27] showed recently that at low angles of attack the lift force may abruptly change due to a slight change in the Reynolds number. Similarly to drag crisis, this phenomenon (named lift crisis) is associated with flow separation, and is dependent on whether the flow separates off the laminar or turbulent boundary layer.

Although the literature concerning aerodynamics of kites is very scarce, the theory of flows around flexible membranes has been thoroughly studied over the past few decades. In some applications, such as yacht sails or ram air wings, the flow conditions are very similar to what an LEI kite experiences during the pumping cycle – frequent flow separations, high angles of attack and strong fluid-structure coupling. This makes the sail theory relevant to LEI kite application for energy harvesting and will be included in the following sections, which review methods that were applied to flows over flexible membranes in the past.

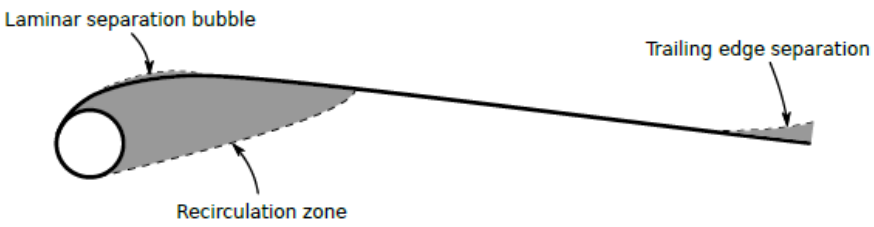

Figure 2.8: Typical flow around LEI kite airfoil (reproduced from [5]).

2.2.1 Lookup table based models

The simplest and fastest model for kite aerodynamics was developed by Fechner et al [22]. The kite geometry is divided into three separate surfaces. The state of the kite is determined and corresponding aerodynamic coefficients on each surface are then related from empirically determined lookup tables. The model can be used to predict kite flight paths and the values in the lookup tables are corrected so that the model results align with given experimental results. As such this method cannot be reliably used during a kite design stage.

A more advanced lookup table based model has been developed by Breukels [3]. It is a parametric model where the kite is divided into a number of 2D cross sections. The aerodynamic properties of these cross sections are then determined by an algorithm that uses camber, angle of attack and airfoil thickness to output local lift, drag and moment coefficients. Those output values are based on lookup tables consisting of results obtained from 2D RANS simulations that were ran beforehand. Next, the integral aerodynamic forces are computed and distributed over six nodes of the 2D cross section (see Figure 2.9) by means of fairly arbitrary weighting functions. These functions are said to approximate the force distribution of a generic kite and have been validated against two actual kites. Using the same set of weighting functions during a design phase of a new kite is questionable.

Breukels also implemented a correction for 3D effects that is based upon a vortex lattice method (VLM) analysis of an arbitrary kite. It relies on the premise of linear lift curve slope and the assumption that airfoil shape does not influence the relation between anhedral angle and the lift curve slope [3]. Unfortunately such assumptions are not realistic for a kite experiencing high angles of attack, near-stall conditions and large deformations. Bosch used Breukels model to solve a kite aeroelastic problem and has pointed out a few major flaws of the model [19]. The 3D correction has not been included in his approach as Bosch stated that "Discussions with the author of the model led to the conclusion that the uncertainty of the three dimensional correction is so significant that it is not clear whether this correction actually improves the model or not." [19]

2.2.2 Potential flow methods

Potential flow methods assume that the flow is irrotational, often coupled with the assumption of the fluid being inviscid and incompressible. These methods are very computationally efficient, however they exhibit a few major shortcomings, such as inability to account for the presence of boundary layer or flow separation. For a detailed overview of various potential flow methods the reader is referred to an in-depth textbook of Katz and Plotkin [28].

A large part of the early yacht sail theory is described using the assumptions of irrotational,

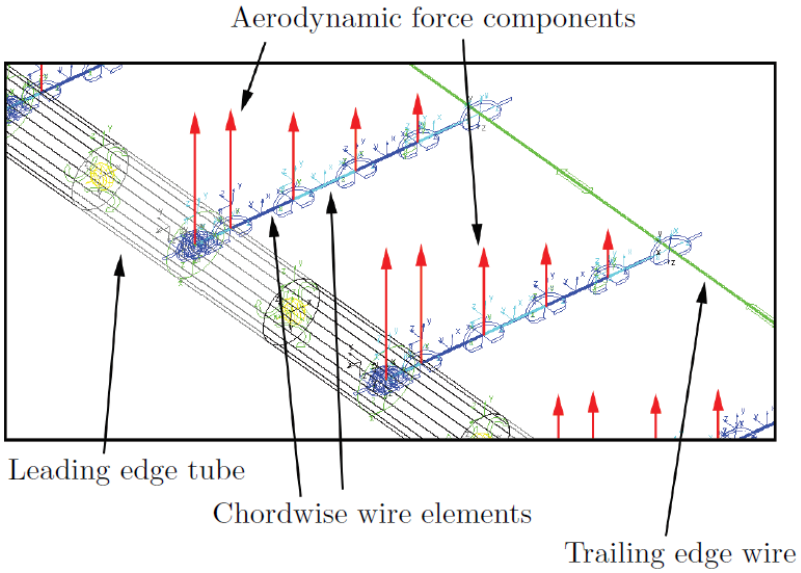

Figure 2.9: Aerodynamic forces distribution in Breukels' model (reproduced from [3]).

inviscid flow and the thin airfoil theory. Thwaites combined these assumptions with static equilibrium to set foundations for the sail equation in the early 1960s [29]. Early studies on three dimensional sail aeroelastics utilised lifting line theory and vortex lattice methods [30]. Mendenhall et al [31] performed an analysis on the performance of parawings using lifting surfaces and 2D strip theory. It showed that the methods struggled with representing 3D effects and predicting flow separation accurately at high angles of attack.

In light of those limitations, many potential flow approaches has been enhanced to account for some of the viscous effects, typically through implementation of a viscous correction. Fiddes and Gaydon [32] used 3D free wake vortex lattice method combined with integral boundary layer method to correct for viscous effects on yacht sails. Lorillu et al [33] developed a potential flow method with a Helmholtz thick wake model to aid prediction of the flow separation on 2D yacht sails. The resultant sail shape and free streamline computed with this approach were in good agreement with experimental Particle Image Velocimetry data, for both attached and separated flows. Graf et al [34] used a lifting line method combined with lift and drag airfoil data obtained through 2D RANS simulations for analysis of wing sails. Lifting line method was used to model three dimensional flow phenomena, while 2D RANS investigations accounted for induced drag. Comparison of the results to 3D RANS showed that for attached flows the agreement is very good, but for larger angles of attack the lift becomes overpredicted and solution can become unstable. Similarly, Vimalakanthan et al [35] used non-linear lifting line model and free vortex code combined with polar data obtained from 2D numerical simulations for power prediction analysis of an energy harvesting airplane.

Potential flow methods have also been applied to flows around kites. Work by Guanaa et al [36] presents a method for determining aerodynamic performance of kites by using VLM to model physical effects of the flow and coupling it with angle of attack shift to determine the viscous lift coefficient. The method achieved good agreement with a 3D RANS simulation of a simplified kite geometry, especially for attached flow (see Figure 2.10). Similarly to other studies including potential flow methods, the correlation worsens as the flow becomes stalled. Leuthold [37] investigated aerodynamics of 3D LEI kite geometry using a quasi-steady multiple wake vortex lattice method and compared the results to experimental measurements, 3D lifting line model and 3D RANS simulations of relevant test cases. It was found that the model struggles to predict flow reattachment correctly, which unfortunately is very common to occur on LEI kite during its flight. Similar problems related to flow separation modelling have been encountered by Mandru [38], who developed a double wake model for 2D kite airfoils.

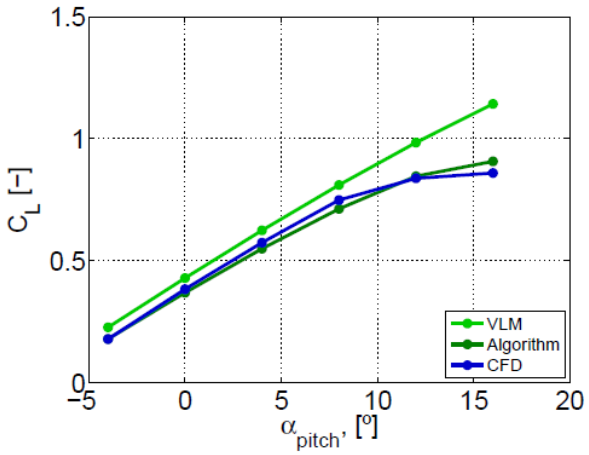

Figure 2.10: Comparison of lift coefficient simulated by regular VLM, 3D CFD and Algorithm (VLM with viscous correction), as obtained by Gaunaa et al [36].

2.2.3 Navier-Stokes methods

In light of the limitations of the potential flow methods outlined in the previous section, researchers have been investigating other, more complex computational methods with desire to capture the flow separation and other viscous effects properly. One of the common methods in today's engineering applications are computational methods based on viscous Navier-Stokes equations, called Computational Fluid Dynamics (CFD). One of the earliest applications of CFD to flexible membranes was the work done by Smith in 1994 [39], who performed a numerical analysis of unsteady 2D flow over flexible membrane wings using a viscous Navier-Stokes equations based fluid model. The flow was assumed to be laminar and incompressible and the results were in general agreement with certain limiting cases. However, the assumption of flow laminarity limited the scope for meaningful quantitative comparison to existing experimental data.

In reality, flows past real size kites are highly turbulent and CFD simulations need to take into consideration the effects of turbulence on the mean flow. The most accurate approach is to perform a Direct Numerical Simulation (DNS), where the Navier-Stokes equations are solved directly, fully resolving all relevant length and time scales. That condition requires both mesh and time step to be sufficiently small to capture the smallest turbulent flow scales as defined by Kolmogorov [40]. Coudou [41] performed a DNS of unsteady 3D flow over a LEI kite using Fluidity solver. The simulations were performed at Reynolds numbers of 1000 and 5000 and results indicated a strong interaction between vortices shed at the leading edge and the canopy, which is also expected to occur at higher Reynolds numbers. DNS is currently restricted to low Reynolds numbers, since its computational cost is proportional to Re^3 [42]. One of the largest simulations performed recently at $\mathrm{Re} = 125000$ [43], ran for about two weeks on the second largest supercomputer in the world that consists of 786 thousand cores [44]. As such it is clear that due to current hardware limitations, DNS is not a feasible method for engineering applications of high Reynolds number flows.

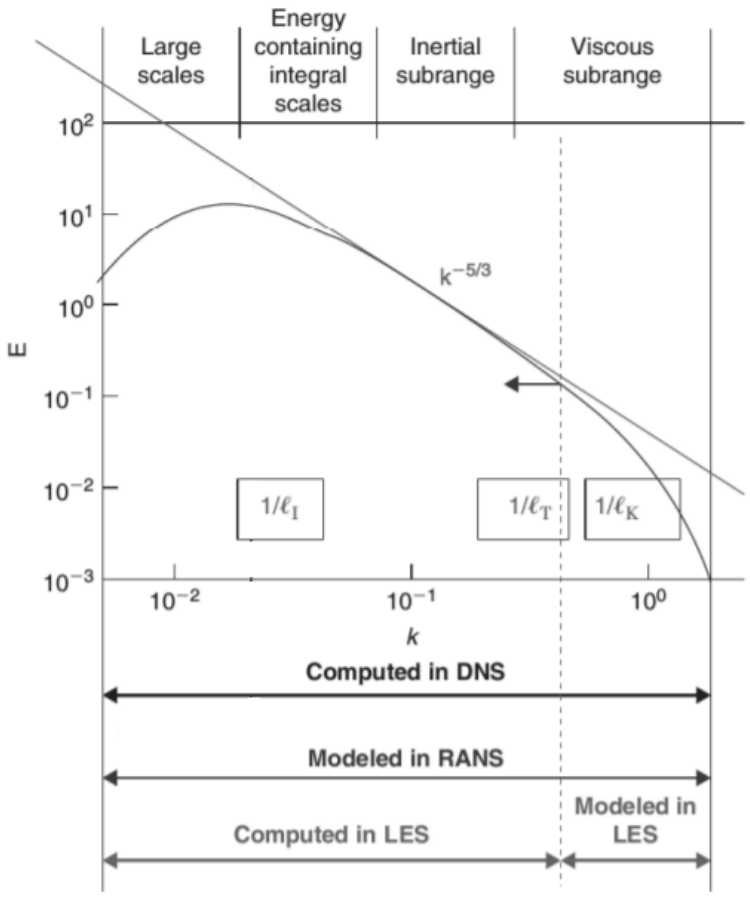

Figure 2.11: Differences between RANS, LES and DNS (reproduced and modified from [41]).

Another method to solve turbulent flows is called the Large Eddy Simulation (LES), which fully resolves the largest turbulent scales of the flow directly and models all the smaller scales. Due to LES still considerable computational power requirements, the most com-

mon CFD methodology for engineering applications is to use RANS equations, which use time-averaged (mean) quantities. RANS ignores the turbulent fluctuations and models the whole turbulence spectrum (see Figure 2.11). The flow past kite wings can often be assumed to be incompressible, due to low Mach number, and steady-state. RANS equations for steady-state incompressible flow represent conservation of mass and momentum:

$$\frac{\partial \overline{u}_i}{\partial x_i} = 0, \tag{2.2}$$

$$\overline{u}_j \frac{\partial \overline{u}_i}{\partial x_j} = -\frac{1}{\rho}\frac{\partial \overline{p}}{\partial x_i} + \nu \frac{\partial^2 \overline{u}_i}{\partial x_j^2} - \frac{\partial \overline{u_i' u_j'}}{\partial x_j}, \tag{2.3}$$

where $\overline{u}_i$ and $\overline{p}$ are the mean velocity and pressure, while $\overline{u_i' u_j'}$ is the Reynolds stress tensor. Reynolds stress tensor represents the effect of turbulent fluctuations and has to be modelled using a RANS turbulent model.

A popular turbulence model is the $k-\epsilon$ model [45], in which the local turbulent viscosity is calculated by means of two additional transport equations for turbulent kinetic energy and the energy dissipation rate. It performs best in free shear layers with relatively small pressure gradients [46] and has been used for analysis of flexible membranes and kite systems in the past. Kheiri et al [47] applied modified actuator disc theory to a crosswind kite power system and compared power production results with an Unsteady Reynolds-Averaged Navier-Stokes (URANS) simulation that used the $k-\epsilon$ turbulence model. The study assumed fully turbulent attached flow in all cases and modelled the kite surfaces as straight rigid wings. When applied to separated flows, $k-\epsilon$ model fails to accurately predict lift and drag coefficients, even if the prediction is better than when using potential flow methods [48].

An alternative to $k-\epsilon$ turbulence model is Wilcox's $k-\omega$ model [49], which performs better with flows experiencing adverse pressure gradients. Menter proposed the $k-\omega$ Shear-Stress Transport (SST) model in 1992 [50], that utilizes strength of both models. $k-\omega$ SST uses the $k-\omega$ model within the inner 50% of the boundary layer and then gradually changes to the $k-\epsilon$ model towards the boundary layer edge. Menter's model has been often used for kite and sail aerodynamics over the past years as it is proven to be good for adverse pressure gradients and airfoil flows in general [51]. Smith and Shyy performed an analysis of viscous turbulent flow over 2D flexible membranes using both $k-\epsilon$ [52] and $k-\omega$ SST [53] turbulence models. It was found that the $k-\epsilon$ model struggled to correctly predict leading edge separation over an inclined thin flat plate (see Figure 2.12) and that $k-\omega$ SST model is more suitable for investigating single-surface membrane wing aerodynamics. Viola et al [54] validated 3D RANS $k-\omega$ SST results against wind tunnel pressure measurements on yacht sails. Very good agreement found between the results allowed to interpret the modelled flow field with high confidence. Menter's $k-\omega$ SST has been applied to both 2D

aeroelastic applications [55] and detailed 3D kite aerodynamic analyses [56][57]. Deaves [4] analysed 3D aerodynamics of a Kitepower LEI V2 kite using RANS coupled with a $k-\omega$ SST turbulence model. The study focused on 3D viscous phenomena, such as flow separation, and their effect on lift and drag of the kite. Those results can be used as a reference for the results obtained in this thesis, since the geometry and flow conditions in both cases are similar. Qualitative comparison can be made regarding regions of flow separation on pressure and suction sides of the kite, while computed values of lift and drag coefficient can be compared quantitatively.

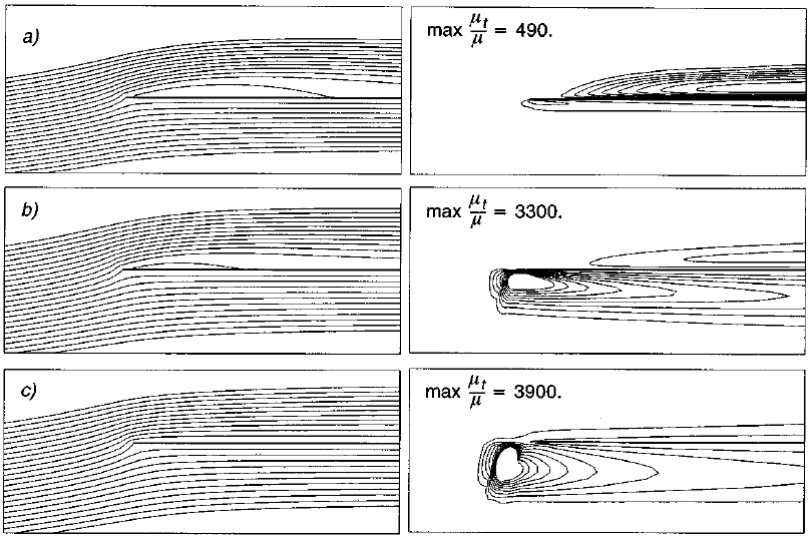

Figure 2.12: Comparison of streamfunction and eddy viscosity contours around a thin flat plate at 3 degrees angle of attack, Re = 1.3×10^6, using $k-\omega$ SST, BSL $k-\omega$ and standard $k-\epsilon$ turbulence models (top to bottom), as obtained by Smith and Shyy [53].

As mentioned at the beginning of the Section 2.2, boundary layer transition may have a significant effect on aerodynamics of a LEI kite, however this phenomenon has not really been studied in detail. Common turbulence models like $k-\omega$ SST assume that the boundary layer is always turbulent, as they cannot model the transition from laminar to turbulent separately. Only recently generic transition models that can be easily applied to a RANS simulation on an arbitrary mesh, such as $\gamma - \widetilde{\mathrm{Re}}_{\theta t}$ [58], have been developed and published. Folkersma et al [5] investigated boundary layer transition of a LEI kite airfoil using $k-\omega$ SST turbulence model with a $\gamma - \widetilde{\mathrm{Re}}_{\theta t}$ transition model and the results were in agreement with low Reynolds number ($Re = 10^5$) experiment over all angles of attack considered (see Figure 2.13). The results obtained from simulations with the transition model were closer to the experimental values than ones obtained without the transition model. As such, the results obtained for the LEI kite airfoil by Folkersma et al can be used in this thesis for the purpose of validation of the solver setup. Another application of $k-\omega$ SST turbulence model with $\gamma - \widetilde{\mathrm{Re}}_{\theta t}$ transition model is the study by Gaunaa et al [36], which used a 3D RANS simulation to validate a new potential flow method using vortex elements. Overview of selected RANS simulations of flexible membranes and kite systems

is presented in Table 2.1.

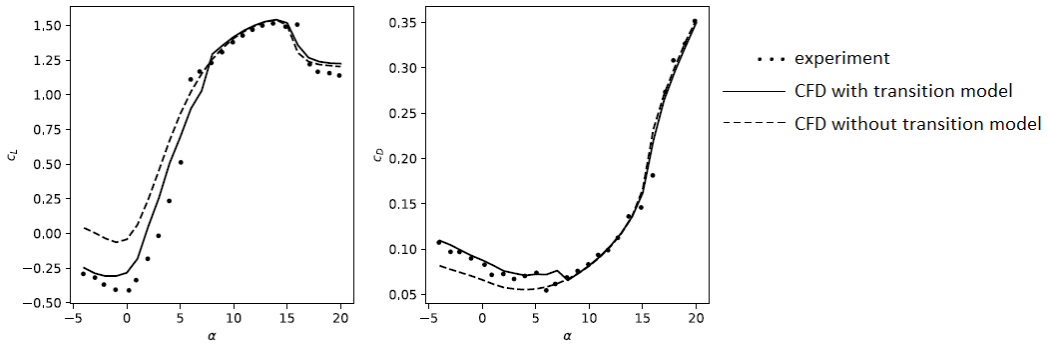

Figure 2.13: Lift and drag characteristics of a sailwing airfoil at low Reynolds number, as obtained by Folkersma et al [5].

2.2.4 Experimental studies

Due to numerous limitations and shortcomings of computational methods, some of the researchers turned towards experimental methods to try to characterize kite aerodynamic performance. Babinsky [60] performed a wind tunnel study on ram air wings to investigate the effects of various aerodynamic devices on lift-to-drag ratio. De Wachter [56] studied the 3D shape of a ram air kite in a wind tunnel using methods of photogrammetry and laser scanning. The determined shape was then analysed using a 3D RANS simulation with a $k-\omega$ SST turbulence model with $\gamma - \widetilde{\mathrm{Re}}_{\theta t}$ transition model in Ansys FLUENT software.

In general, wind tunnel experiments of larger devices are very challenging because scaling down a large inflatable membrane structure requires scaled deformations, which is very complex and not feasible to do properly. As such, experimental studies focused on kite aerodynamics moved towards field tests and in-situ aerodynamic characterisation of real-size kites in flight. In 2010 a test rig for kite performance measurement has been developed, where a kite was tethered to a moving vehicle [61]. It allowed to measure static flight performance and dynamic flight history through measurements of the tether force and kite position angles. Similarly, Hummel et al [62] developed a towing test setup (see Figure 2.14) that achieved good repeatability of measurements gathered for different membrane wings. Python [63] used the same towing test bench for evaluating the aerodynamic performance of three different kites to improve the original methodology proposed by Hummel et al. The main problem of this testing method however is the physical limit of the traction force, measurement uncertainty due wind variations and inability to measure lift-to-drag ratio for dynamic manoeuvres [64].

In order to rectify these problems, Oehler et al [6] proposed an innovative method for experimental characterisation of flexible kite aerodynamics. It consists of in-situ measurements of relative flow past a kite using on-board measurement setup, with kite performing

Table 2.1: Overview of selected RANS simulations of flexible membranes and kite systems.

reference	geometry	2D/3D	steady /unsteady	solver	turbulence model	transition model	mesh type
Folkersma et al (2018) [5]	LEI kite	2D	steady	openFOAM simpleFOAM	$k-\omega$ SST	$\gamma - \tilde{Re}_\theta$	structured O-mesh
Steiner (2018) [55]	LEI kite	2D	unsteady	openFOAM preCICE	$k-\omega$ SST	-	structured O-mesh
Deaves (2015) [4]	LEI kite	3D	steady	openFOAM simpleFOAM	$k-\omega$ SST	-	hybrid mesh
Sachdeva (2017) [57]	LEI kite	3D	steady	openFOAM simpleFOAM	$k-\omega$ SST	-	unstructured mesh
Coudou (2017) [41]	LEI kite	3D	unsteady	Fluidity	DNS	-	unstructured mesh
Gaunaa et al (2018) [36]	arbitrary kite	3D	steady	Ellipsys3D	$k-\omega$ SST	$\gamma - \tilde{Re}_\theta$	structured O-mesh
Maneia et al (2013) [59]	curved kite wing	3D	steady	STAR-CCM+	Spalart-Allmaras	-	unstructured mesh
Smith and Shyy (1995) [52]	flexible membrane wing	2D	steady	-	$k-\epsilon$	-	structured H-mesh
Smith and Shyy (1996) [53]	flexible membrane wing	2D	steady	-	$k-\omega$ SST	-	structured H-mesh
Kheiri et al (2018) [47]	rigid wing	3D	unsteady	Ansys FLUENT	$k-\epsilon$	-	hybrid mesh
Collie et al (2009) [48]	yacht sail	3D	steady	Ansys FLUENT	$k-\epsilon$	-	hybrid mesh
Viola et al (2013) [54]	yacht sail	3D	steady	Ansys FLUENT	$k-\omega$ SST	-	structured H-mesh

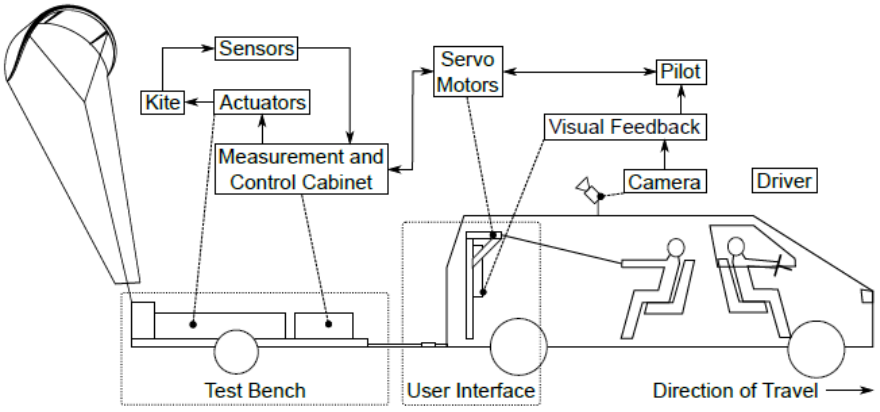

Figure 2.14: Towing test setup developed by Hummel et al [62].

routine flight manoeuvres. The setup allows to measure apparent wind velocity, angle of attack, lift-to-drag ratio and lift coefficient for any kite manoeuvre during regular operation. The results obtained for Kitepower LEI V3 kite showed reasonable agreement with currently established coefficients used in various simulations (see Figure 2.15). As such, these results will be used as experimental reference in this thesis. Detailed measurements of aerodynamic coefficients at various flight manoeuvres the kite performed will allow for quantitative comparison to numerical results. A similar measurement setup has been also used by Oehler et al [64] and van Reijen [65] to investigate turning manoeuvres and corresponding kite deformations, turn rates and aerodynamic efficiency. Aerodynamic coefficients obtained by van Reijen agree with those found by Python [63] on the towing test bench.

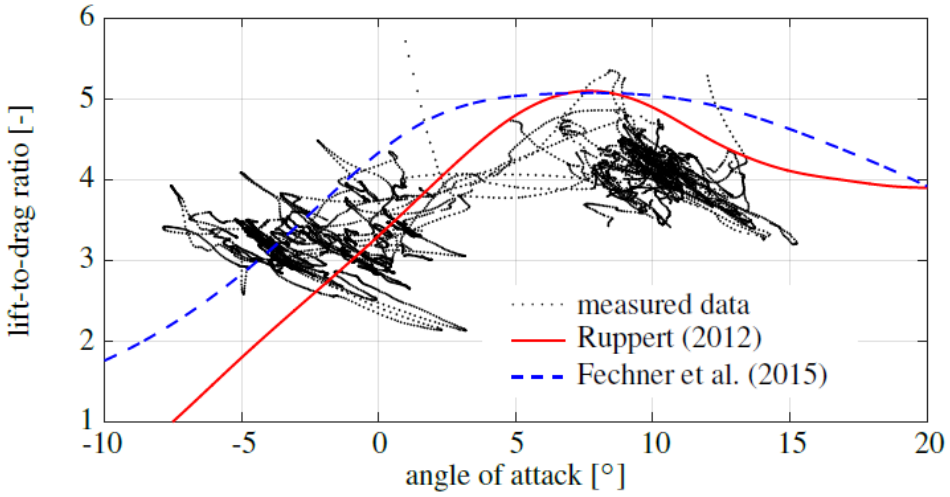

Figure 2.15: Comparison of lift-to-drag ratio measured by Oehler et al [6] with Ruppert [13] and Fechner et al [22] models.

Table 2.2: Overview of selected experimental studies of flexible membranes and kite systems.

reference	geometry	test type	measured parameters
Viola et al (2013) [54]	yacht sail	wind tunnel	pressure coefficient
Babinsky (1999) [60]	ram air wing	wind tunnel	lift and drag coefficients
de Wachter (2008) [56]	ram air wing	wind tunnel	lift and drag coefficients
Dadd et al (2010) [61]	ram air wing	towing setup	lift coefficient lift-to-drag ratio
Hummel et al (2019) [62]	various	towing setup	lift coefficient lift-to-drag ratio
Python (2017) [63]	LEI kite	towing setup	lift coefficient lift-to-drag ratio
Ruppert (2012) [13]	LEI kite	crosswind	relative wind speed angle of attack
Oehler et al (2018) [6]	LEI kite	crosswind	relative wind speed angle of attack lift coefficient lift-to-drag ratio

2.2.5 Challenges of viscous 3D aerodynamic modelling of flexible membranes

As mentioned in the beginning of Section 2.2, a LEI kite airfoil is a complex aerodynamic problem due to the flow topology that naturally features multiple flow separation zones. Depending on the Reynolds number, the flow separation can happen from laminar or turbulent boundary layer, which may greatly affect aerodynamic performance of the airfoil. The Reynolds numbers and angles of attack vary periodically because of the crosswind energy generation principles, and varying loads lead to substantial structural deformation. Extending the problem to 3D introduces additional flow effects, such as wingtip vortices, cross flow and other three-dimensional flow features caused by low aspect ratio and high anhedral angle of the kite [66].

Based on the review of literature given in the previous sections, it can be concluded that the significance of flow separation rules out the application of potential flow methods or other inviscid solvers for the purpose of a detailed three dimensional analysis of LEI kite aerodynamics. A 3D RANS solver is much better suited for such an analysis. The kite shape is going to be fixed during meshing, as setting up a coupled Fluid-Structure Interaction (FSI) simulation using 3D RANS and a structural solver is very challenging and computationally expensive. Recent FSI studies on kite aeroelastics focused on 2D analyses [55] or 3D analyses with a simplified aerodynamic model [17] [19]. In order to isolate variables,

the geometry considered is going to be rigid and represent the kite shape in high power setting, during traction phase. The reason for this is that during traction phase with high aerodynamic loads the kite's shape does not vary much, as high aerodynamic loading stiffens the structure and enlarges the projected area.

Recent study of LEI kite and sailwing airfoils performed by Folkersma et al [5] showed the importance of modelling transition for aerodynamic analysis of LEI kite airfoils at Reynolds numbers lower than 2×10^7. Boundary layer transition is a process of a laminar flow becoming turbulent. It is a complex phenomena that involves different modes. The primary modes of transition are:

- Natural transition, when two-dimensional Tollmien-Slichting instability waves start appearing in the boundary layer, followed by development of three-dimensional instability. Eventually turbulent spots grow from the fluctuations until the whole boundary layer becomes turbulent [67]. This process can be accelerated by disturbances in the free-stream or by surface waviness. This mode usually occurs on smooth surfaces.
- Bypass transition, when a large external perturbation (such as freestream disturbance or rough surface of the body) triggers a transition. Very common transition mode in applications with very high free-stream turbulence level such as turbomachinery flow [68].
- Separation-induced transition (also called separated flow transition), when a laminar boundary layer subjected to a large adverse pressure gradient separates and transition develops within the formed shear layer. The turbulent flow may reattach forming a laminar-separation / turbulent-reattachment bubble on the surface [69]. The laminar separation bubble has been studied in detail by Malkiel and Mayle [70].

Additionally, Mayle [69] distinguishes wake-induced transition, common in turbomachinery flows where the wakes of upstream blade rows heavily disrupt the laminar boundary layer on surfaces downstream. It is not clear whether this mode of transition is caused by high turbulence in the wake or the interaction of the freestream momentum deficit with the boundary layer, hence why it is considered different to bypass transition mode [71]. Additionally, a reverse transition may occur, from turbulent to laminar flow, if the flow is subjected to very strong acceleration [69].

Common RANS turbulence models cannot accurately predict the transition from laminar to turbulent flow. Their transport equations do not resolve instantenous flow field and as such, lack the information about the disturbances required to predict the transition. However, at lower Reynolds numbers, up to 2×10^7 [5], transition may have significant effects on aerodynamic characteristics of LEI kite airfoil (see Figure 2.16) and needs to be

modelled. The simulations of the flow past the LEI V3 kite in this thesis will be performed for a range of Reynolds numbers that goes below 2×10^7, which is the main motivation behind the use of the $\gamma - \widetilde{\mathrm{Re}}_{\theta t}$ transition model. Such a range of Reynolds numbers will allow to capture various flow conditions over the kite.

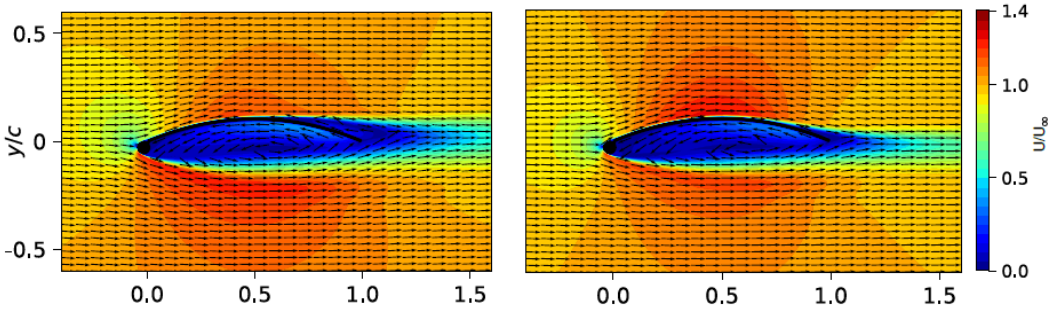

Figure 2.16: Flow field over a sailwing airfoil at zero angle of attack, Re = 10^5, with (left) and without (right) transition modelling, as obtained by [5].

2.3 Research objective

In this chapter various AWE concepts and methodologies for aerodynamic analysis of kites and flexible membranes used in the past have been reviewed. It can be concluded that 3D LEI kite aerodynamics is a complex problem with little literature and reference data available. Primary limitations of existing studies include two-dimensional flow representation, inaccurate flow separation prediction and lack of validation of numerical results against experimental data. The research objective of this thesis can therefore be stated as:

To expand on previously employed RANS methodologies by applying correlation based transition modelling to a 3D LEI kite geometry and comparing the results to existing numerical and experimental data. To analyse the flow field and corresponding 3D flow features around the kite at various Reynolds numbers and produce a set of reference data for LEI kite aerodynamics.

Based on this research goal, the following research question are formed and will be answered in the study:

1. *What is the benefit of employing a transition model to a $k-\omega$ SST turbulence model in the context of a 3D RANS simulation of LEI kite?*

   This question can be answered by performing a 3D RANS simulation with appropriate settings for the turbulence and transition models and comparing the results to the experimental and numerical data found in the literature. The primary references for numerical data include the work by Deaves [4] and Folkersma et al [5]. Results presented by Oehler and Schmel [6] will be used as a reference for experimental data.

The following sub-questions will assist with formulating the answer to the main question.

- To what extent is the prediction of the 3D flow effects and viscous phenomena improved when using a transition model, compared to $k-\omega$ SST model alone?
- How significant are the laminar phenomena at considered Reynolds numbers? At which Reynolds number can the flow field be approximated as fully turbulent?
- To what extent are the obtained results consistent with experimental and numerical data gathered in the past? Is the agreement improved compared to results obtained without transition modelling?

2. *What is the impact of 3D flow effects on the design of the LEI kite?*

   To answer this question, the results obtained in the project need to be compared to existing 2D numerical data obtained using a similar approach (Folkersma et al [5]). The following sub-questions will assist with formulating the answer to the main question.

   - What are the differences between flow patterns observed in 2D and 3D?
   - Are the flow patterns observed in 2D also present in 3D?
   - How are the aerodynamic parameters of the kite affected by extension of the 2D analysis to 3D?

3. *Is it possible to develop a reliable methodology for performing a 3D RANS simulation of LEI kite?*

   To answer this question, the methodology used to obtain the results needs to be investigated in the context of reliability of the results and model stability. The following sub-questions will assist with formulating the answer to the main question.

   - What meshing approach can lead to high quality of the resultant computational grid?
   - What boundary conditions should be used for the computational domain and how sensitive are the results to changes of those boundary conditions?
   - What are the prescribed and achievable convergence criteria and do they result in satisfactory accuracy?

Chapter 3

Numerical modelling

As discussed in the literature review Chapter 2, the choice of numerical modelling methodology is crucial to resolving desired flow features and obtaining reliable results for chosen geometry and flow conditions. This Chapter will first outline the underlying equations behind the simulations of incompressible fluid flow in Section 3.1. Schemes used to discretise the computational domain are treated in Section 3.2. Lastly, various ways of modelling the turbulence and transition are presented in Sections 3.3 and 3.4.

3.1 Governing equations

The flow field around a LEI kite can be assumed to be incompressible and of constant temperature, as typical flow velocities upstream and downstream of a kite are in the range of $15 - 30\ m/s$. This assumption makes incompressible Navier-Stokes equations, describing conservation of mass and momentum, suitable for analysis of LEI kite aerodynamics:

$$\frac{\partial \rho}{\partial t} + \frac{\partial \rho u_i}{\partial x_i} = 0, \tag{3.1}$$

$$\frac{\partial u_i}{\partial t} + u_j \frac{\partial u_i}{\partial x_j} = -\frac{1}{\rho}\frac{\partial p}{\partial x_i} + \nu \frac{\partial^2 u_i}{\partial x_j^2}. \tag{3.2}$$

These equations, written using Einstein summation convention, assume Eulerian description and Cartesian coordinate system. Here ρ represents fluid density, p stands for pressure and ν is the fluid kinematic viscosity. Under the assumption of steady-state solution, the temporal derivatives will further reduce to zero. The resultant set of equations however still

cannot be easily solved for turbulent flows and analytical solutions do not exist. As such, a typical approach to obtain a solution involves numerical procedures to solve the Navier-Stokes equations in a discretised domain – commonly referred to as Computational Fluid Dynamics.

3.2 Discretisation schemes

A very common discretisation method used in many engineering fields including fluid mechanics is the finite volume method. Its main advantage is the ease of application to numerical simulations for various types of conservation laws that are calculated for arbitrary geometries and meshes. When using the finite volume method, the domain of interest is discretised into a number of cells called control volumes. The flow field variables are set to constant within each of the volumes and fluxes of those variables between adjacent volumes (represented as surface integrals) are evaluated using the divergence theorem. This makes the method locally conservative, as the flux leaving a given volume is equal to the flux entering the neighbouring cell [72], which is another advantage for fluid mechanics applications.

With grid spacing tending to zero, the computational solution should approach the exact solution of the equations that are discretised. In case of simplified flow models, such as RANS, this means that past a certain grid refinement level, further refinement will not decrease the error. It is the consequence of original equations already averaging out the turbulence and resolving the mean flow only.

3.3 Turbulence modelling

Due to DNS and LES methods being too expensive for typical engineering applications, direct resolution of turbulent flow scales is not possible. As such, all turbulence and its effect on the mean flow need to be modelled. This can be achieved through Reynolds-averaged approaches, such as RANS, where all of the unsteadiness is averaged out. To derive RANS equations, Reynolds decomposition is used, that separates the time-averaged value of a variable and its fluctuation about that value:

$$u(x,t) = \overline{u}(x) + u'(x,t). \tag{3.3}$$

To derive RANS equations, Eq. (3.3) is substituted into the incompressible Navier-Stokes equations, Eq. (3.1) and Eq. (3.2), and subsequently time averaged, such that $\overline{\overline{u}}(x) =$

$\overline{u}(x); \overline{u'}(x,t) = 0$. The result is a system of equations that describes the mean flow field:

$$\frac{\partial \overline{u}_i}{\partial x_i} = 0, \tag{3.4}$$

$$\frac{\partial \overline{u}_i}{\partial t} + \overline{u}_j \frac{\partial \overline{u}_i}{\partial x_j} = -\frac{1}{\rho}\frac{\partial \overline{p}}{\partial x_i} + \nu \frac{\partial^2 \overline{u}_i}{\partial x_j \partial x_j} - \frac{\partial \overline{u'_i u'_j}}{\partial x_j}. \tag{3.5}$$

A new term arises, $\overline{u'_i u'_j}$, called theReynolds stress tensor that represents the averaged momentum transfer due to turbulent fluctuations. It is important to note that in this approach, any unsteadiness of the flow is averaged out and treated as turbulence [42]. The presence of Reynolds stress tensor means that the system is not closed and needs an introduction of a turbulence model – either through additional transport equations or further approximations to prescribe the Reynolds stress tensor, usually in terms of the mean flow quantities that can be computed. Turbulence closure through introduction of additional transport equations for the Reynolds stresses, known as Reynolds Stress Models, is not going to be further discussed in this text, as their computational cost is too high for the current research objective.

A common approach to model the Reynolds stresses is to draw an analogy from laminar flows, where transport of mass and momentum normal to the streamlines happens through viscosity [42]. Similarly, one can assume that the effect of turbulence can be seen as added viscosity that relates the Reynolds stress tensor and mean velocity gradients through:

$$\overline{u'_i u'_j} = \frac{2}{3} k \delta_{ij} - \nu_T \left(\frac{\partial \overline{u}_i}{\partial x_j} + \frac{\partial \overline{u}_j}{\partial x_i} \right), \tag{3.6}$$

where ν_T is the turbulent eddy viscosity. This relation is commonly known as Boussinesq hypothesis. It provides closure to the RANS equations and does not change their form, which makes it very convenient. The last step is to determine the value of $\nu_T(x_i, t)$. ν_T is not a property of the fluid but of the flow field itself and is commonly defined as a product of some characteristic length $l_*(x_i, t)$ and characteristic velocity $u_*(x_i, t)$. Different turbulent models will specify and calculate those quantities in different ways.

Two main classes of eddy viscosity turbulence models can be distinguished – algebraic, one-equation and two-equation models. Algebraic models, often called zero-equation models, propose algebraic closure to the RANS equations, through assumptions of uniform turbulent viscosity across the flow (normal to the mean flow direction) or through mixing-length. The main drawback of algebraic models is their incompleteness, as often the characteristic length $l_*(x_i, t)$ and characteristic velocity $u_*(x_i, t)$, or either of the two, need to be explicitly specified and are by definition dependent on the flow geometry [73].

One-equation and two-equation models attempt to remove this incompleteness by introducing one or two transport equations to determine the value of eddy viscosity ν_T. The most popular one-equation model is the Spalart-Allmaras model which uses a single model transport equation to calculate the eddy viscosity directly. It is computationally simpler than two-equation models, however it faces similar problems as the $k-\epsilon$ model with separated flows where it significantly overpredicts shear stresses [74]. Two-equation models are based off the idea of turbulent-kinetic-energy models, where velocity scale u_*, used to calculate ν_T, can be based on the turbulent kinetic energy:

$$u_* = ck^{1/2}, \tag{3.7}$$

with c being a constant. k is calculated using one model transport equation. The turbulent viscosity is then defined as:

$$\nu_T = ck^{1/2}l_*. \tag{3.8}$$

To close the turbulence model, an additional transport equation needs to be introduced for a second variable that will allow to determine the value of l_*. There have been many models developed in the past few decades that chose various variables for that purpose, as the choice itself is not very significant [73]. In this work, three of the most commonly used turbulence models in analyses of flows around flexible membranes, namely $k-\epsilon$, $k-\omega$ and $k-\omega$ SST, are presented. Although not used in this thesis, the general specification of $k-\epsilon$ and $k-\omega$ turbulence models is provided for convenience, as $k-\omega$ SST directly relates to these two. Note that in the rest of this document, any velocity u_i or pressure p present in the equations is by default assumed to represent Reynolds averaged quantities unless explicitly stated otherwise.

3.3.1 $k-\epsilon$ turbulence model

The $k-\epsilon$ turbulence model has been developed by Jones and Launder in 1972 [45] and it introduces two transport equations – one for k, the turbulent kinetic energy, and one for ϵ, the dissipation rate of turbulent kinetic energy. For Standard $k-\epsilon$ model [75] the equations are given by:

$$\frac{\partial k}{\partial t} + \frac{\partial k u_j}{\partial x_j} = \tau_{ij}\frac{\partial u_i}{\partial x_j} - \epsilon + \frac{\partial}{\partial x_j}\left[\left(\nu + \frac{\nu_T}{\sigma_k}\right)\frac{\partial k}{\partial x_j}\right], \tag{3.9}$$

$$\frac{\partial \epsilon}{\partial t} + \frac{\partial \epsilon u_j}{\partial x_j} = C_{\epsilon 1}\frac{\epsilon}{k}\tau_{ij}\frac{\partial u_i}{\partial x_j} - C_{\epsilon 2}\frac{\epsilon^2}{k} + \frac{\partial}{\partial x_j}\left[\left(\nu + \frac{\nu_T}{\sigma_\epsilon}\right)\frac{\partial \epsilon}{\partial x_j}\right]. \tag{3.10}$$

The Reynolds stress tensor is then:

$$\tau_{ij} = 2\nu_T \left[S_{ij} - \frac{1}{3}\frac{\partial u_k}{\partial x_k}\delta_{ij} \right] - \frac{2}{3}k\delta_{ij}, \tag{3.11}$$

with the mean strain rate tensor:

$$S_{ij} = \frac{1}{2}\left[\frac{\partial u_i}{\partial x_j} + \frac{\partial u_j}{\partial x_i} \right]. \tag{3.12}$$

$C_{\epsilon 1} = 1.44$, $C_{\epsilon 2} = 1.92$, $\sigma_k = 1.0$ and $\sigma_\epsilon = 1.3$ are model constants.

Knowing both k and ϵ, the characteristic length scale can be determined from as $L \sim k^{3/2}/\epsilon$, thus providing model closure. The eddy viscosity can then be calculated as:

$$\nu_T = C_\mu \frac{k^2}{\epsilon}, \tag{3.13}$$

where $C_\mu = 0.09$ is a model constant.

3.3.2 $k - \omega$ turbulence model

The $k - \omega$ turbulence model was formulated by Wilcox in 1988 [49] as an attempt to develop a model that performs well with boundary layers in adverse pressure gradients, thus overcoming the main shortcoming of the $k - \epsilon$ model. It introduces a transport equation for k, the turbulent kinetic energy, and for ω, the specific turbulent dissipation rate, or turbulence frequency:

$$\frac{\partial k}{\partial t} + \frac{\partial k u_j}{\partial x_j} = \tau_{ij}\frac{\partial u_i}{\partial x_j} - \beta^* \omega k + \frac{\partial}{\partial x_j}\left[\left(\nu + \sigma^* \nu_T\right) \frac{\partial k}{\partial x_j} \right], \tag{3.14}$$

$$\frac{\partial \omega}{\partial t} + \frac{\partial \omega u_j}{\partial x_j} = \frac{\gamma \omega}{k}\tau_{ij}\frac{\partial u_i}{\partial x_j} - \beta \omega^2 + \frac{\partial}{\partial x_j}\left[\left(\nu + \sigma \nu_T\right) \frac{\partial \omega}{\partial x_j} \right], \tag{3.15}$$

where:

$$\nu_T = \gamma^* \frac{k}{\omega}. \tag{3.16}$$

Model constants were originally determined as:

$$\beta = \frac{3}{40}; \beta^* = 0.09; \gamma = \frac{5}{9}; \gamma^* = 1; \sigma = 0.5; \sigma^* = 0.5. \tag{3.17}$$

3.3.3 $k-\omega$ SST turbulence model

Menter's idea behind $k-\omega$ SST turbulence model [50] is to combine $k-\epsilon$ and $k-\omega$ models using a blending function F_1 to utilize the advantages of both models. Near walls F_1 approaches unity and $k-\omega$ is used. Further from the surface F_1 reaches 0 and the model switches to $k-\epsilon$. Such formulation allows for accurate separation prediction and solid near-wall performance. OpenFOAM v1812 uses the 2003 model variant [76]. The transport equations for the turbulent kinetic energy and specific dissipation rate for that model are given by:

$$\frac{\partial k}{\partial t} + \frac{\partial k u_j}{\partial x_j} = \widetilde{P}_k - \beta^* k\omega + \frac{\partial}{\partial x_j}\left[\left(\nu + \sigma_k \nu_t\right)\frac{\partial k}{\partial x_j}\right], \tag{3.18}$$

$$\frac{\partial \omega}{\partial t} + \frac{\partial \omega u_j}{\partial x_j} = \gamma \frac{\widetilde{P}_k}{\nu_t} - \beta\omega^2 + \frac{\partial}{\partial x_j}\left[\left(\nu + \sigma_\omega \nu_t\right)\frac{\omega}{x_j}\right] + 2\left(1 - F_1\right)\sigma_{\omega 2}\frac{1}{\omega}\frac{\partial k}{\partial x_j}\frac{\partial \omega}{\partial x_j}. \tag{3.19}$$

The blending function F_1 is defined as:

$$F_1 = \tanh\left\{\left\{\min\left[\max\left(\frac{\sqrt{k}}{\beta^*\omega y}, \frac{500v}{y^2\omega}\right)^4 \cdot \frac{4\rho\sigma_{\omega 2}k}{CD_{k\omega}y^2}\right]\right\}^4\right\}, \tag{3.20}$$

where:

$$CD_{kw} = \max\left(2\rho\sigma_{\omega 2}\frac{1}{\omega}\frac{\partial k}{\partial x_i}\frac{\partial \omega}{\partial x_i}, 10^{-10}\right), \tag{3.21}$$

and y being the distance to the nearest wall. $\widetilde{P}_k$ is the production limiter term that prevents build up of eddy viscosity in the stagnation regions:

$$\widetilde{P}_k = \min\left(P_k, 10\beta^* k\omega\right), \tag{3.22}$$

where:

$$P_k = \nu_t \frac{\partial u_i}{\partial x_j}\left(\frac{\partial u_i}{\partial x_j} + \frac{\partial u_j}{\partial x_i}\right). \tag{3.23}$$

The turbulent eddy viscosity is then defined as:

$$\nu_t = \frac{a_1 k}{\max(a_1\omega, SF_2)}, \tag{3.24}$$

where $a_1 = 0.31$, S is the absolute value of the strain rate tensor and F_2 is a second blending function:

$$F_2 = \tanh\left[\left[\max\left(\frac{2\sqrt{k}}{\beta^*\omega y}, \frac{500\nu}{y^2\omega}\right)\right]^2\right]. \tag{3.25}$$

All model constants are interpolated between $k-\epsilon$ and $k-\omega$ models using the formula:

$$\alpha = \alpha_1 F + \alpha_2(1-F), \tag{3.26}$$

where α_1 and α_2 are the following:

$\beta_1 = 0.075, \beta_2 = 0.0828,$
$\gamma_1 = 5/9, \gamma_2 = 0.44,$
$\sigma_{k1} = 0.85, \sigma_{\omega 1} = 0.5,$
$\sigma_{k2} = 1, \sigma_{\omega 2} = 0.856.$

The final model constant is given by $\beta^* = 0.09$.

3.4 Transition modelling

Folkersma et al [5] showed the significance of transition modelling in aerodynamic simulations of LEI kite airfoils at Reynolds numbers lower than 2×10^7. At low Reynolds numbers, the flow exhibits laminar separation on the suction and pressure sides of the airfoil, as well as laminar separation bubble for $Re < 5 \times 10^6$, that regular turbulence models cannot capture.

Modelling transition within the RANS framework has always been somewhat problematic, as the information about flow disturbances, that typically cause laminar to turbulent flow transition, is lost during the averaging procedure. Transition itself is a very complex phenomenon that occurs through different mechanisms, as outlined in Section 2.2.5. The physics of transition are also not entirely understood and still actively researched, which is why not many phenomenological (physics based) models exist [77].

The most straightforward approach to transition prediction are DNS and LES simulations

[78], however these methods mostly lie outside of the scope of engineering applications due to their computational cost. An option is to apply unchanged eddy-viscosity turbulence models, such as the ones outlined in the previous sections, to transitional flows [79]. The accuracy of such simulations remains questionable, as further research showed that the ability of such models to predict transition seems to be a numerical artifact [80]. There exist several methods that address boundary layer transition prediction in CFD, but most of them suffer from either limited applicability or complex implementation. One can determine, for example experimentally, a transition location in the computational domain, and activate the turbulence model only downstream of that location. Such approach is limited to the particular geometry and Reynolds number. Over past few decades there have been efforts to formulate a more general approach for transition modelling in RANS simulations. Menter et al [81] formulated following requirements for a transition model compatible with existing CFD codes:

1. "Allow the calibrated prediction of the onset and the length of transition.
2. Allow the inclusion of the different transition mechanisms.
3. Be formulated locally (no search or line-integration operations).
4. Avoid multiple solutions (same solution for initially laminar or turbulent boundary layer).
5. Do not affect the underlying turbulence model in fully turbulent regimes.
6. Allow a robust integration with similar convergence as underlying turbulence model.
7. Be formulated independently of the coordinate system."

Until recently, hardly any transition model would fulfil all of those requirements. Widely used e^N method of van Ingen [82] and Smith and Gamberoni [83] provides very good prediction of transitional flows through linear stability theory. However it proved difficult to implement to existing CFD codes, as it requires coupling between the RANS solver, a high resolution boundary layer code and the e^N stability method [84], and such approach consists of many operations that are not local. Recent efforts focused on developing single-point transition models, meaning that they do not require any non local or integral operations. Such model formulation enables simple implementation to common CFD codes that are run on parallel cores or processors. An example of a phenomenological single-point transition model is a $k - k_L - \omega$ turbulence model developed by Walters and Cokljat [77]. It utilizes the idea that in the RANS equations, the Reynolds stress represents any unsteadiness or fluctuations of the flow, which means that transitional fluctuations can also be modelled through the Reynolds stress tensor. For steady laminar flow, the model prescribes very small values to the Reynolds stress. It introduces an additional transport equation for the laminar kinetic energy k_L to the Wilcox's $k - \omega$ model. k_L stands for the

energy of the fluctuations in the pre-transitional flow. The model provides good accuracy in transition prediction for various flows without any empirical correlations.

A good alternative to phenomenological transition models are correlation-based formulations that couple turbulence models with empirical transition correlations obtained from experimental databases covering a variety of geometries and flow conditions. The correlations are commonly based on the boundary layer momentum thickness and freestream conditions. It is important to note that these models do not attempt to model the physics of transition and rather rely on implementing empirical data effectively. The main strength of correlation-based models lies in the ease of calibration, as new experimental data can always be added to the existing correlations. They are also not limited to a single transition mechanism, as correlations can be provided for various types of transition. However, such approach typically requires non local information about boundary layer thickness and flow conditions in the freestream, and so do majority of existing correlation-based models such as one developed by Agu-Ghannam and Shaw [85] or Eulitz and Engel [86]. One of the first single-point (fully local) correlation-based formulations is Langtry and Menter's $\gamma - \widetilde{\mathrm{Re}}_{\theta t}$ model [58].

This transition model adds two transport equations to Menter's $k-\omega$ SST turbulence model – one for intermittency γ and one for local transition onset momentum thickness Reynolds number $\widetilde{\mathrm{Re}}_{\theta t}$. It can however also be implemented to other turbulence models, for example Spalart-Allmaras [87]. The model is able to take into account freestream conditions while maintaining fully local formulation thanks to the $\widetilde{\mathrm{Re}}_{\theta t}$ transport equation, where the freestream $\mathrm{Re}_{\theta t}$ is allowed to diffuse into the boundary layer through a diffusion term – effectively converting a global correlation to a local quantity.

The intermittency can be characterised as probability that a point in the flow field is located in the turbulent region. Intermittency can vary from 0, meaning the region is fully laminar, to 1, for fully turbulent regions. In this model, intermittency is used to trigger the transmission locally. It is done through modifying production and destruction terms in the transport equation for turbulent kinetic energy k in the original $k-\omega$ SST turbulence model:

$$\frac{\partial k}{\partial t} + \frac{\partial k u_j}{\partial x_j} = \widetilde{P}_k - \widetilde{D}_k + \frac{\partial}{\partial x_j}\left(\left(\nu + \sigma_k \nu_t\right) \frac{\partial k}{\partial x_j} \right), \tag{3.27}$$

where:

$$\widetilde{P}_k = \min\left(P_k, 10\beta^* k\omega\right) \gamma_{\mathrm{eff}}, \tag{3.28}$$

$$\widetilde{D}_k = \min\left(\max\left(\gamma_{\mathrm{eff}}, 0.1\right), 1.0\right) D_k. \tag{3.29}$$

The transport equation for intermittency is based on the wall distance and local flow field quantities:

$$\frac{\partial \gamma}{\partial t} + \frac{\partial \gamma u_j}{\partial x_j} = P_\gamma - D_\gamma + \frac{\partial}{\partial x_j}\left[\left(\nu + \frac{\nu_t}{\sigma_f}\right)\frac{\partial \gamma}{\partial x_j}\right]. \tag{3.30}$$

The production term is then defined as:

$$P_\gamma = F_{\text{length}}\, c_{a1} \rho S \left[\gamma F_{\text{onset}}\right]^{0.5} \left(1.0 - c_{e1}\gamma\right), \tag{3.31}$$

with:

$$F_{\text{onset}} = \max\left(F_{\text{onset2}} - F_{\text{onset3}}, 0\right), \tag{3.32}$$

$$F_{\text{onset1}} = \frac{\mathrm{Re}_\nu}{2.193\,\mathrm{Re}_{\theta c}}, \tag{3.33}$$

$$F_{\text{onset2}} = \min\left(\max\left(F_{\text{onset1}}, F_{\text{onset}}^4\right), 2.0\right), \tag{3.34}$$

$$F_{\text{onset3}} = \max\left(1 - \left(\frac{R_T}{2.5}\right)^3, 0\right), \tag{3.35}$$

$$\mathrm{Re}_\nu = \frac{y^2 S}{\nu}, \quad \mathrm{R}_T = \frac{\mathrm{k}}{\nu\omega}. \tag{3.36}$$

F_{onset} controls the transition onset and quickly grows from 0 to 1 when the boundary layer becomes turbulent, based on the ratio of vorticity Reynolds number Re_ν to the critical momentum thickness Reynolds number $\mathrm{Re}_{\theta c}$. This activates intermittency source term and leads to turbulence production. The F_{length} function controls transition length. Both $\mathrm{Re}_{\theta c}$ and F_{length} are empirical correlations related to local transition onset momentum thickness Reynolds number $\widetilde{\mathrm{Re}}_{\theta t}$.

The destruction term, or relaminarisation source, is defined as:

$$D_\gamma = c_{a2}\Omega\gamma F_{\text{turb}}\left(c_{e2}\gamma - 1\right), \tag{3.37}$$

where Ω represents the vorticity magnitude. F_{turb} is designed to disable intermittency destruction outside of the laminar boundary layer or in the viscous sublayer and is given by:

$$F_{\text{turb}} = e^{\left(-\frac{\mathrm{R}_T}{4}\right)^4}. \tag{3.38}$$

A second transport equation is formulated for local transition onset momentum thickness Reynolds number $\widetilde{\mathrm{Re}}_{\theta t}$:

$$\frac{\partial \widetilde{\mathrm{Re}}_{\theta t}}{\partial t} + \frac{\partial \widetilde{\mathrm{Re}}_{\theta t} u_j}{\partial x_j} = P_{\theta \mathrm{t}} + \frac{\partial}{\partial x_j}\left[\sigma_{\theta t}\left(\nu + \nu_t\right)\frac{\partial \widetilde{\mathrm{Re}}_{\theta t}}{\partial x_j}\right]. \tag{3.39}$$

In the freestream, the source term $P_{\theta t}$ forces $\widetilde{\mathrm{Re}}_{\theta t}$ to match the local $\mathrm{Re}_{\theta t}$ determined from the empirical correlations,

$$P_{\theta t} = \frac{c_{\theta t}}{t}\left(\mathrm{Re}_{\theta t} - \widetilde{\mathrm{Re}}_{\theta t}\right)\left(1.0 - F_{\theta t}\right), \tag{3.40}$$

where $t = \frac{500\nu}{U^2}$ is a time scale, while U represents the velocity magnitude.

$F_{\theta t}$ turns off the source term within the boundary layer, thus enabling diffusion of $\widetilde{\mathrm{Re}}_{\theta t}$ from the freestream into the boundary layer.

$$F_{\theta t} = \min\left(\max\left(F_{\text{wake}} \cdot e^{-\left(\frac{y}{\delta}\right)^4}, 1.0 - \left(\frac{\gamma - 1/c_{e2}}{1.0 - 1/c_{e2}}\right)^2\right), 1.0\right), \tag{3.41}$$

$$F_{\text{wake}} = e^{-\left(\frac{\mathrm{Re}\,\omega}{10^5}\right)^2}, \tag{3.42}$$

$$\mathrm{Re}_\omega = \frac{\omega y^2}{\nu}, \tag{3.43}$$

$$\delta = \frac{375\Omega y \nu\, \widetilde{\mathrm{Re}}_{\theta t}}{U^2}. \tag{3.44}$$

F_{wake} function turns off $F_{\theta t}$ in the wake regions.

Model constants have been determined as:

$$c_{e1} = 1.0, \quad c_{a1} = 2.0, \quad c_{e2} = 50.0, \quad c_{a2} = 0.06, \quad \sigma_f = 1.0,$$

$$c_{\theta t} = 1.0, \quad \sigma_{\theta t} = 2.0.$$

Finally, the intermittency is modified to be able to exceed value of 1 during laminar boundary layer separation to improve the prediction of separation-induced transition:

$$\gamma_{\text{sep}} = \min\left(s_1 \max\left[0, \left(\frac{\mathrm{Re}_\nu}{3.235 Re_{\theta c}}\right) - 1\right] F_{\text{reattach}}, 2\right) F_{\theta t}, \tag{3.45}$$

$$\gamma_{\text{eff}} = \max\left(\gamma, \gamma_{\text{sep}}\right), \tag{3.46}$$

where $F_{\text{reattach}} = e^{-\left(\frac{R_T}{20}\right)^4}$ and $s_1 = 2.0$.

The transition model also redefines the F_1 blending function of the original $k-\omega$ SST turbulence model to prevent switching to $k-\epsilon$ within a laminar boundary layer:

$$F_1 = \max\left(F_1, F_3\right), \quad F_3 = e^{-\left(\frac{R_y}{120}\right)^8}, \quad R_y = \frac{y\sqrt{k}}{\nu}. \tag{3.47}$$

The boundary conditions for γ are unity at the inlet and zero normal flux at walls. For $\widetilde{\mathrm{R}}\mathrm{e}_{\theta t}$ it is zero flux at walls, while for the inlet it is calculated using the empirical correlations. The model requires y^+ of approximately 1 for the first cell in the computational grid to ensure proper transitional boundary layer capture, and boundary layer cell growth rate of 1.1 to 1.15.

The model has been extensively validated against various aerodynamic and turbomachinery flows, both in 2D and 3D, by Langtry [71] using CFX-5 solver. The model has been calibrated primarily using flat plate test cases. The 2D aeronautical validation cases included Aerospatiale A airfoil, GE wind turbine airfoil, McDonnell Douglas 30P-30N 3-element flap configuration and the drag crisis of a cylinder. The 3D test cases included transonic DLR F-5 wing with shock induced laminar separation and full helicopter body with wake-induced transition on the tail wing. It was shown that the model can account for natural transition, bypass transition, wake-induced transition and separation-induced transition, without affecting solver's convergence detrimentally. For 2D airfoils the accuracy of the model was shown to be comparable to the e^N method. The main drawback of the transition model is lack of correlations for cross flow instability. The formulation is also not Galilean invariant, however that only poses an issue when the domain consists of multiple moving walls [81].

Sørensen [88] implemented the model in an in-house incompressible Navier-Stokes solver EllipSys3D and validated it for various aeronautical 2D and 3D test cases. Additionally, Folkersma et al [5] validated the $\gamma - \widetilde{\mathrm{R}}\mathrm{e}_{\theta t}$ transition model against experimental data for a sailwing airfoil and subsequently generated results for a LEI kite airfoil using OpenFOAM. The resuts demonstrated the capability of the model to capture laminar separation bubble and laminar to turbulent flow transition that follows. Ability of the model to correctly predict the drag crisis of a cylinder should be a big benefit for flow prediction around LEI kites due to their circular leading edge.

Chapter 4

Meshing and simulation setup

Before actual results are generated, it is necessary to verify the mesh convergence and simulation settings. Firstly, the mesh generation process and associated mesh quality metrics are explained in Sections 4.1 and 4.2. The simulation settings used are outlined in Section 4.3. Mesh sensitivity study results, regarding the influence of mesh resolution, boundary layer cells growth ratio and boundary conditions on the results are presented in Section 4.4.

4.1 Mesh generation approach

Generation of high quality volume mesh for the LEI V3A kite posed a major challenge in this work, due to the geometrical complexity of the kite that involves a large anhedral angle, inflated leading edge and chordwise struts (see Figure 4.1). The wing geometry has been imported from Surfplan to Rhinoceros – a commercial Computer Aided Design (CAD) modelling software based on Non-Uniform Rational Basis Spline (NURBS) mathematical model – to generate a simplified CAD geometry suitable for meshing. Computational meshes have been generated using the commercial software to Pointwise.

4.1.1 CAD modelling

Rhinoceros was chosen for CAD model preparation, due to the flexibility it offers in terms of curve and surface manipulation. The goal of the modelling was to generate a smooth, watertight model that can be easily imported to Pointwise. Watertight means that each edge has exactly two neighbouring surfaces, or that each surface is connected to each other without any empty space in between.

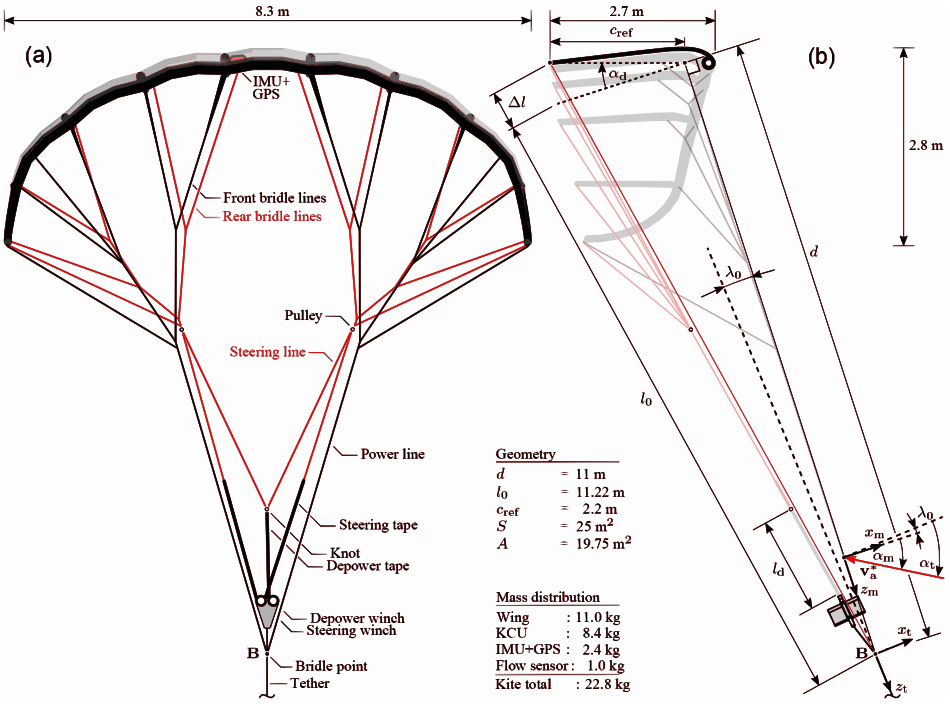

Figure 4.1: Geometry of the LEI V3A kite.

The original geometry, as presented on Figure 4.1, has been exported from Surfplan, a kite design software, in a format readable by Rhinoceros, such as Drawing eXchange Format. From then on, multiple simplifications and enhancements have been made, notably:

- Removal of bridle system and chordwise struts.
- Conversion of all edges defining the geometry to splines.
- Specification of finite thickness of the canopy.
- Definition of rounded trailing edge that connects the upper and lower surfaces of the canopy.
- Filling in behind the LE tube.
- Recreation of kite tips.

A few reasons stand behind these simplifications. The geometry exported from Surfplan was defined using polylines of very small resolution and had to be converted to splines to make the model smooth and more detailed. Bridle system has been removed because the analysis is limited to kite aerodynamics only – no fluid-structure interaction is considered and the geometry is assumed to be rigid. Chordwise struts have been removed to greatly simplify the meshing process. The impact of this change on the flow solution and resultant aerodynamic forces is uncertain, since struts certainly limit the cross flow across the geometry. The study of the effect of struts on the present results is left as future work. The

canopy was given a small thickness with a rounded trailing edge because of the requirements of meshing software. Slight filling behind the LE has been added to improve mesh quality in that region, with assumed small impact on the flow solution, as determined by Deaves [4]. The filling originates from the LE tube at about 60° angle and connects to the lower surface of the canopy at about 25% of the chord length. A comparison between original and filled in profile can be seen on Figure 4.5. Tips of the kite have been recreated to ensure watertight model, while remaining as close as possible to the original geometry. The resultant CAD model is shown in Figs. 4.2-4.4. The procedure followed to generate the surfaces can be found in Appendix A.

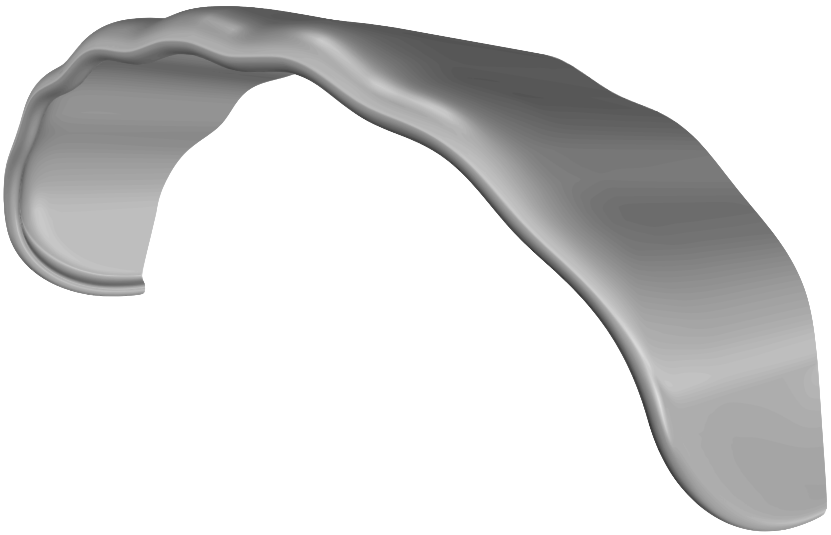

Figure 4.2: LEI V3A CAD model perspective view.

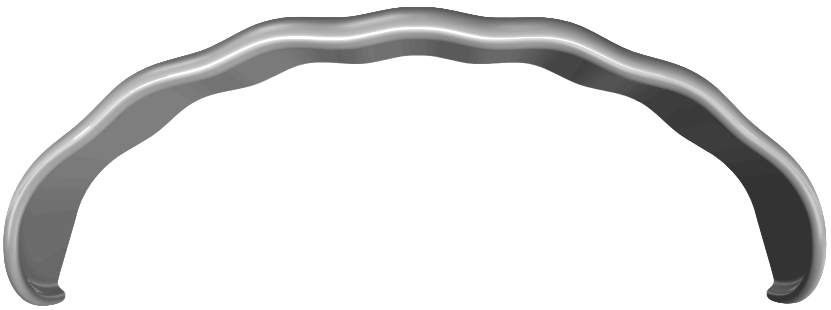

Figure 4.3: LEI V3A CAD model front view.

4.1.2 Mesh generation

Mesh generation for 3D LEI kite has proven quite a challenge in the past, as their bowed shape and LE-canopy connection makes fully structured mesh generation impractical. Unstructured mesh is an option, however the number of elements required would rapidly increase to unworkable levels, given y^+ and mesh quality requirements for Reynolds numbers of a few millions and above. Generally hybrid structured and unstructured meshing

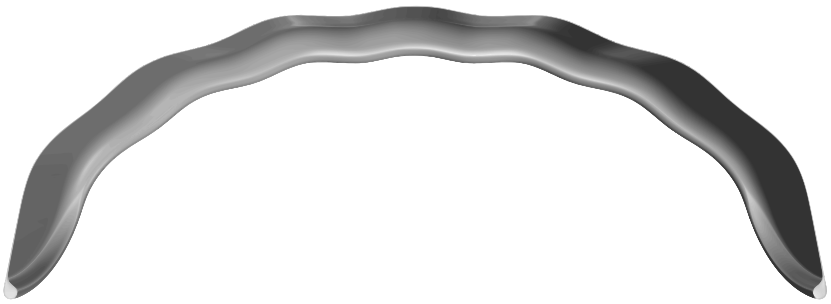

Figure 4.4: LEI V3A CAD model rear view.

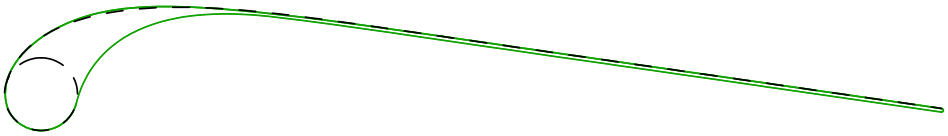

Figure 4.5: Original (dashed line) and filled in (solid line) profile at the kite symmetry plane.

approach has been adopted for 3D kites [56], however it can result in large regions of very low quality, severely non-orthogonal cells [4]. As such, one of the objectives for this work was set to generate a high quality mesh using a method that can be reliably reproduced on other similar shapes.

For that purpose, Pointwise grid generation software has been chosen. It offers automated unstructured mesh generation algorithm called T-Rex [89], which stands for anisotropic tetrahedral extrusion. It allows for extrusion of high quality, high aspect ratio tetrahedra layers, that can be later combined into hexahedra, prisms and pyramids. This allows to create hybrid mesh that behaves and looks like structured mesh in the boundary layer and near-wall region, thanks to being hexahedra-dominant and flow-aligned. It then transitions into the farfield tetrahedra-dominant region through use of prism and pyramid layers. The extrusion can initiate off structured, unstructured or hybrid surface grid. The algorithm is automated and Pointwise provides a few variables that can be used to control refinement level and quality of the resultant mesh, such as growth ratio of the hexahedral layers, maximum included angle or skewness allowed in the domain. Anisotropic cell extrusion generally stops once they reach isotropy, however the stopping condition is allowed to vary locally depending on parameters such as local mesh quality or distance to other extrusion fronts. This feature makes T-Rex a very robust algorithm that offers a lot of control over the resultant mesh, while ensuring no invalid cells, such as those with negative volume, are created.The generated grid provides the benefits of structured grid in the boundary layer region, while retaining flexibility of unstructured meshing.

The procedure for volume mesh generation for the LEI V3A kite in Pointwise can be split into two main parts – surface mesh generation (consisting of one or more surface *domains*) and volume mesh generation (one or more *blocks*). First, the surface of the kite is meshed, thus forming the basis for extrusion to the volume grid. Because the kite is symmetrical

and the assumed flow solution is steady-state, only half of the geometry has been meshed. The assumed coordinate system has origin at the symmetry plane, at the LE. The grid generation process has been iterative, as various mesh topologies and extrusion settings were tested and assessed based on mesh quality, simulation results and convergence.

Eventually the following mesh topology has been chosen for the surface mesh of the kite:

- Fully structured 2D domains from the symmetry plane to the start of the tip.
- Hybrid structured and unstructured T-Rex generated 2D domains at the tip.

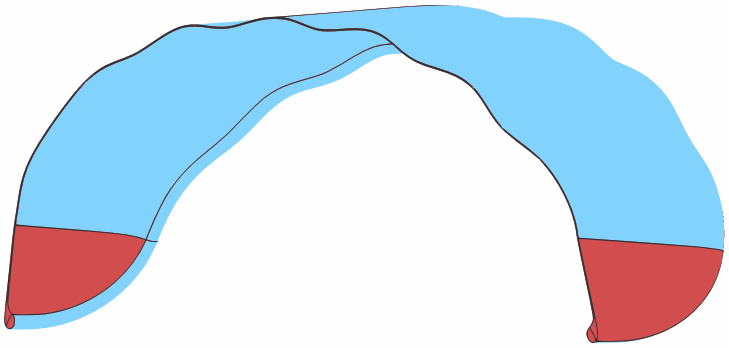

Figure 4.6: Structured (light blue) and unstructured (red) surface domains.

The idea is to use structured domains for any quasi-rectangular region and only utilize unstructured surface mesh for triangular areas, where structured grid would have low quality. The regions of structured and unstructured domains are shown on Figure 4.6. The structured domains from symmetry plane to the start of the tip are shown on Figure 4.7. Tip meshing is presented on Figure 4.8 – the red lines indicate edges from which T-Rex extrusion fronts advance. It creates anisotropic triangles with prescribed initial size and growth ratio such that it matches the adjacent structured domains and advances them until isotropy is achieved. Afterwards it combines as many elements as possible to quads. The blue edge, which also belongs to the adjacent structured domain, has element distribution set such that it matches the T-Rex mesh well. The tip mesh on the pressure side was created in the same way (Figure 4.9b). On the TE tip domains the T-Rex fronts advance from all the edges (Figure 4.9a).

Once the surface mesh has been completed, it can be extruded to form a volume mesh. That process is relatively straight forward. A half sphere, centred at mid-span LE point, of radius equal to 100 chord lengths, is created to define the computational domain boundaries. Next, T-Rex algorithm extrusion is set up to start from the kite surface domains with given first cell height and extrude at least 5 full anisotropic layers. This requirement was added because at the symmetry plane the algorithm would sometimes stop after just a few layers. What happens then is that subsequent layers of anisotropic tetrahedra are extruded with specified growth ratio, similarly to hyperbolic extrusion algorithm, until they

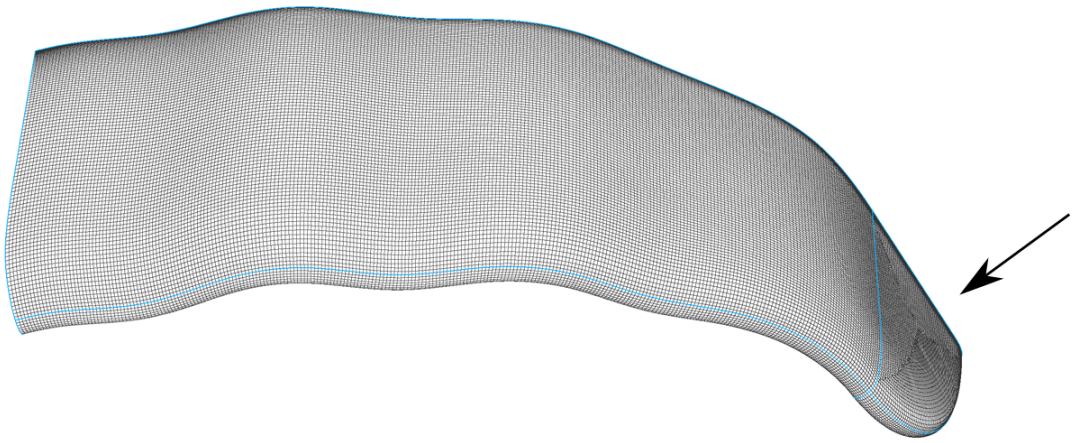

Figure 4.7: Structured surface domains.

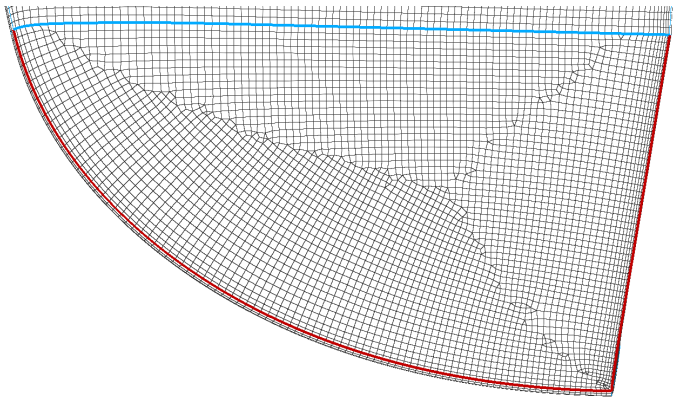

Figure 4.8: Unstructured surface domains on the tip.

reach isotropy or meet other stopping criteria, such as cell collision or failure of cell skew criteria. Once the anisotropic extrusion finishes, created elements are combined into hexahedra, prisms and pyramids. The remaining space in the domain is filled with isotropic tetrahedra that comply with any additional refinement criteria. The symmetry plane is set to *Match* boundary condition with *Push Attributes* setting turned on, so that cell distribution at that domain is automatically adjusted to cells created by the T-Rex algorithm.

Figure 4.10 presents resultant mesh topology around the kite over a chordwise cross-section near the symmetry plane. Violet elements represent hexahedra, red indicate prisms, pyramids are shown as yellow and tetrahedra are represented in light blue. Figure 4.11 shows the spanwise cross-section of the mesh. Mesh topology around the kite tip is shown on Figure 4.12. Overall, the extents of different types of elements across various cross sections are shown on Figure 4.13. Additional refinement in the vicinity of the kite can be seen on Figure 4.14. Next section will discuss various mesh quality metrics and extrusion parameters used to obtain this volume mesh.

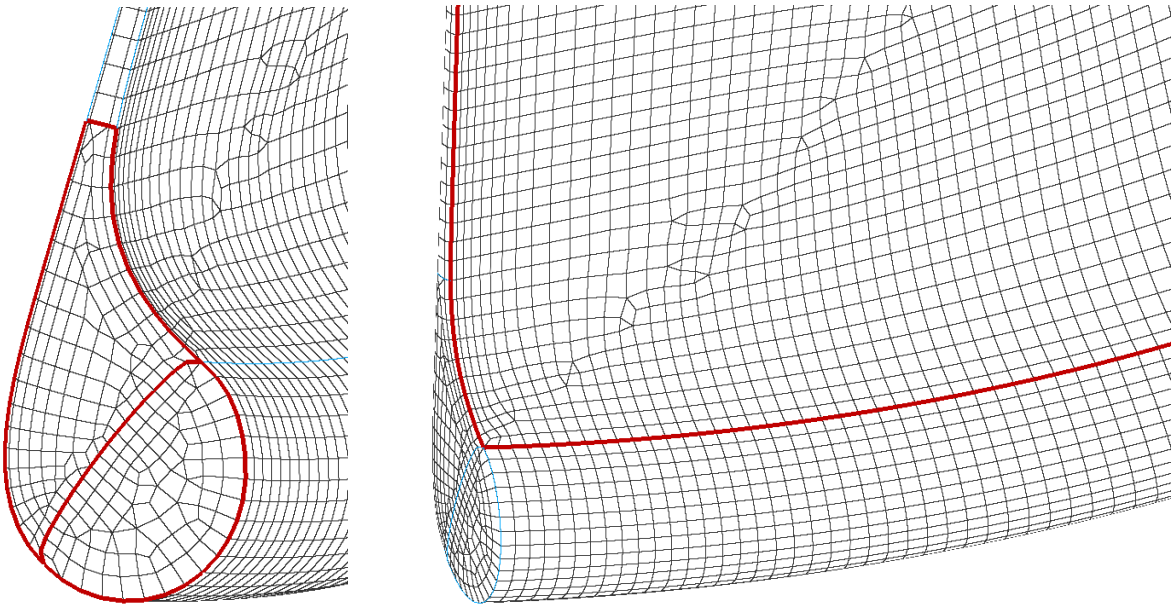

(a) Trailing edge tip mesh.

(b) Tip mesh on the pressure side.

Figure 4.9: Unstructured surface domains at the tip.

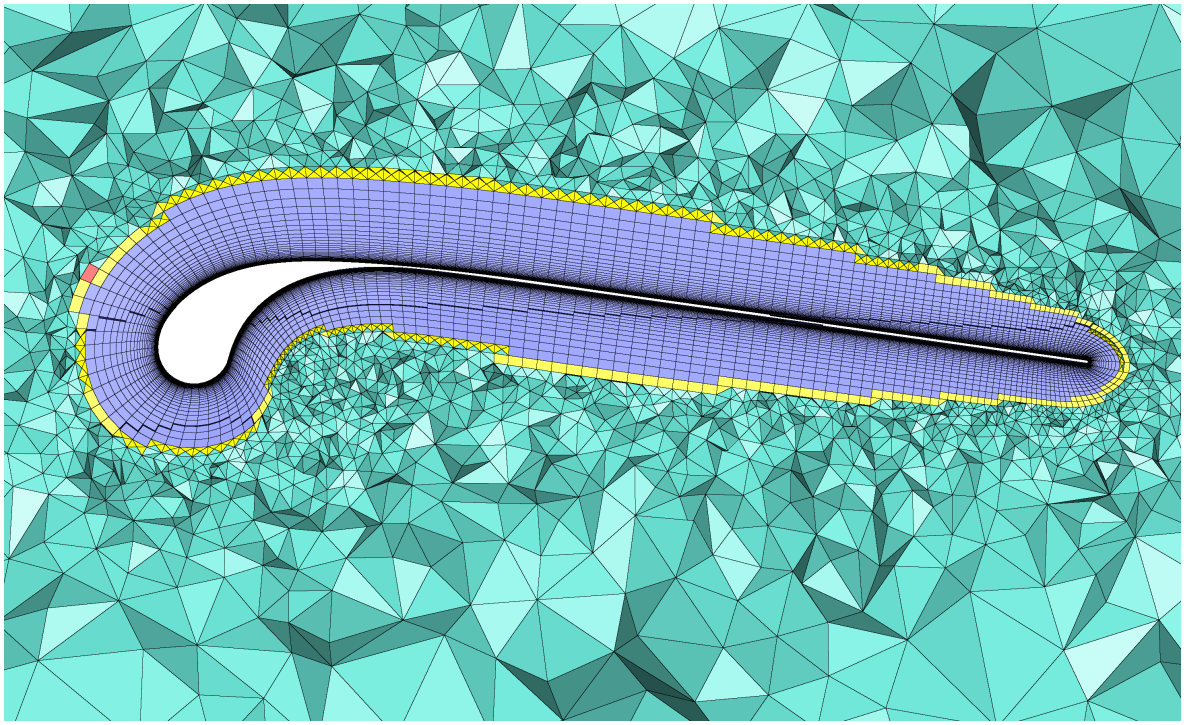

Figure 4.10: Mesh topology near the symmetry plane.

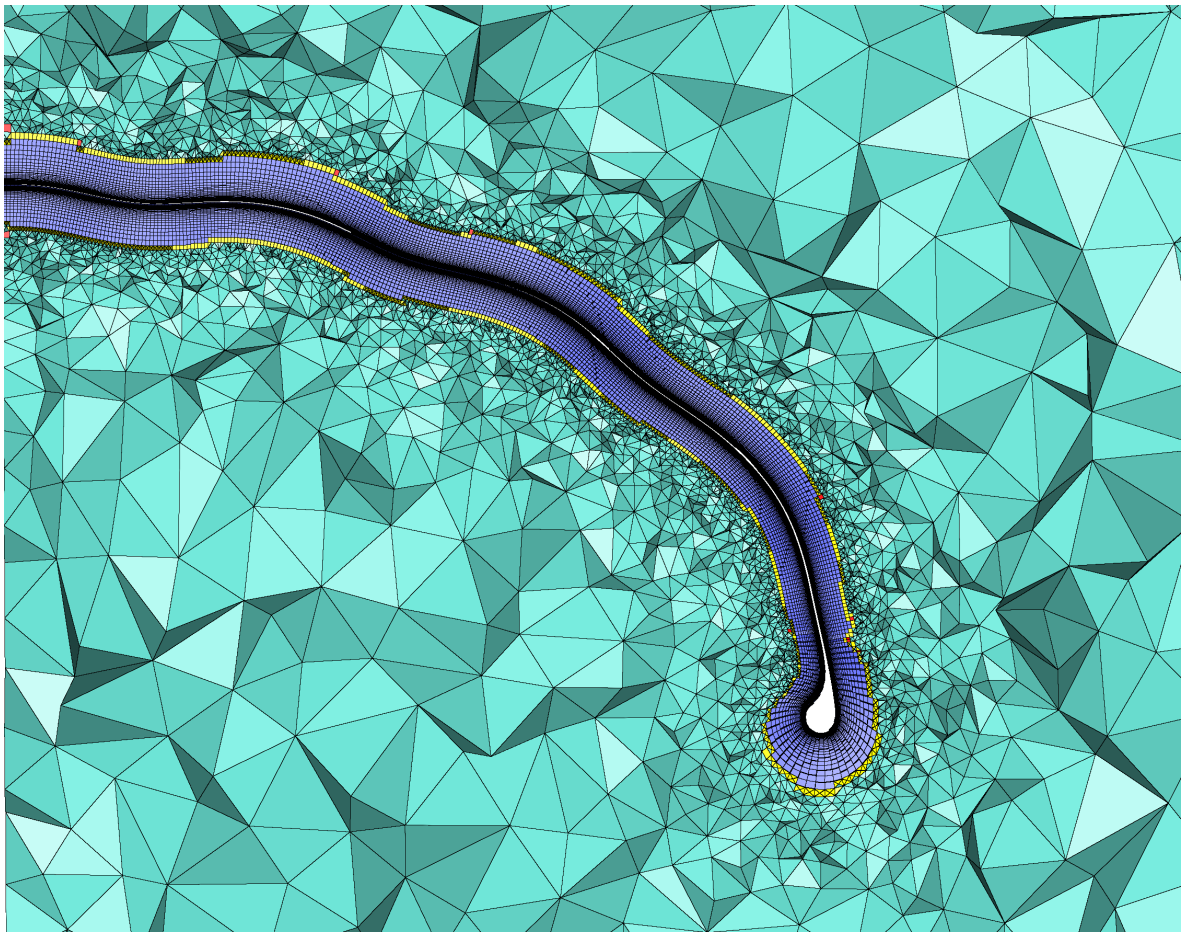

Figure 4.11: Mesh topology over the span of the kite.

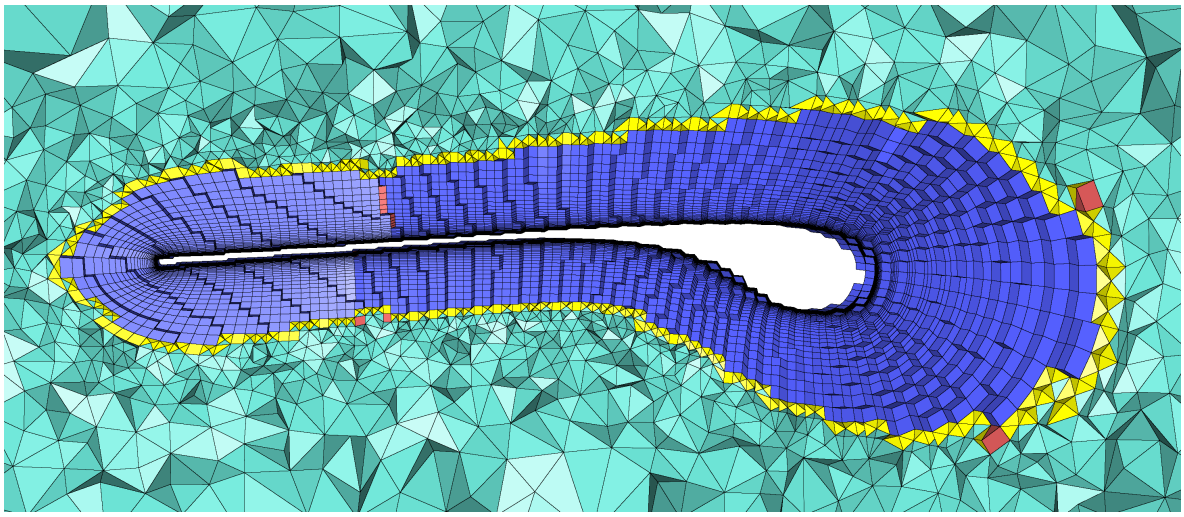

Figure 4.12: Mesh topology around the kite tip.

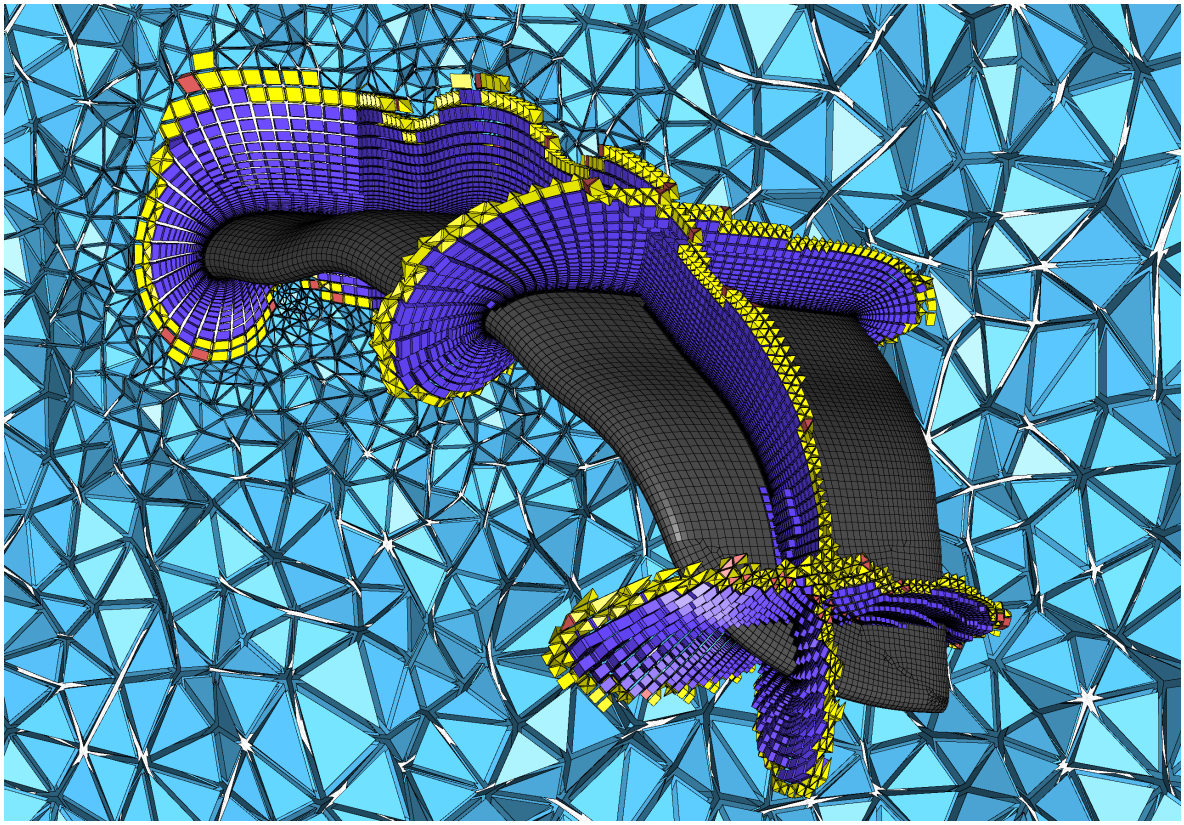

Figure 4.13: Extents of the hexahedra layers around the kite.

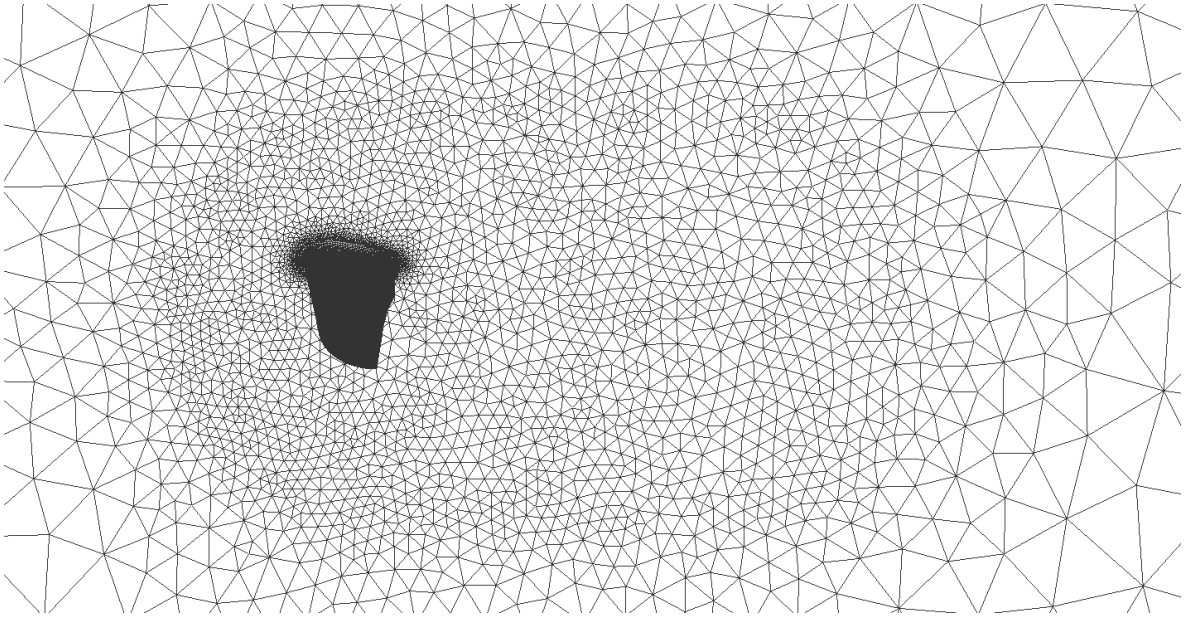

Figure 4.14: Mesh topology in the vicinity of the kite, symmetry plane.

4.2 Mesh quality

The main focus of the meshing process has been on ensuring high quality of grenerated the mesh, paying particular attention to:

- Low volume ratios of adjacent cells (< 10 for majority of the grid).
- Reasonable aspect ratios of the boundary layer cells (up to a few thousands for the first few layers).
- Minimized number of severely non-orthogonal cells ($> 70°$).
- Minimized cell skewness.

Volume ratio is defined as the maximum ratio of a given cell volume to any adjacent cell volumes. Large volume ratios can result in poor convergence and instability of the solution. Aspect ratio is computed as the ratio of the longest edge length to the shortest edge length of a cell. Cell non-orthogonality is an angle between the normal of a face shared by two adjacent cells and a line that connects those cells' centroids, averaged for all adjacent cells (see Figure 4.15, where β denotes the non-orthogonality angle). Non-orthogonality leads to solution instability and numerical errors due to OpenFOAM calculations of gradients at cell faces [90], mostly affecting diffusive terms in the N-S equations. Cell skewness, which can be defined in different ways (equiangle, equiarea, equivolume, centroid skewness, refer to [91]) can similarly introduce numerical errors and mostly affects calculations of convective derivatives [90].

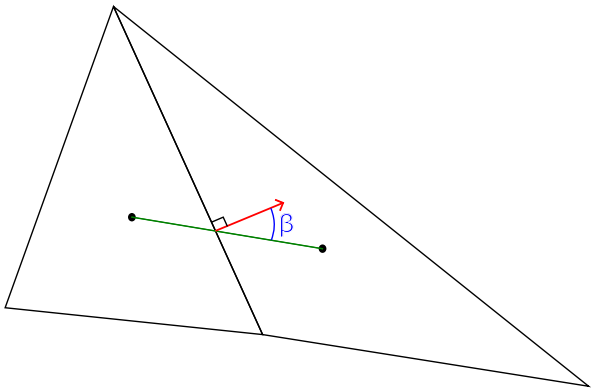

Figure 4.15: Cell non-orthogonality (β) definition.

In any type of 3D domain that is built around a complex shape, creation of several low quality cells is inevitable. As such, the goal is not to avoid any low quality cell, but to minimize their number and keep the overall mesh quality high. If possible, eliminating any degenerate cells (skewness > 0.99, non-orthogonality $> 89°$) is also desirable. Pointwise developers, as well as André Bakker from ANSYS [92], recommend to keep the maximum skewness below 0.8 for a good grid, however values up to 0.9 can be acceptable, provided

the solver can deal with such cells. OpenFOAM checkMesh utility gives warnings when non-orthogonality exceeds $70°$, but does not indicate a failed mesh check. Given $y^+ < 1$ requirement and considered Reynolds numbers of up to 15 million in this work, aspect ratio of the first cell extruded off the kite surface will be of several thousands. This is common practice in high Reynolds number aerodynamics simulations and OpenFOAM can handle high aspect ratio cells in the boundary layer well.

Surface extrusion algorithms used to create 3D blocks are very sensitive to surface mesh quality. For quad-dominant surface domains, Pointwise recommends to keep the maximum area ratio below 8-10 to guarantee smooth surface mesh and high quality volume mesh. The grids generated in this work have maximum area ratio between 5 and 6 for 3 to 4 elements in the whole domain, usually near the region of the tip trailing edge (Figure 4.9a). The aspect ratio of the surface mesh has to be kept below 5 in order to reduce the skewness of pyramids connecting anisotropic and isotropic cells near the trailing edge of the kite model.

Figure 4.16 shows the distribution of various quality metrics on an example kite volume mesh used in this thesis. The distributions look solid, as the vast majority of the cells have very high quality. This grid contains a total of 5.5 million cells, with about 4 million hexahedra in the near-wall region. There's only 5 cells that exceed centroid skewness of 0.8, which is a good result. Skewness equiangle is worse, as 64 cells exceed 0.8. However, maximum included angle metric, which is another measure of skewness that represents the maximum angle inside of the cell in degrees, shows that only 4 cells exceed 165°, which is acceptable for such grid. The mesh contains multiple non-orthogonal cells, which will be explained in more detail in Section 4.2.1. The only quality metric with sub-optimal results is equivolume skewness – there is over 100 cells that exceed 0.95. It is however a bit misleading, since this measure indicates how isotropic a cell is, whereas T-Rex intentionally creates anisotropic boundary layer cells. Because of this, it is more reasonable to use centroid skewness and included angle metrics to assess the quality of T-Rex extruded mesh instead. Majority of those high equivolume-skew cells are grouped behind the trailing edge near the symmetry plane, where hexahedral cells transition to tetrahedra.

4.2.1 Cell non-orthogonality

When extruding a volume mesh with really low first cell height (less than 10^{-5} of the chord length), it was found that multiple hexahedral cells at the kite surface were flagged as severely non-orthogonal by OpenFOAM, as seen on Figure 4.17. Even though it seems to be a rather unintended result, upon consultation with Pointwise it was determined that the extrusion is indeed behaving correctly. The non-orthogonality is related to very high aspect ratio of the boundary layer cells, which leads to high sensitivity of non-orthogonality calculations to potential shifts in cell centroids. The shift usually occurs because hexahedral cells deviate from perfect cuboids.

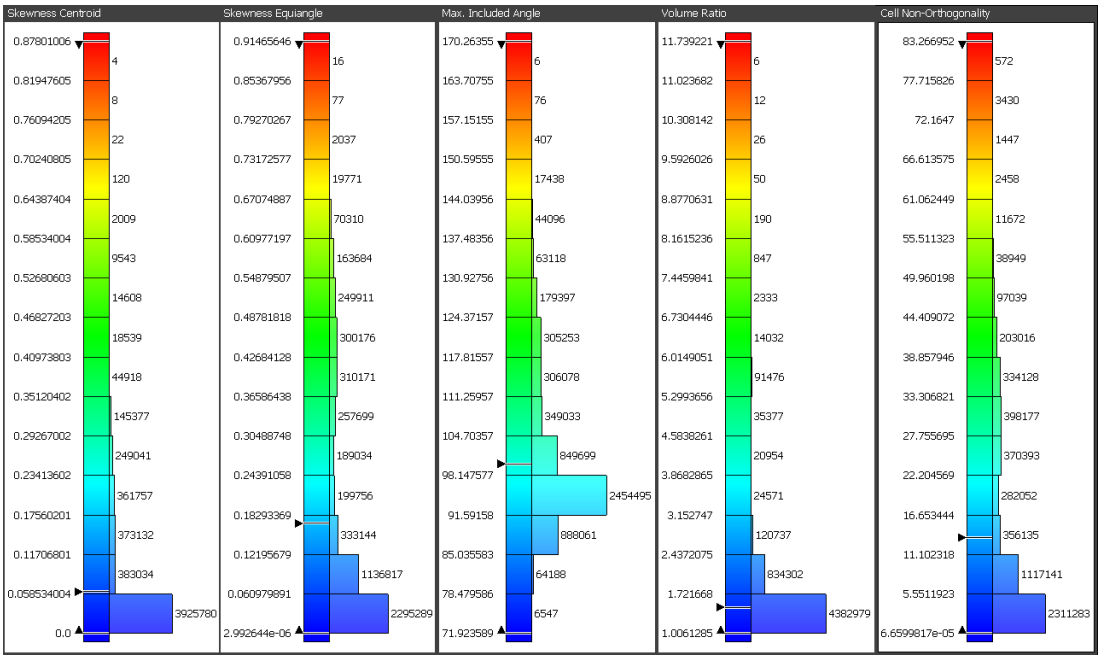

Figure 4.16: Mesh quality metrics for an example kite volume mesh

Since those cells could not be eliminated, their impact on the solution convergence and results was evaluated. Two almost identical volume meshes, one with first cell height (spacing) of 10^{-4} of the chord length ($y^+ < 1$) and one with first cell height of 2×10^{-6} of the chord length ($y+ << 1$) were tested for Reynolds number of 100,000. The former mesh had no severely non-orthogonal cells, while the latter had a few thousands at the surface. No solution instability was observed and solution convergence was unaffected. The resultant lift and drag coefficients of the kite differ by less than 1.0%. The skin friction coefficient over the kite surface in the region of laminar separation bubble seems more stable and physical for the mesh with non-orthogonal cells, presumably due to better boundary layer resolution. It also resembles kite airfoil results of Folkersma et al [5] better. The comparison can be seen on Figure 4.18. Based on this result, the effect of those non-orthogonal cells in the boundary layer is assumed to be negligible.

4.2.2 T-Rex extrusion parameters for maximised mesh quality

Over many volume mesh iterations, T-Rex extrusion parameters that lead to the best mesh quality for given kite grid topology were determined. It is important to note that stopping criteria and other parameters are essentially a trade off between creating more hexahedral cells and increased mesh quality. In an extreme case, one can create a fully unstructured, tetrahedra exclusive mesh with very high quality, but it does not imply good accuracy of the simulation results, and would result in a massive number of cells. Balancing cell count, mesh quality and the number of hexahedra was the main challenge during the mesh creation process.

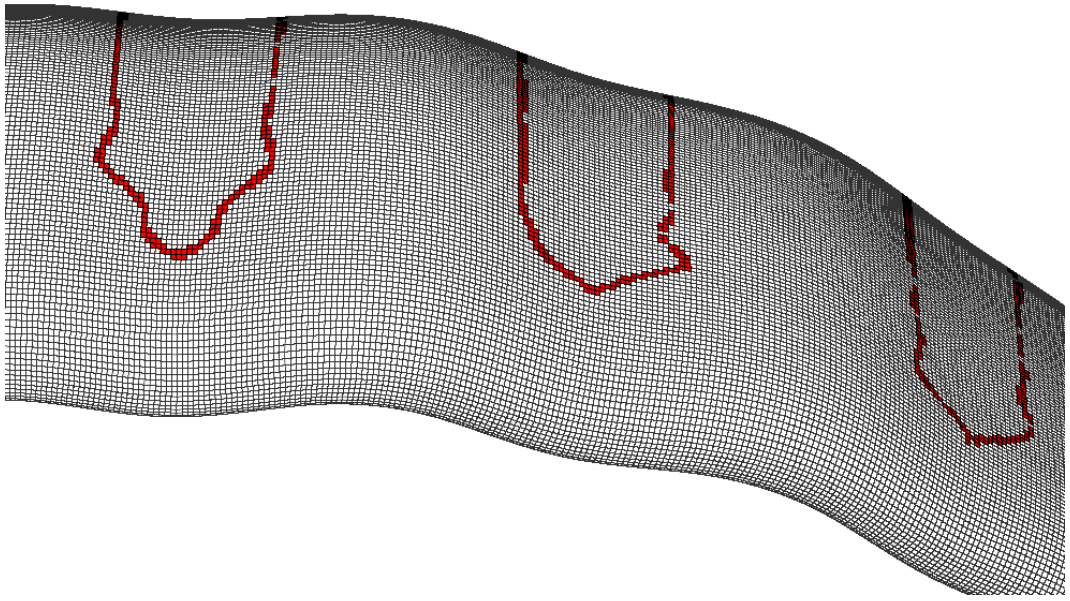

Figure 4.17: Severely non-orthogonal cells (red) at the kite surface.

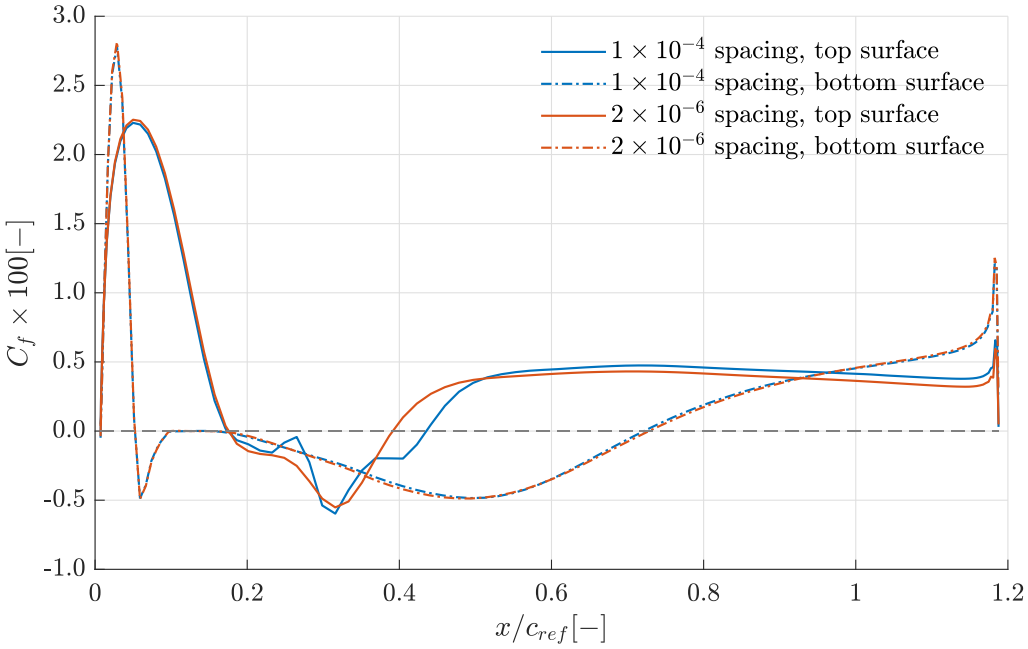

Figure 4.18: Skin friction coefficient over a kite chordwise cross section for various spacing of the first cell in the boundary layer.

T-Rex extrusion parameters are presented in Table 4.1. Growth rate of 1.15 resulted in smoothest hexahedra layers in the region behind the LE, while also complying with grid requirements for the $\gamma - \widetilde{\mathrm{Re}}_{\theta t}$ transition model as defined by Langtry [71]. Collision buffer controls how extrusion front behaves when it may collide with another portion of the front. Reducing the value from 2.0 to 0.8 prevented early stopping of the extrusion above the concave surfaces of the kite. Aniso-iso blend controls the transition from anisotropic to isotropic tetras, and vice versa. Values above 0 allow the front to keep advancing anisotropic cells after it already transitioned to isotropic tetras. This effectively increases the region of hexahedral cells, as can be seen on Figure 4.19. Isotropic height of 1.2 allows the algorithm to continue extruding anisotropic cells past the isotropic condition, up to 120% of isotropic height. Skew criteria have been set rather liberally, because they apply to the original extruded tetrahedra, before they are combined to hexahedra, prisms and pyramids. Due to very high aspect ratios of cells in the first few layers, the extruded tetrahedra have very high skewness. It is not a problem, as the skewness vanishes once these elements are combined to hexahedra. Equivolume and equiangle skewness criteria set below 1.0 would sometimes completely prevent the extrusion. Centroid skewness does not share this property, so the criterion was set to 0.8, as recommended by Pointwise.

Table 4.1: T-Rex extrusion parameters used for LEI V3A volume mesh.

Parameter	Value
Growth rate	1.15
Collision buffer	0.8
Aniso-iso blend	0.5
Isotropic height	1.2
Max. angle	165
Equivolume skewness	1.0
Equiangle skewness	1.0
Centroid skewness	0.8

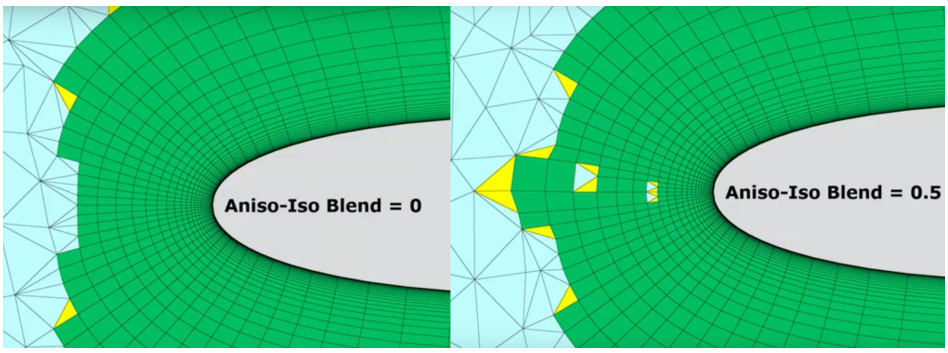

Figure 4.19: Aniso-iso blend effect (reproduced from [93]).

4.3 Simulation settings

The simulation setup used in this thesis has been adapted from Folkersma et al [5] OpenFOAM setup for the 2D airfoil. OpenFOAM is an open-source CFD toolbox written in C++ [94]. Version v1812 of the software is used in this work. The solution is obtained using an incompressible steady-state solver simpleFoam that uses the Semi-Implicit Method for Pressure Linked Equations (SIMPLE) algorithm developed by Patankar and Spalding [95].

The kite model has been scaled so that unit length represents $c_{ref} = 2.2\mathrm{m}$, as defined on Figure 4.1. As a result, the projected area of the half-kite is scaled to $A_{ref} = 2.0403m^2$. The projected area is used to normalise resultant lift and drag forces (Eqs. (4.1) and (4.2)) to stay consistent with force coefficient calculations from Oehler et al [6]. The coordinate system is defined as follows – the x-axis represents the chordwise direction, z-axis points in the spanwise direction and y-axis points upwards. Next three subsections will outline OpenFOAM case setup in more detail.

$$C_L = \frac{2L}{\rho U_\infty^2 A_{ref}}, \tag{4.1}$$

$$C_D = \frac{2D}{\rho U_\infty^2 A_{ref}}. \tag{4.2}$$

4.3.1 Boundary conditions

Due to the hemispherical computational domain, `inletOutlet` and `outletInlet` boundary conditions are set for the farfield domain. It is a mixed boundary condition that changes depending on whether the flow enters the domain or not. Uniform values are prescribed for the velocity and turbulence quantities of the inflow, with pressure gradient set to zero. For the outflow, pressure is set to zero, with zero gradients of velocity and turbulence quantities. No-slip boundary condition is applied at the kite surface. Symmetry plane has `symmetry` boundary condition imposed.

The magnitude of the inlet velocity is set to unity, with varying direction depending on the desired angle of attack. Since velocity, density and reference chord are all equal to one, the magnitude of the Reynolds number is fully controlled through the kinematic viscosity with $\mathrm{Re} = \frac{1}{\nu}$. Turbulence quantities at the inlet are calculated from prescribed turbulence intensity Tu, expressed in percentages, and the eddy viscosity ratio ν_T/ν:

$$k = \frac{3}{2}\left(U_{inlet}\frac{\mathrm{Tu}}{100}\right)^2, \tag{4.3}$$

and

$$\omega = \frac{k}{\nu} \cdot \frac{\nu}{\nu_t}. \tag{4.4}$$

The initial value for Tu was set to 2%, with eddy viscosity ratio equal to 10. Later, in Section 4.4, it will be shown that the choice of those boundary conditions does not influence the solution much.

The boundary conditions for γ are unity at the inlet and zero gradient at kite surface. For $\widetilde{\mathrm{Re}}_{\theta t}$ it is zero gradient at kite surface, while for the inlet it is calculated using the empirical correlations:

$$\widetilde{\mathrm{Re}}_{\theta t} = 1173.51 - 589.428\mathrm{Tu} + \frac{0.2196}{\mathrm{Tu}^2}, \text{ for } \mathrm{Tu} \leq 1.3, \tag{4.5}$$

$$\widetilde{\mathrm{Re}}_{\theta t} = 331.5(\mathrm{Tu} - 0.5658)^{-0.671}, \text{ for } \mathrm{Tu} > 1.3. \tag{4.6}$$

4.3.2 Solution control

Numerical schemes and equation solver settings outlined in Tables 4.2 and 4.3 provided swift convergence and stable solution for Reynolds numbers ranging from 1×10^5 and 15×10^6 and for angles of attack between -5° to 24°. `Corrected` schemes were used for surface normal gradient and Laplacian computations, because they provide an explicit non-orthogonal correction, necessary for meshes that contain cells not perfectly aligned with the Cartesian coordinate system. Non-orthogonal correctors specify the number of repeated solutions of the pressure equation, which is used to calculate that correction. Setting the number to one or higher can stabilize the solution computed over a mesh with non-orthogonal cells, at the cost of increased computation time. To ensure solution stability for the first few hundred iterations one non-orthogonal corrector was used for Reynolds numbers up to 3×10^6, two for Reynolds number 5×10^6 and three for Reynolds numbers above 10×10^6. Upwind schemes were used for divergence computations to improve solution stability.

Table 4.2: Numerical schemes used in the simulations.

Gradient	Gauss linear
Divergence (u)	bounded Gauss linearUpwind default
Divergence $(k, \omega, \gamma, \widetilde{\mathrm{Re}}_{\theta t})$	bounded Gauss upwind
Surface normal gradient	corrected
Laplacian	Gauss linear corrected

Table 4.3: Equation solvers and algorithms used in the simulations.

Solver (p)	GAMG; Gauss-Seidel smoother
Solver $(u, k, \omega, \gamma, \widetilde{\mathrm{Re}}_{\theta t})$	smoothSolver; symmetric Gauss-Seidel smoother
Relaxation factor (u)	0.9
Relaxation factor $(k, \omega, \gamma, \widetilde{\mathrm{Re}}_{\theta t})$	0.7
Non-orthogonal correctors	1 to 3

It was determined that solution residuals for various cases generally stabilise between 500 and 2000 iterations (Figure 4.20). As such, all simulations were run for 4000 iterations to make sure they converge. Few cases were run for up to 10000 iterations, however no significant differences in the results have been observed between solutions at 4000th and 10000th iteration. For the majority of the cases, the highest residuals settle between 10^{-6} and 10^{-5}. When transient flow behaviour is present in the simulation, for example when the kite is in stall conditions, the highest residuals generally remain between 10^{-5} and 10^{-4} and sometimes show rather large oscillations (Figure 4.21). However, even in those cases the force coefficients remain stable throughout the simulation time (Figure 4.22).

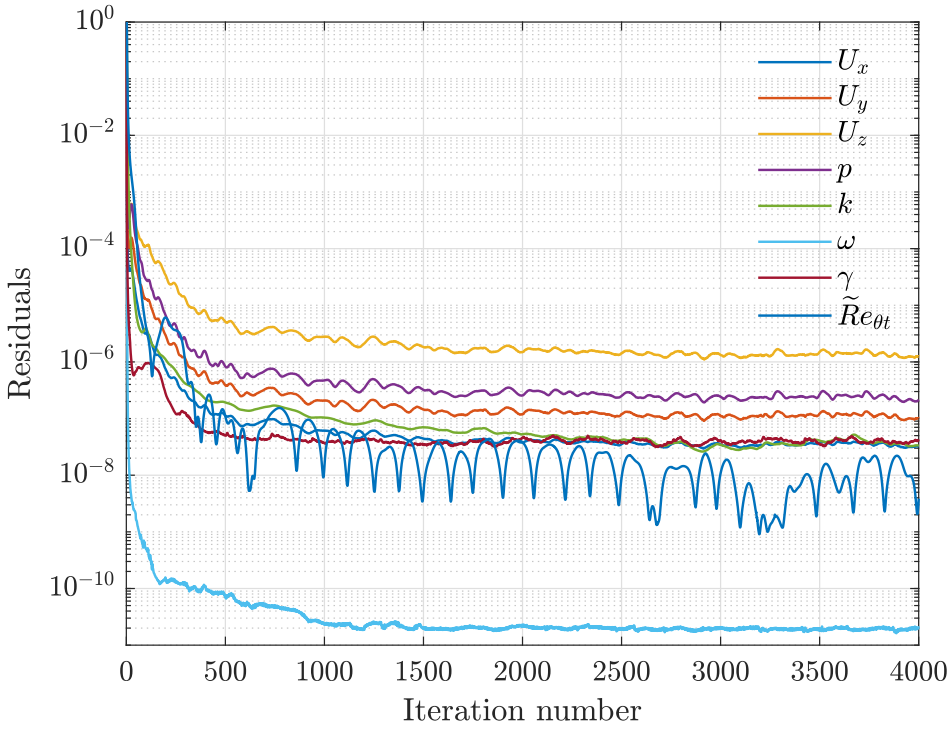

Figure 4.20: Residuals for case $\mathrm{Re} = 1 \times 10^6, \alpha = 6°$.

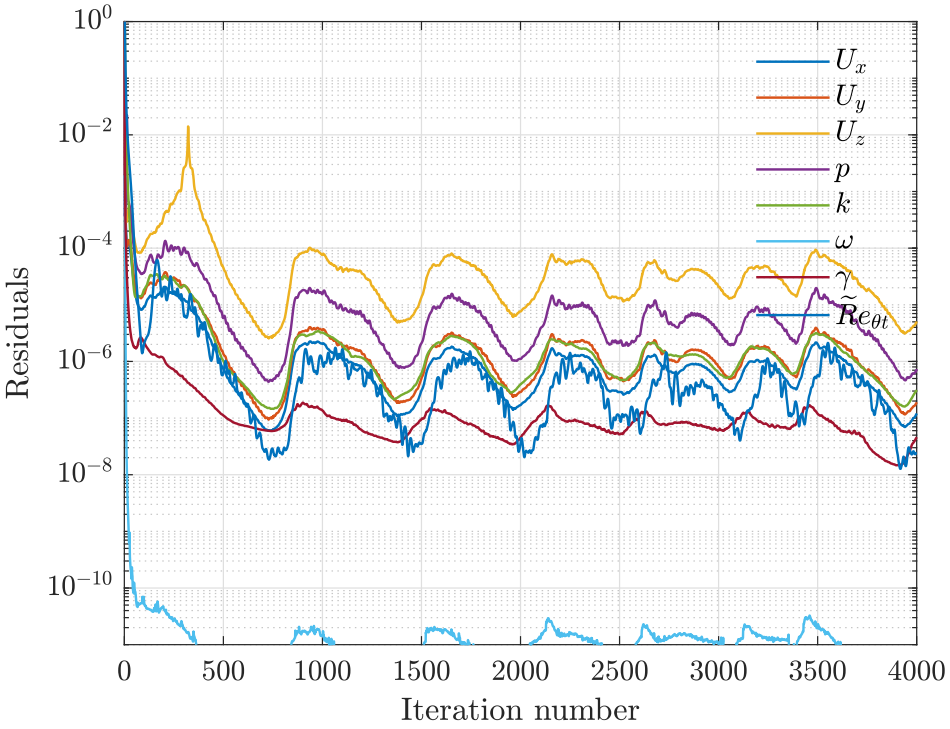

Figure 4.21: Residuals for case $\mathrm{Re} = 1 \times 10^5, \alpha = 24°$.

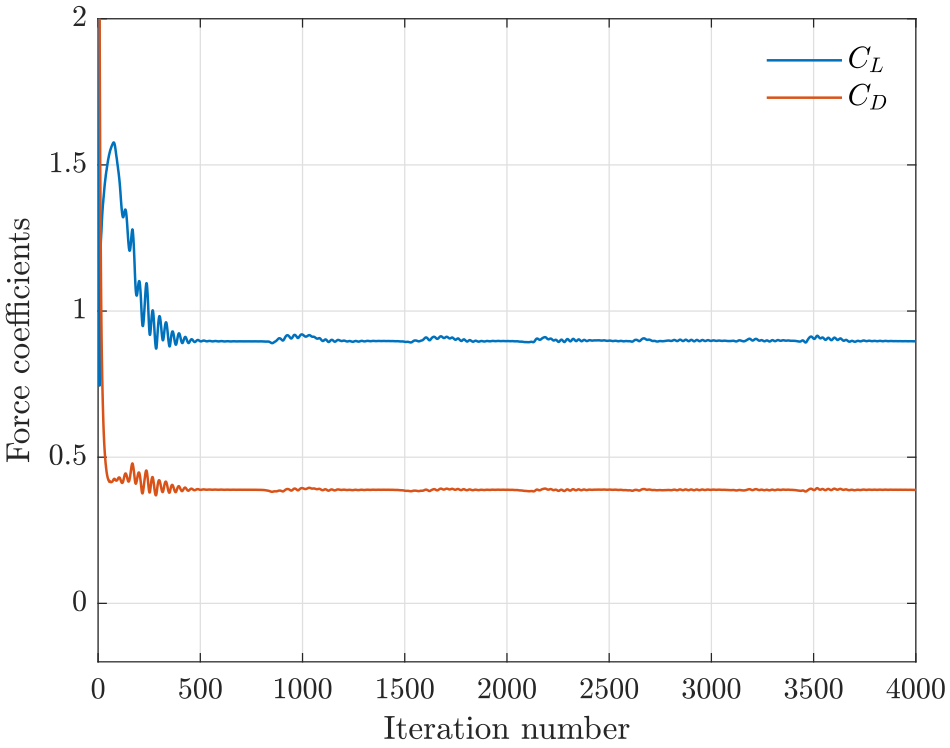

Figure 4.22: Force coefficients throughout the simulation for case $\mathrm{Re} = 1 \times 10^5, \alpha = 24°$.

4.4 Mesh sensitivity study

Using simulation settings outlined in the previous sections as a basis, multiple variations of mesh and boundary conditions were tested to verify sensitivity of the solution results to various parameters. Influence on the solution of mesh resolution, growth rate of the boundary layer cells and boundary conditions is presented in the following sections. All simulations were done for Reynolds number equal to 3 million at 10° angle of attack, which is a very common flow regime for the LEI V3A kite [6].

To ensure good resolution of the boundary layer, it is necessary that the first few cells extruded off the surface have sufficiently small height. That height is usually measured using non-dimensional wall units, y^+, and the requirement is typically defined for the first cell as follows:

$$y^+ = \frac{u^* \Delta s}{\nu} < 1, \tag{4.7}$$

where u^* is the friction velocity and Δs is the height of the first cell. Friction velocity is not known prior to running a simulation and is defined as:

$$u^* = \sqrt{\frac{\tau_w}{\rho}}. \tag{4.8}$$

An estimate of this quantity can be made using flat plate boundary layer relations from White [96]:

$$\mathrm{Re}_x = \frac{U_\infty L}{\nu}, \tag{4.9}$$

$$C_f = \frac{0.027}{\mathrm{Re}_x^{1/7}}, \tag{4.10}$$

$$\tau_w = \frac{C_f \rho U_\infty^2}{2}, \tag{4.11}$$

where C_f is the skin friction coefficient. Knowing τ_w allows to calculate u^* and subsequently Δs. This value was used for the initial guess of the first cell height, and after a few simulations was adjusted to ensure $y^+ < 1$ across the whole kite surface for each computational mesh used in this thesis.

4.4.1 Mesh resolution

In order to evaluate the effect of mesh resolution on the simulation result, a mesh convergence study was conducted using the $\gamma - \widetilde{\mathrm{Re}}_{\theta t}$ transition model. Boundary conditions are set up as outlined in Section 4.3.1. Six different meshes were created, with varying number of elements on the kite surface domains. All meshes were extruded using T-Rex algorithm with same first cell height and extrusion parameters as explained in Section 4.2.2. As a result, between 50 and 70 anisotropic layers are extruded, depending on the location. For simulations run for $\mathrm{Re} = 3 \times 10^6$, the average y^+ is about 0.15, with the maximum at 0.35. To achieve that value, the first cell height was set to $\Delta s = 2.09 \times 10^{-6}$ of the reference chord length. Computed lift and drag coefficients can be found in Table 4.4.

The table indicates the number of points along the kite LE and along the chordwise cross section, as well as the number of points defining TE for each refinement level. Mesh dimension metric was defined as a product of the number of points along LE and along the cross section. Figure 4.23 indicates lines along which the points were counted.

Table 4.4: Sensitivity of aerodynamic coefficients to mesh resolution.

Refinement level	LE points	Section points	TE points	LE × section	$C_L[-]$	$C_D[-]$
1	155	60	3	9300	0.9315	0.0935
2	245	84	3	20580	0.9328	0.0931
3	280	105	4	29400	0.9303	0.0924
4	330	120	4	39600	0.9324	0.0942
5	480	160	7	76800	0.9338	0.0928
6	800	240	11	192000	0.9317	0.0928

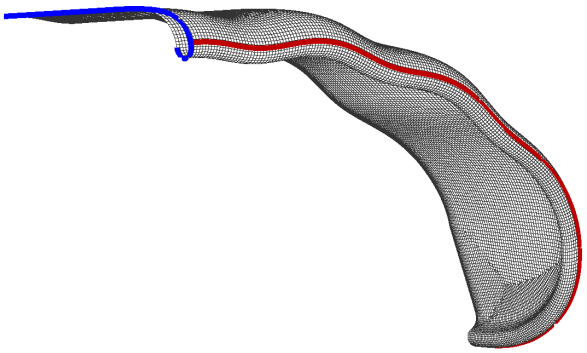

Figure 4.23: Lines used for point count in Table 4.4 (blue – section, red – LE).

Figure 4.24 shows computed lift and drag coefficients normalised against results obtained for refinement level 6 mesh:

$$\widehat{C}_L = C_L/C_{Lref6}, \quad \widehat{C}_D = C_D/C_{Dref6}. \tag{4.12}$$

No distinct mesh convergence trend can be found and the differences between mesh results are within 0.2% for C_L and 1% for C_D. It may seem that even the refinement level 1 mesh is already fine enough for the force coefficients to be converged. However, it is difficult to assess these results for a few reasons. Firstly, it was impossible to obtain results using mesh coarser than refinement level 1. Due to the chosen mesh generation approach, coarsening the mesh significantly reduces the mesh quality until many skew cells are present that cause the simulation to diverge. On top of that, the size of hexahedral cell region would vary depending on the surface domain refinement. As such, the boundary layer cell region near the LE would decrease noticeably with increasing refinement level (Figure 4.25). This is caused by cells extruded off smaller surface cells reaching isotropy faster. As such it is unreasonable to say that results from refinement level 6 are the most accurate, as it may as well be refinement level 3 or 4, which have more layers of cells aligned with the flow. Hence, instead of choosing mesh refinement level based on the convergence study, it was chosen based on resultant mesh topology and quality. Refinement level 4 mesh has satisfactory topology around the kite, provides manageable computational times for 4000 iterations (about 5 hours, with 6 million cells parallelised on 20 cores), fast convergence, and is of very high quality. In fact, mesh quality metrics from Figure 4.16 were obtained for refinement level 4 grid.

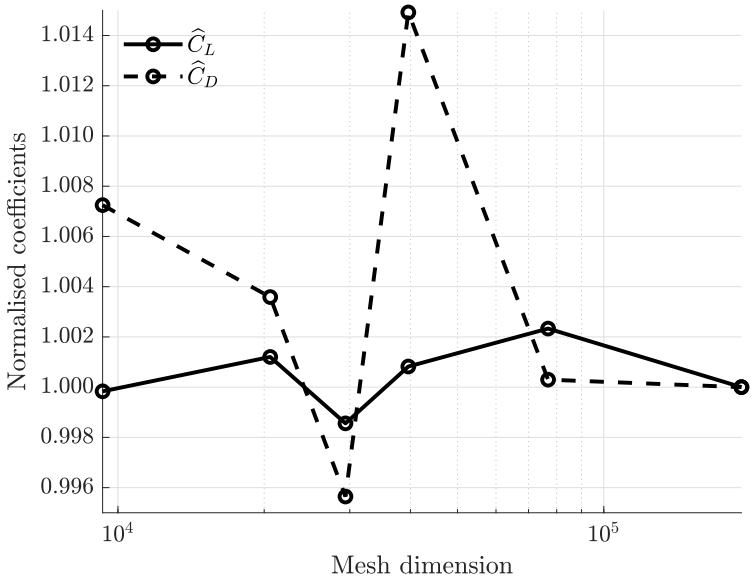

Figure 4.24: Force coefficients normalised against results from refinement level 6.

Another observation from the mesh resolution study was that the tetrahedra region just behind the LE, where extrusion fronts meet, had rapidly increasing element size. This region is quite crucial, as it is placed directly in the LE wake for most considered angles of attack. Additional refinement was added to that region of isotropic cells for the whole span of the kite, as seen on Figure 4.26.

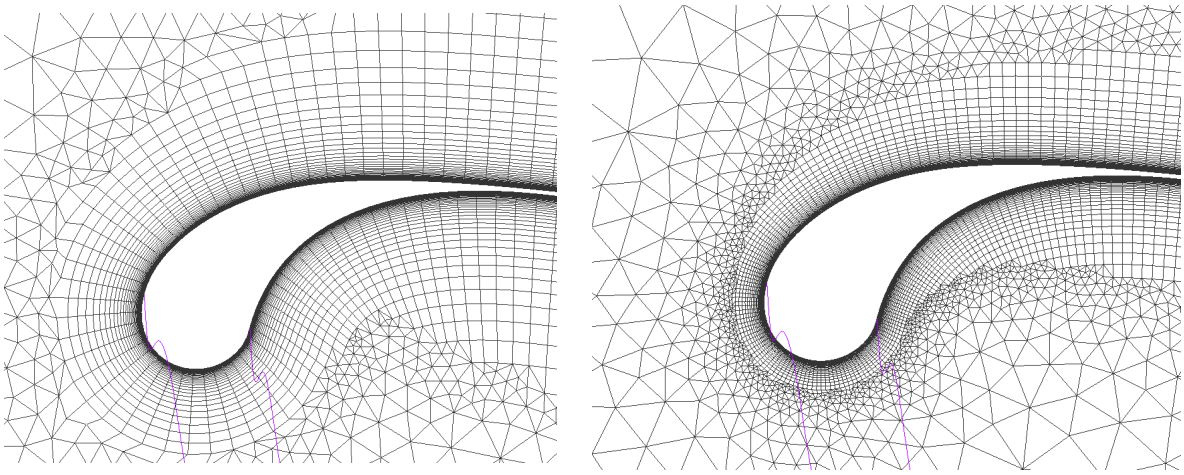

(a) Mesh topology for refinement level 4.

(b) Mesh topology for refinement level 6.

Figure 4.25: Mesh topology at the symmetry plane for different refinement levels.

4.4.2 Growth ratio

The influence of the boundary layer cells growth ratio on the results has been investigated. Lift and drag coefficients computed on refinement level 4 grid with growth ratios set to 1.10, 1.15 and 1.20 are presented in Table 4.5. The results are within 0.2% for C_L and up to 1.5% for C_D. As such the growth ratio of 1.15 is assumed to be sufficient for further simulations and was chosen because it provides higher mesh quality than other options.

Table 4.5: Effect of boundary layer cells growth ratio on computed force coefficients.

Growth ratio	$C_L[-]$	$C_D[-]$	$\Delta C_L[\%]$	$\Delta C_D[\%]$
1.10	0.9345	0.0956	+0.23%	+1.49%
1.15	0.9324	0.0942	-	-
1.20	0.9349	0.0948	+0.27%	+0.64%

4.4.3 Boundary conditions

The effect of varying turbulence boundary conditions on the results has been investigated on refinement level 5 grid. Computed lift and drag coefficients can be found in Table 4.6. It is apparent that varying eddy viscosity ratio or turbulence intensity has negligible effect on the solution, as relative difference between force coefficients does not exceed 0.27%. It is a consequence of swift decay of the turbulent quantities prescribed at the farfield (Figure 4.27). Such behaviour of boundary conditions is standard in many turbulence models and should not pose a problem, since in external aerodynamics the freestream turbulence levels are very low.

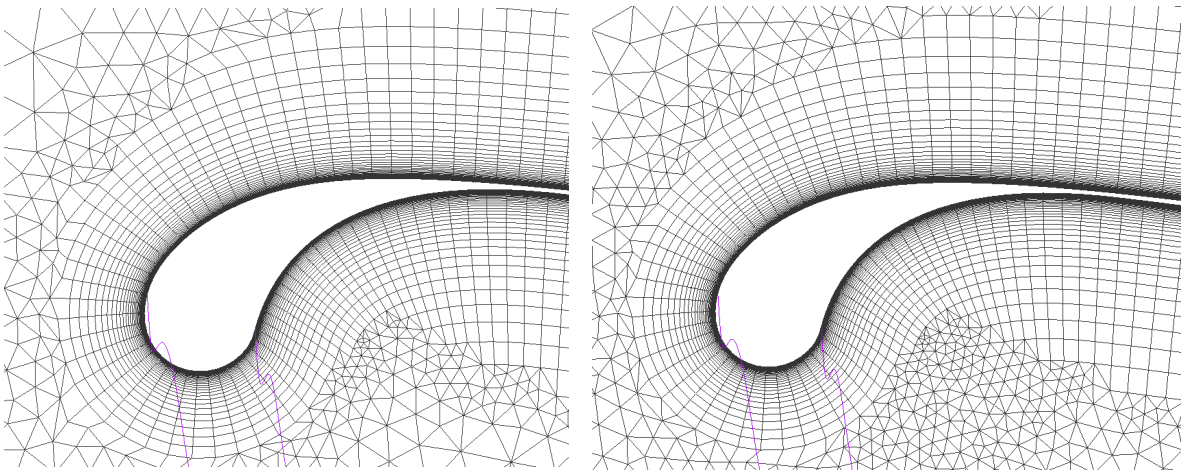

(a) Original refinement level 4 mesh.

(b) Isotropic cells region refinement.

Figure 4.26: Mesh topology at the symmetry plane before and after isotropic region refinement.

Table 4.6: Effect of boundary conditions on computed force coefficients.

Eddy viscosity ratio [−]	$C_L[-]$	$C_D[-]$	$\Delta C_L[\%]$	$\Delta C_D[\%]$
1	0.9333	0.0927	-0.06%	-0.10%
10	0.9338	0.0928	-	-
50	0.9339	0.0928	+0.01%	+0.02%
Turbulence intensity [%]	$C_L[-]$	$C_D[-]$	$\Delta C_L[\%]$	$\Delta C_D[\%]$
0.5	0.9343	0.0926	+0.05%	-0.27%
2	0.9338	0.0928	-	-
20	0.9342	0.0929	+0.04%	+0.07%

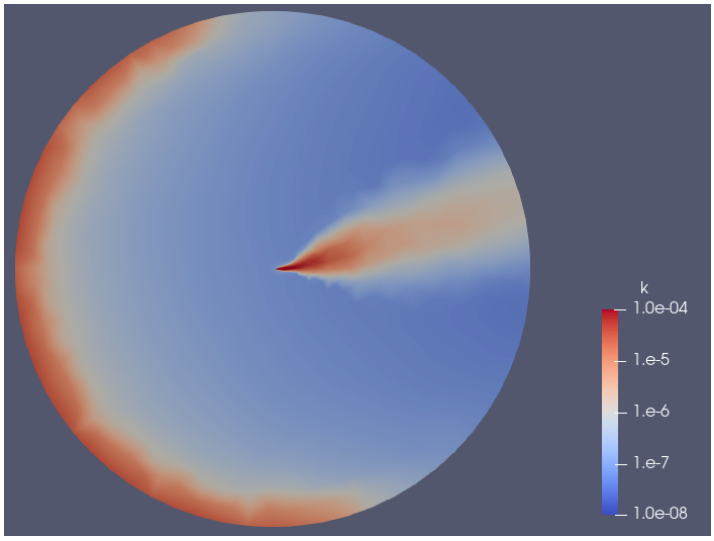

Figure 4.27: Decay of turbulent quantities prescribed on the farfield.

Chapter 5

Results and discussion

In this Chapter, the results that characterise LEI kite aerodynamics are introduced and analysed. Section 5.1 presents the results of various parameters that describe kite aerodynamics at varying flight conditions. The effect of transition modelling on the flow field and kite performance are discussed in Section 5.2. The results are compared with those found in literature in Section 5.3.

5.1 LEI V3A kite aerodynamic performance

The simulation setup outlined in the previous section has been used to analyze the LEI kite for a range of Reynolds numbers and angles of attack. $\gamma - \widetilde{\mathrm{Re}}_{\theta t}$ transition model was used for all the simulations presented in this section. The range of flow conditions includes values representative of LEI V3A kite traction and retraction phases, but is not limited to those. The Reynolds number is varied between $\mathrm{Re} = 10^5$ and $\mathrm{Re} = 15 \times 10^6$ to obtain sets of data similar to Folkersma et al [5] and be able to compare different trends in the results. It also allows to evaluate the effect of transition modelling at various flow conditions. Angle of attack is varied between -5° and 24° to capture the full spectrum of force coefficients at different Reynolds numbers and to investigate the flow field at stall conditions.

5.1.1 Integral force coefficients

Computed lift and drag polars are presented on Figure 5.1. There is a large difference in the maximum lift coefficient for Reynolds numbers 1×10^5 and 5×10^5. Very early stall for $\mathrm{Re} = 1 \times 10^5$, at $\alpha = 6^\circ$, can be explained by flow separation happening off the laminar boundary layer, which is less resistant to adverse pressure gradients than a turbulent one. In addition,

the boundary layer in this case is less stable due to existence of a large laminar separation bubble on the suction side of the kite, which can be seen on Figure 5.2. For $\mathrm{Re} = 5 \times 10^5$, the laminar separation bubble is much smaller, as indicated on Figure 5.3. At this Reynolds number, the flow separates off the turbulent boundary layer, which would explain much higher stall angle $\alpha = 18°$. Increasing Reynolds number to $\mathrm{Re} = 1 \times 10^6$ further increases the maximum lift coefficient. For higher Reynolds numbers, up to $\mathrm{Re} = 10 \times 10^6$, the stall angle actually decreases, until it starts increasing again at $\mathrm{Re} = 15 \times 10^6$. Folkersma et al [5] argued that this behaviour can be explained by flow transition. His 2D analysis indicated that with standard $k - \omega$ SST model, the maximum lift coefficient steadily increased with increasing Reynolds number, which substantially changed once transition modelling was turned on and laminar flow phenomena were present.

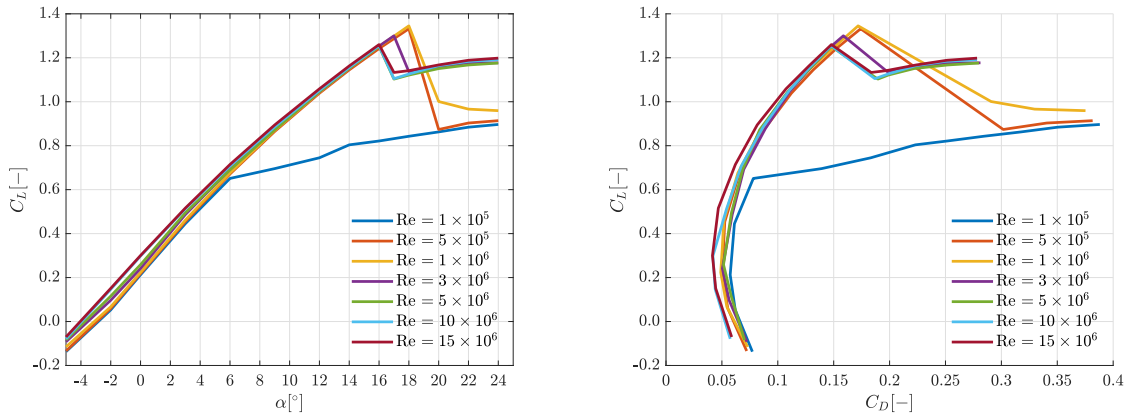

(a) **(b)**

Figure 5.1: Lift (a) and drag (b) polars for the LEI V3A kite computed at various Reynolds numbers.

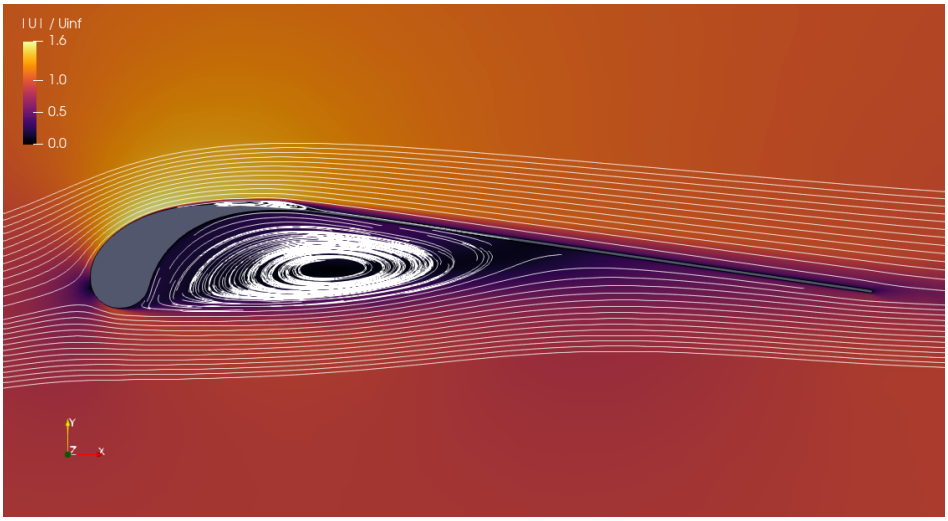

Figure 5.2: Streamlines and normalised flow velocity contour around the kite near the symmetry plane, computed for $\mathrm{Re} = 1 \times 10^5$ and 6° angle of attack.

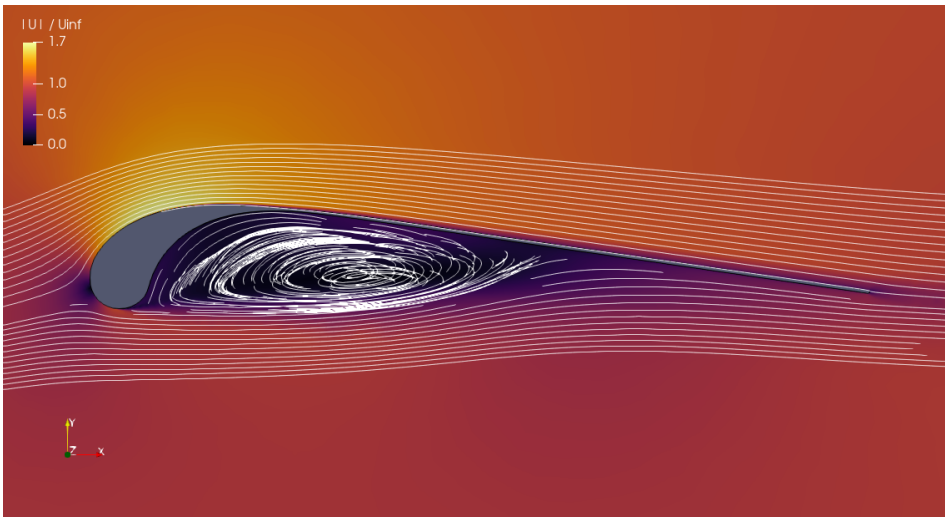

Figure 5.3: Streamlines and normalised flow velocity contour around the kite near the symmetry plane, computed for $\mathrm{Re} = 5 \times 10^5$ and 6° angle of attack.

To analyse the flow transition, one can investigate the chordwise skin friction coefficient along kite surface. It can be calculated as:

$$C_f = \frac{\tau_{w,x}}{\frac{1}{2}\rho U_\infty^2}, \tag{5.1}$$

where $\tau_{w,x}$, wall shear stress in the chordwise direction, is defined as:

$$\tau_{w,x} = \mu \left.\frac{\partial U_x}{\partial y}\right|_{y=0}. \tag{5.2}$$

Negative C_f indicates regions of flow recirculation, while a sudden increase in skin friction represents laminar to turbulent transition. Figure 5.4 presents skin friction coefficient at the symmetry plane for $\alpha = 6°$ for various Reynolds numbers. It can be observed that the laminar separation bubble begins at approximately same point, namely $x = 0.16$, and its size quickly diminishes with increasing Reynolds number. At $\mathrm{Re} = 1 \times 10^6$ it is almost non-existent. According to Folkersma et al [5], this, in conjunction with the longest laminar boundary layer, could explain the highest maximum lift coefficient and low drag coefficient, compared to other polar curves. Increasing the Reynolds number until $\mathrm{Re} = 10 \times 10^6$ moves the transition point towards the LE, resulting in shorter laminar boundary layer and lower maximum lift coefficient. At $\mathrm{Re} = 10 \times 10^6$ the transition occurs very close to the LE, so the boundary layer becomes close to fully turbulent. Increasing Reynolds number for a fully turbulent boundary layer should result in an increased maximum lift coefficient and stall angle, which is exactly what happens on Figure 5.1, when comparing polars of $\mathrm{Re} = 10 \times 10^6$ and $\mathrm{Re} = 15 \times 10^6$.

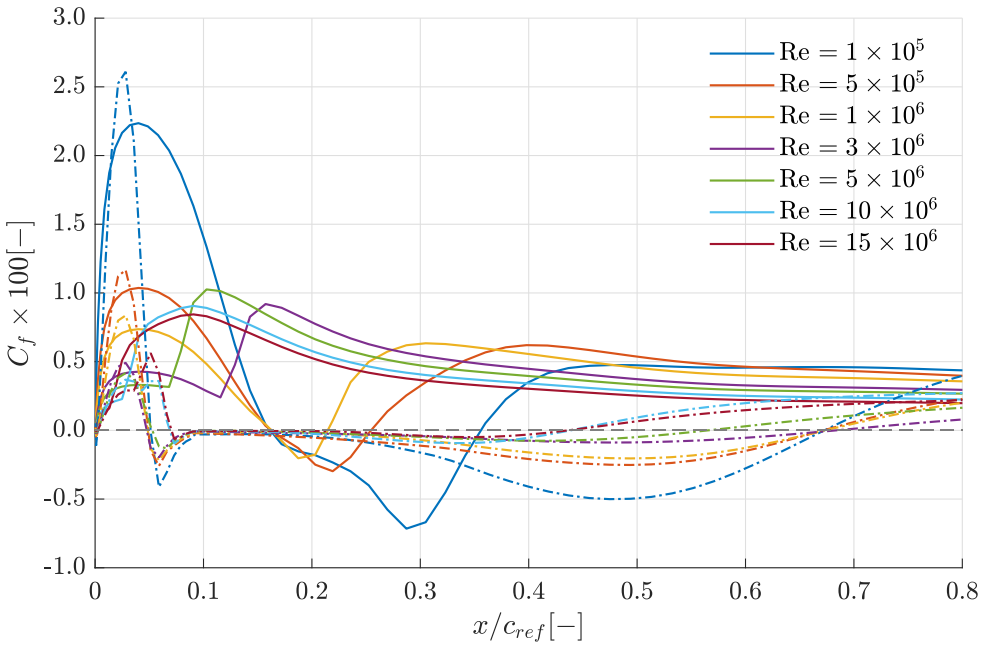

Figure 5.4: Skin friction coefficient along kite surface at the symmetry plane for 6° angle of attack. Solid and dashed lines represent the suction and pressure sides of the kite, respectively.

Another feature that becomes apparent when looking at the drag polars is a noticeable gap between drag coefficients at low angles of attack for $\mathrm{Re} = 10 \times 10^6$ and for lower Reynolds numbers. Folkersma et al [5] argued that this difference can be explained by drag crisis occurring at the cylindrical LE tube. Its diameter at the symmetry plane is about 0.07 chord lengths, which means the equivalent Reynolds number for the LE tube is equal to $\mathrm{Re}_{\mathrm{LE}} = 7 \times 10^5$, for chord-based $\mathrm{Re} = 10 \times 10^6$. This corresponds to critical flow around a cylinder [26], where it experiences significantly reduced drag and smaller recirculation zone downstream. It is caused by the laminar to turbulent flow transition occurring before the typical laminar separation point, resulting in the separation point moving significantly further downstream. As expected, the recirculation zone is much smaller for $\mathrm{Re} = 10 \times 10^6$, compared to lower Reynolds numbers (Figure 5.5). For Reynolds numbers lower than $\mathrm{Re} = 10 \times 10^6$, the flow separates off the laminar boundary layer on the pressure side of the LE tube, hence the increased drag coefficient and larger recirculation zone on the pressure side.

5.1.2 Flow 3D effects

In this section, main flow features will be identified using results computed for Reynolds number of 3×10^6 and 12° angle of attack, which is a very common flow regime for LEI V3A kite in the traction phase. Since the U_∞ boundary condition is set to unity in all the simulations carried out, every figure in this and the following sections will depict flow veloc-

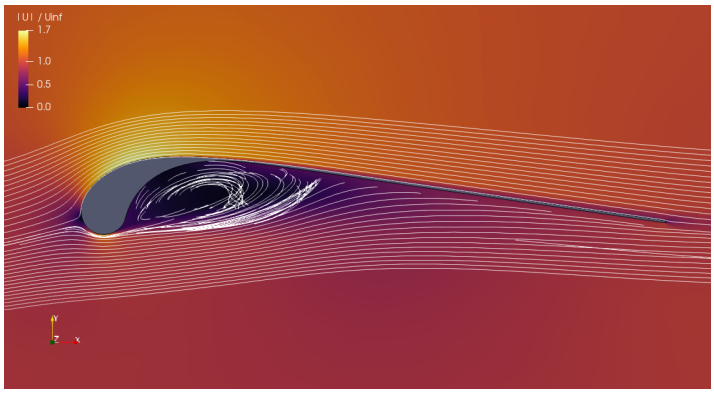

Figure 5.5: Streamlines and normalised flow velocity contour around the kite at the symmetry plane, computed for $\mathrm{Re} = 10 \times 10^6$ and 6° angle of attack.

ity normalised against the freestream velocity, unless explicitly stated otherwise. In order to get a good idea of the global flow field behaviour around the kite, it is useful to look at streamlines originating from a horizontal line downstream of the kite (Figure 5.6), coloured for U_z, the component of the velocity normal to the symmetry plane. It is apparent that at such angle of attack, the portion of the flow going above the kite surface tends inwards, while the flow going below generally tends outwards. This global trend in the wake can be clearly seen by looking at the U_z component contour downstream of the kite (Figure 5.7a). Such flow behaviour is caused by the pressure gradients imposed on the flow by the kite surfaces aligned at a positive angle of attack with the freestream. It creates a distinct region of high magnitude x-component of the vorticity that slowly decays downstream of the kite (Figure 5.7b).

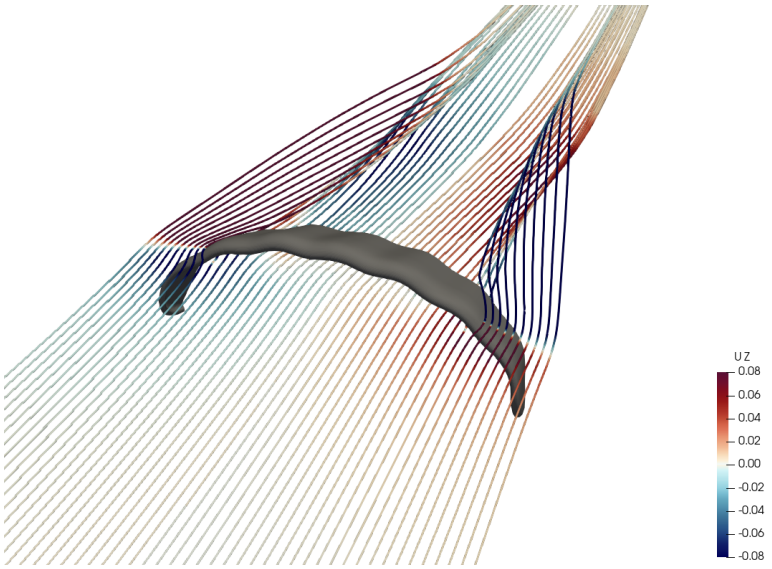

Figure 5.6: Streamlines around the kite coloured for the spanwise velocity component, computed for $\mathrm{Re} = 3 \times 10^6$ and 12° angle of attack.

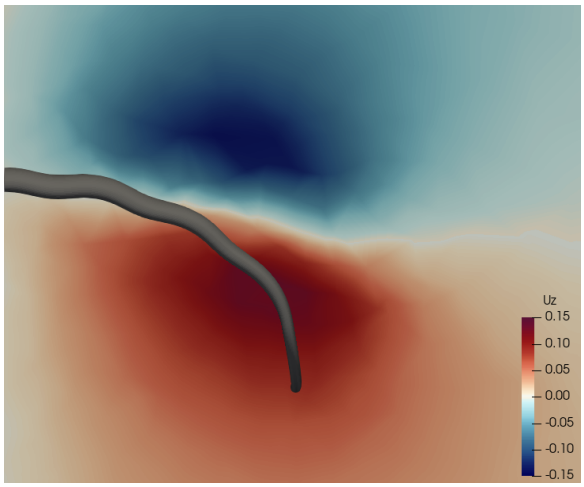

(a) U_z contour in the wake of the kite.

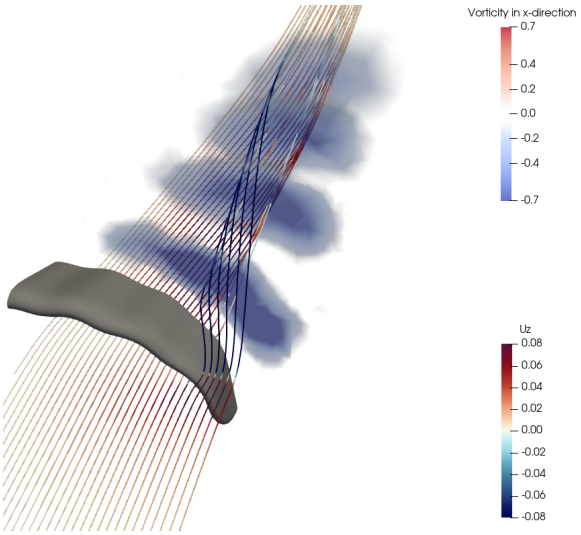

(b) Streamlines around the kite coloured for the spanwise velocity component with vorticity in x-direction contours.

Figure 5.7: Wake visualisation computed for $\mathrm{Re} = 3 \times 10^6$ and 12° angle of attack.

Another important feature of the flow is a persistent flow recirculation zone behind the LE, present at all angles of attack considered. Its size is not uniform across the kite span, as it can be seen on Figure 5.8, which presents the variation of the chordwise component of the velocity at $x = 0.3$ cross section. Streamwise extent of the recirculation zone is visualized on Figure 5.9, which shows a surface plot of the skin friction coefficient. Values below 0 indicate regions of flow reversal. Length of the recirculation zone varies periodically throughout the kite span and it seems to be linked to the wavy shape of the kite.

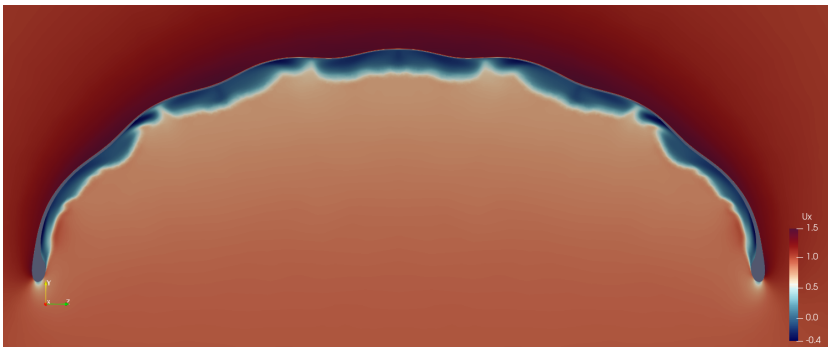

Figure 5.8: U_x contour across the kite span at $x = 0.3$, computed for $\mathrm{Re} = 3 \times 10^6$ at 12° angle of attack.

In close vicinity of the kite a lot of variation in the cross flow is present, compared to the wake. Waviness of the kite surface forces back and forth behaviour of the z-component of the velocity (Figure 5.10). There are distinct regions of positive and negative x-components of vorticity (Figure 5.11), that cause the non-uniformity of the recirculation zone behind

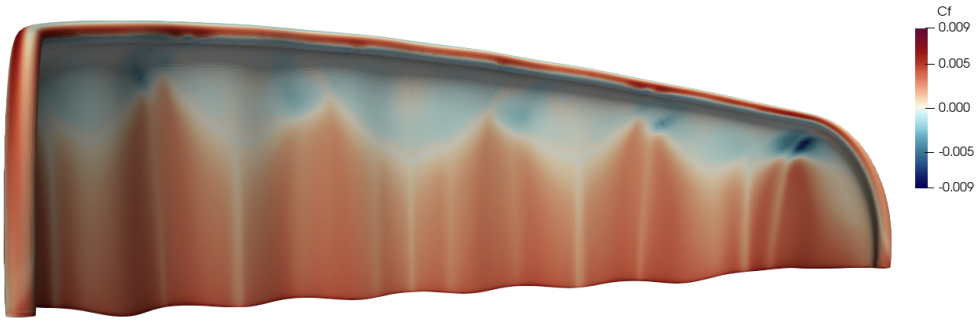

Figure 5.9: C_f across the kite bottom surface, computed for $\mathrm{Re} = 3 \times 10^6$ and 12° angle of attack.

the LE. Figure 5.12 presents the U_x contour at $x = 0.3$ plane in grayscale, coloured with the x-component of vorticity. It can be observed that in regions where negative and positive vorticity fronts meet (looking from left to right), the flow tends towards the kite surface, lowering the size of recirculation zone. Where positive and negative vorticity fronts collide, the opposite happens and recirculation zone increases in size.

Figure 5.10 also indicates that the assumption of flow symmetry could be invalid as there appears to be a discontinuity at the symmetry plane. This means that U_z velocity component is not converged. It must be caused by the innate transient behaviour of the cross flow, however for the purpose of this analysis that it is assumed to be a sufficient approximation.

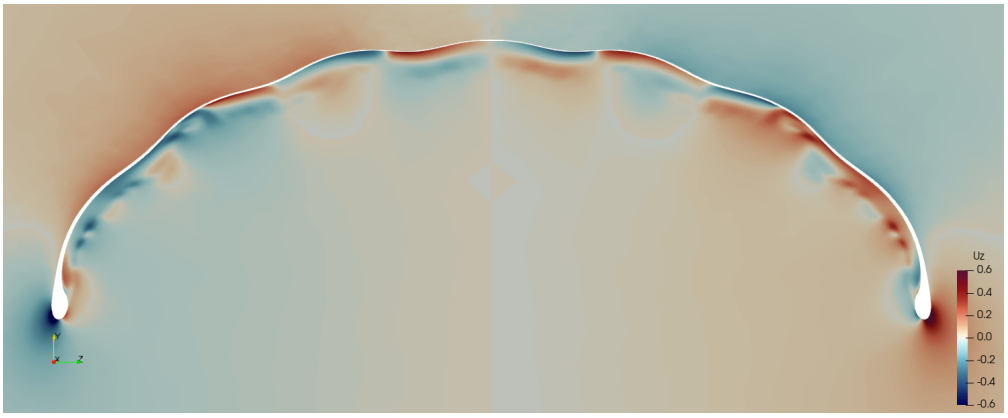

Figure 5.10: U_z contour across the kite span at $x = 0.3$, computed for $\mathrm{Re} = 3 \times 10^6$ and 12° angle of attack.

Vortical structures at the pressure side of the kite can be further visualised using Q-criterion, which is defined as the second invariant of the velocity field gradient. In flow regions where Q is positive, the vorticity magnitude is greater than the magnitude of strain rate, indicating a vortex. Figure 5.13 shows Q-criterion visualisation of the vortical structures on the pressure side of the kite. A few distinct streamwise vortices can be observed that noticeably lower the chordwise velocity component, as seen on Figure 5.13c.

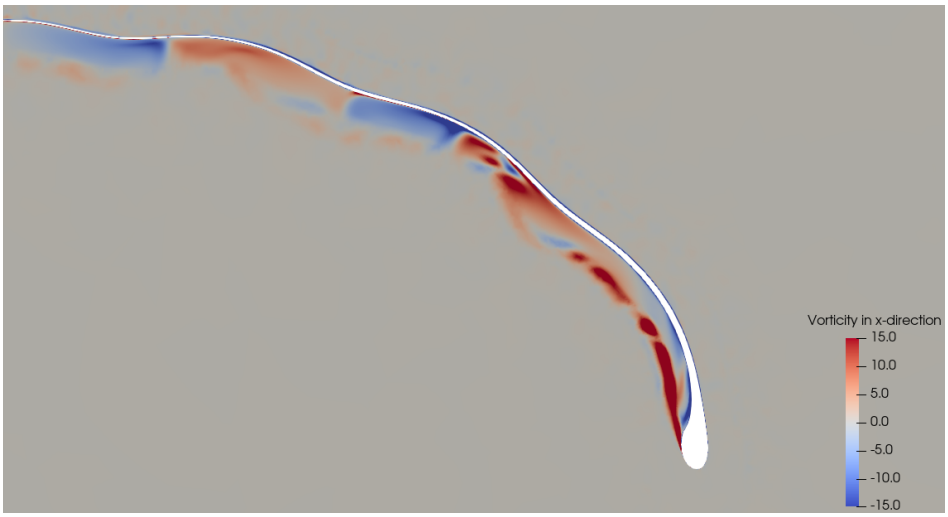

Figure 5.11: Vorticity in chordwise direction contour across the kite span at $x = 0.3$, computed for $\mathrm{Re} = 3 \times 10^6$ and 12° angle of attack.

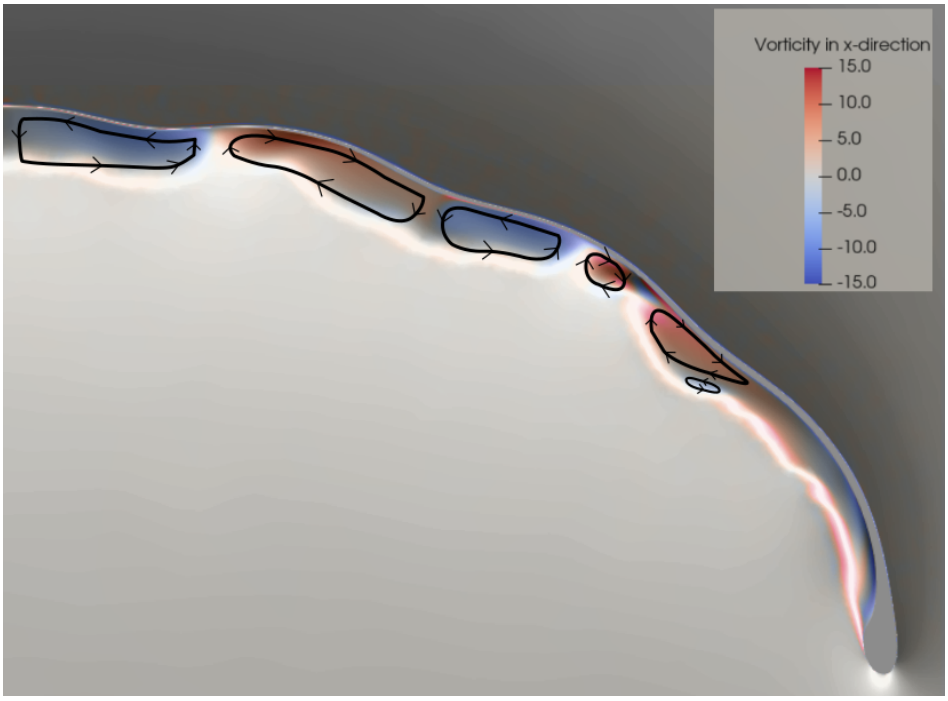

Figure 5.12: U_x contour contour across the kite span at $x = 0.3$ coloured with vorticity in chordwise direction, computed for $\mathrm{Re} = 3 \times 10^6$ and 12° angle of attack.

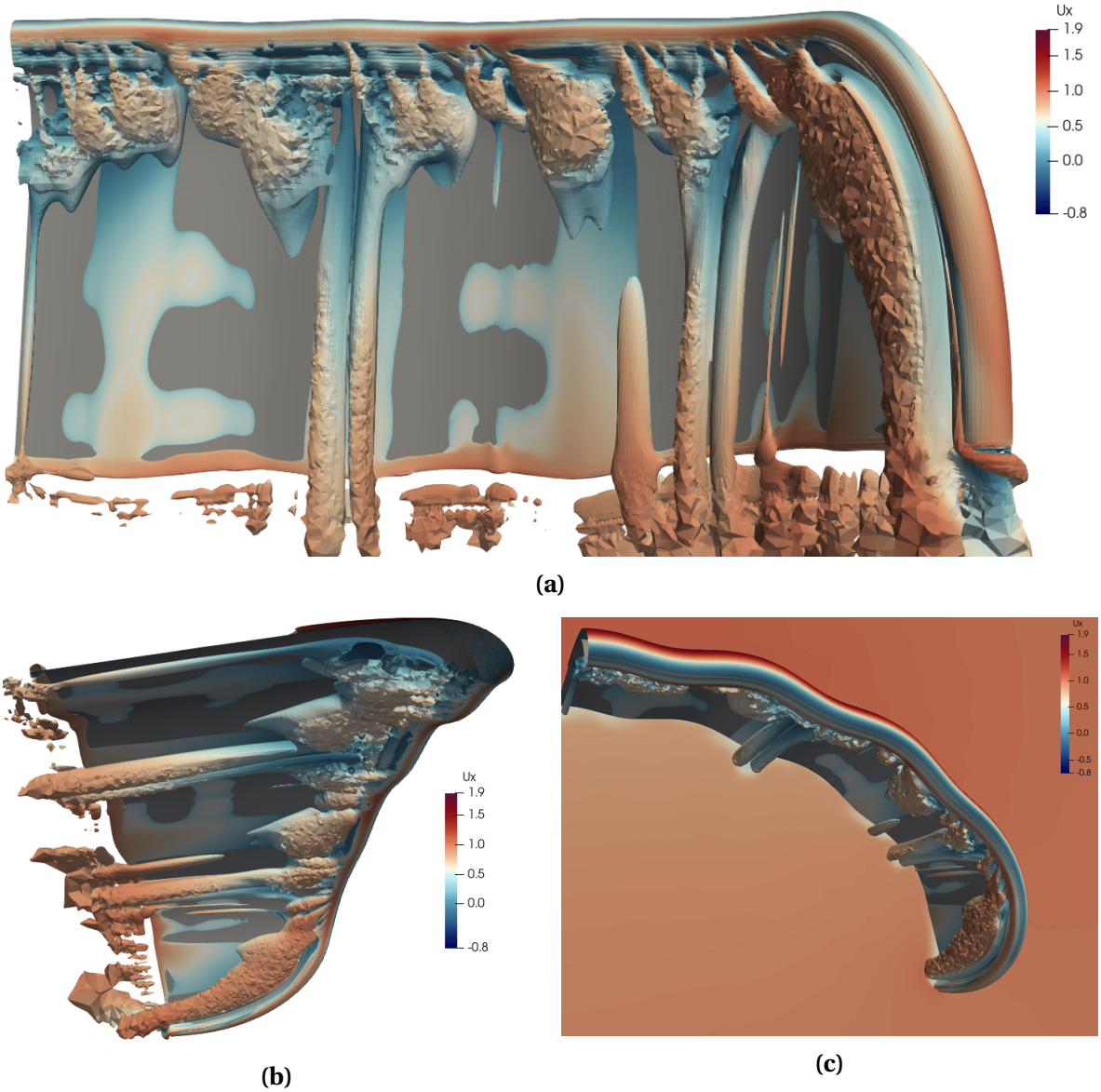

Figure 5.13: Positive Q-criterion isovolumes on the pressure side of the kite seen from below (a), a side (b) and coupled with U_x velocity contour (c), computed for $\mathrm{Re} = 3 \times 10^6$ and 12° angle of attack.

5.1.3 Flow separation

In this section the nature of the flow separation for different Reynolds numbers, on both suction and pressure side of the kite, is discussed. Figure 5.14 presents the flow field near the symmetry plane and skin friction coefficient plots on the kite surface in stall conditions at various Reynolds numbers. Negative skin friction coefficient indicates regions of flow separation. The size of the separation zone decreases with increasing Reynolds number. It is caused by higher Reynolds number flows having thinner boundary layer that is more resistant to adverse pressure gradients. However, the difference between $\mathrm{Re} = 3 \times 10^6$ and higher is barely noticeable and close to negligible. In case of $\mathrm{Re} = 1 \times 10^5$, the flow over whole suction side of the kite is detached because the separation occurs off the laminar boundary layer, which has lower velocity gradients than turbulent and separates more easily. For higher Reynolds numbers the flow at the tip remains attached in stall conditions, because the bowed shape of the kite causes the tip to experience more favourable pressure gradients than the rest of the kite. In stall conditions, separation generally happens near the mid-span of the kite and its size is not uniform in the spanwise direction.

Figure 5.15 shows skin friction graphs for the pressure side of the kite for various Reynolds numbers at 12° angle of attack. It can be used to evaluate the streamwise length of the recirculation zone behind the LE. As mentioned in Section 5.1.1, the recirculation zone noticeably diminishes in length when Reynolds number increases from $\mathrm{Re} = 5 \times 10^6$ to $\mathrm{Re} = 10 \times 10^6$. It can be attributed to delayed flow separation on the cylindrical LE, caused by the drag crisis. It is apparent that for $\mathrm{Re} = 5 \times 10^6$, the separation across the LE happens quite early, indicating laminar separation. For $\mathrm{Re} = 10 \times 10^6$, there are multiple regions of separation occurring much later, which means the boundary layer transitions to turbulent before the flow separates off the LE. For $\mathrm{Re} = 15 \times 10^6$, this happens throughout close to the whole span of the kite. Decreased size of the recirculation zone behind the LE can also be observed when investigating Q-criterion isovolumes for different Reynolds numbers (Figure 5.16).

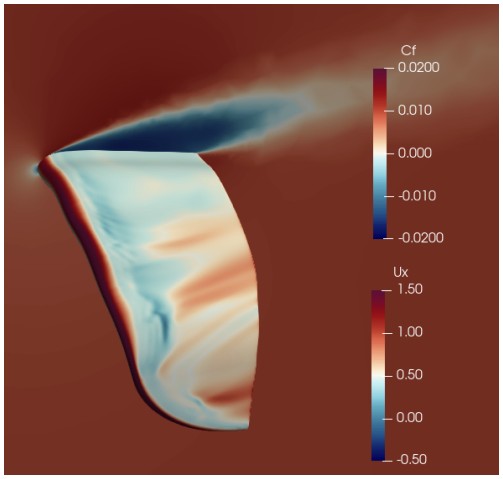

(a) $\mathrm{Re} = 1 \times 10^5, \alpha = 9°$

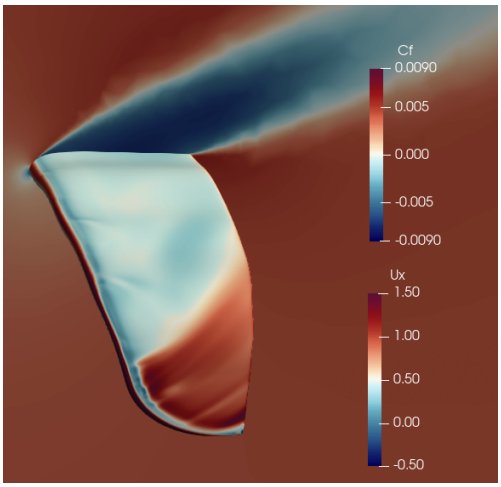

(b) $\mathrm{Re} = 5 \times 10^5, \alpha = 20°$

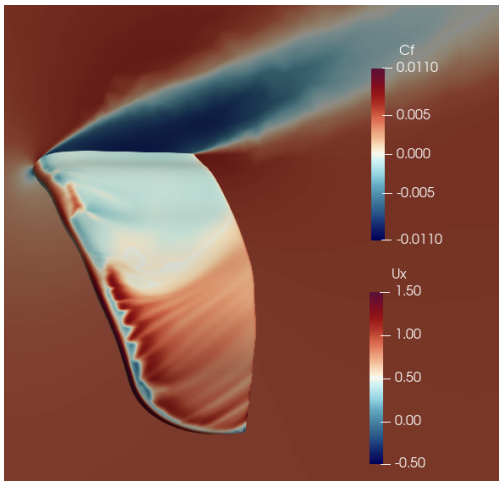

(c) $\mathrm{Re} = 1 \times 10^6, \alpha = 20°$

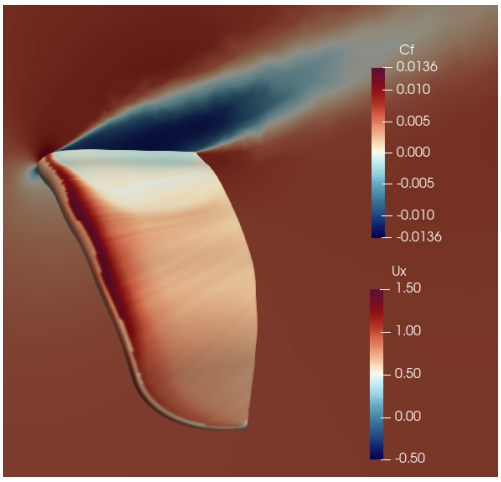

(d) $\mathrm{Re} = 3 \times 10^6, \alpha = 20°$

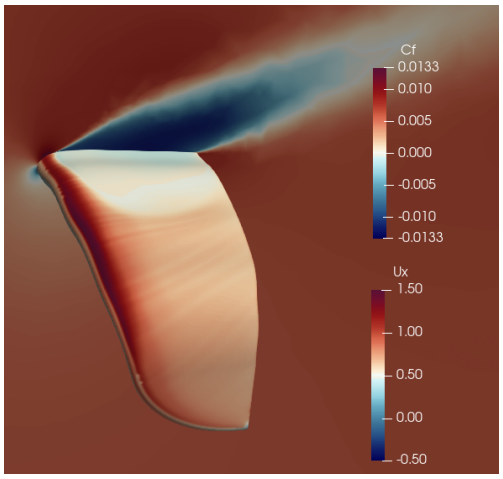

(e) $\mathrm{Re} = 5 \times 10^6, \alpha = 20°$

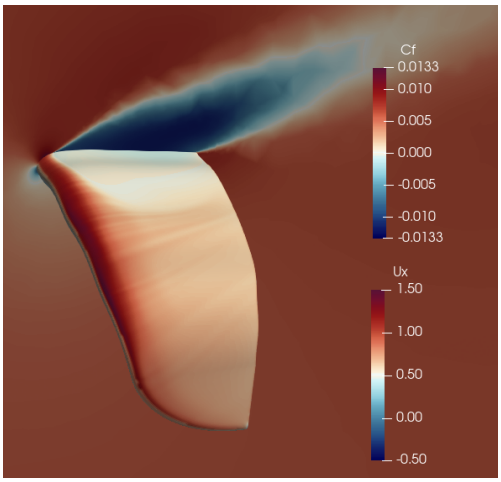

(f) $\mathrm{Re} = 10 \times 10^6, \alpha = 20°$

Figure 5.14: U_x contours near the symmetry plane and skin friction coefficient surface plots, computed for various Reynolds numbers in stall conditions.

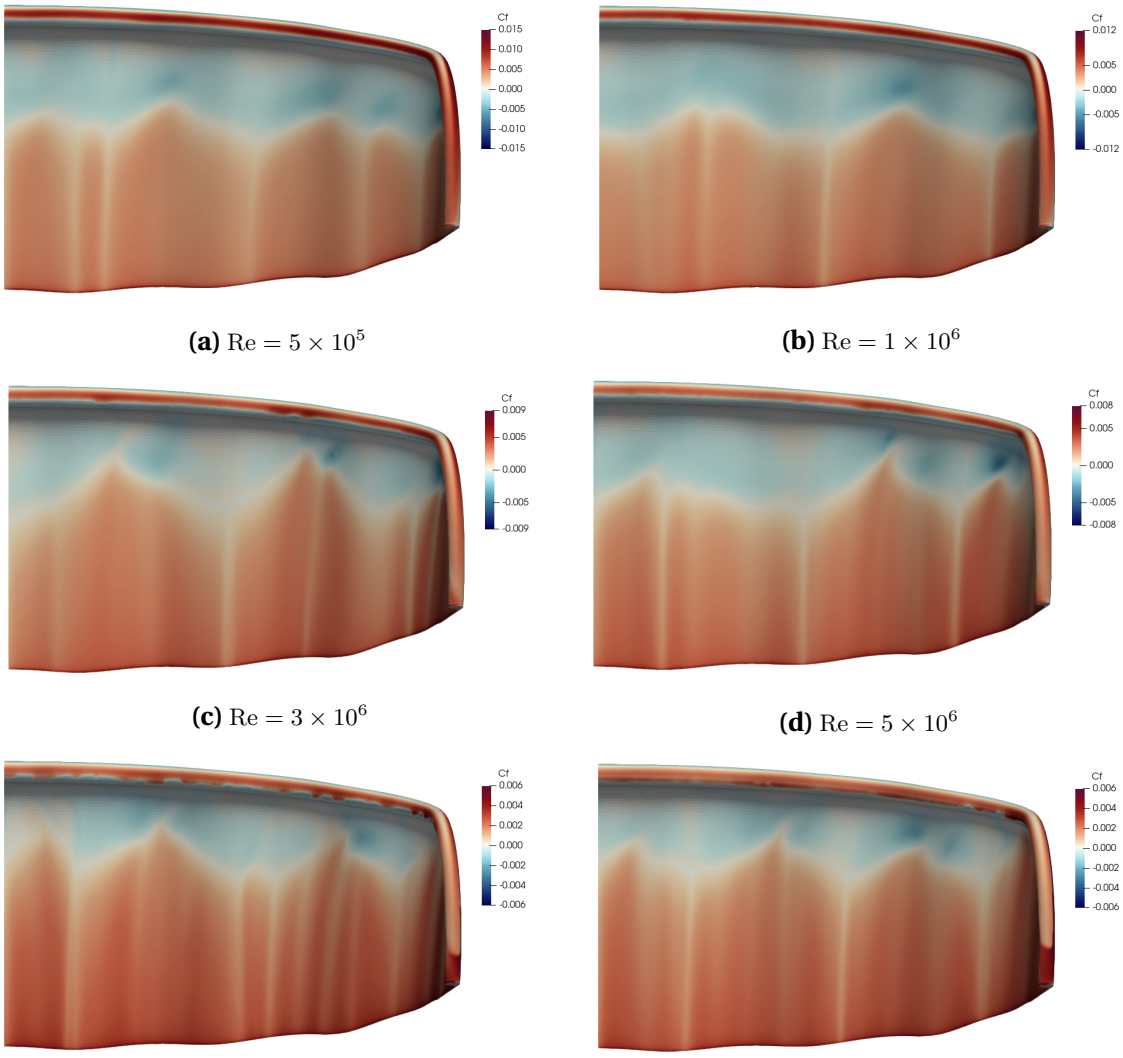

(a) $\mathrm{Re} = 5 \times 10^5$ **(b)** $\mathrm{Re} = 1 \times 10^6$

(c) $\mathrm{Re} = 3 \times 10^6$ **(d)** $\mathrm{Re} = 5 \times 10^6$

(e) $\mathrm{Re} = 10 \times 10^6$ **(f)** $\mathrm{Re} = 15 \times 10^6$

Figure 5.15: Skin friction coefficient at the pressure side of the kite computed for various Reynolds numbers at 12° angle of attack.

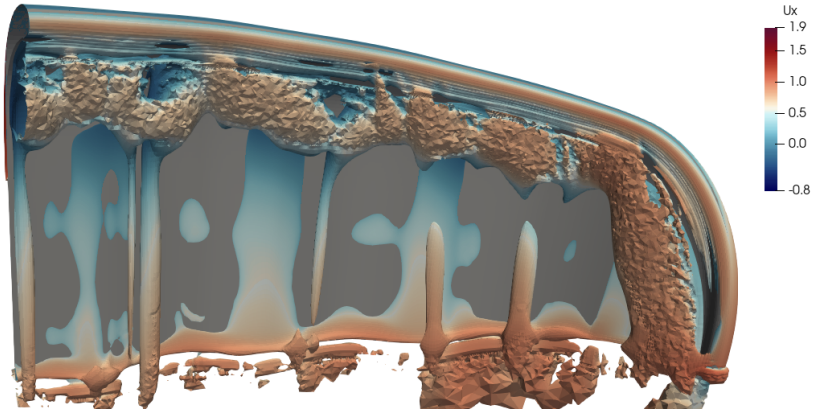

(a) $\mathrm{Re} = 5 \times 10^5$

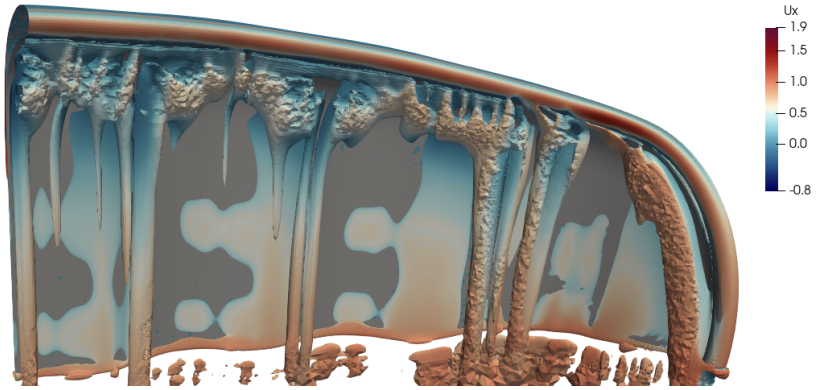

(b) $\mathrm{Re} = 15 \times 10^6$

Figure 5.16: Positive Q-criterion isovolumes on the pressure side of the kite computed for various Reynolds numbers at 12° angle of attack.

5.2 Effect of transition modelling

In this section the impact of transition modelling on the LEI V3A kite aerodynamic performance and flow field is evaluated. To make it possible, CFD simulations using $k-\omega$ SST turbulence model, the 2003 model variant [76], without transition modelling are run for the following Reynolds numbers and angles of attack:

- $\mathrm{Re} = 5 \times 10^5, \alpha = 0°, 12°, 20°$.
- $\mathrm{Re} = 3 \times 10^6, \alpha = 0°$ to $24°$.
- $\mathrm{Re} = 10 \times 10^6, \alpha = 0°, 12°, 20°$.

The resultant lift and drag polars are presented on Figure 5.17. Lift coefficient data with and without transition modelling agree closely for angles of attack before stall for all Reynolds numbers considered. The integral drag coefficient computed with $k-\omega$ SST is underpredicted by up to 9% for $\mathrm{Re} = 3 \times 10^6$ at angles of attack before stall, compared to $\gamma - \widetilde{\mathrm{Re}}_{\theta t}$ results. For $\mathrm{Re} = 3 \times 10^6$, the transition model predicts stall $1°$ later than regular $k-\omega$ SST turbulence model. During stall conditions, $k-\omega$ SST overpredicts lift and underpredicts drag for $\mathrm{Re} = 5 \times 10^5$, underpredicts lift and overpredicts drag for $\mathrm{Re} = 3 \times 10^6$, compared to $\gamma - \widetilde{\mathrm{Re}}_{\theta t}$ transition model. Additionally, without transition modelling, the lift coefficient drop during stall is higher for $\mathrm{Re} = 3 \times 10^6$ than with transition modelling. For $\mathrm{Re} = 10 \times 10^6$, lift and drag coefficients match closely for all angles of attack considered.

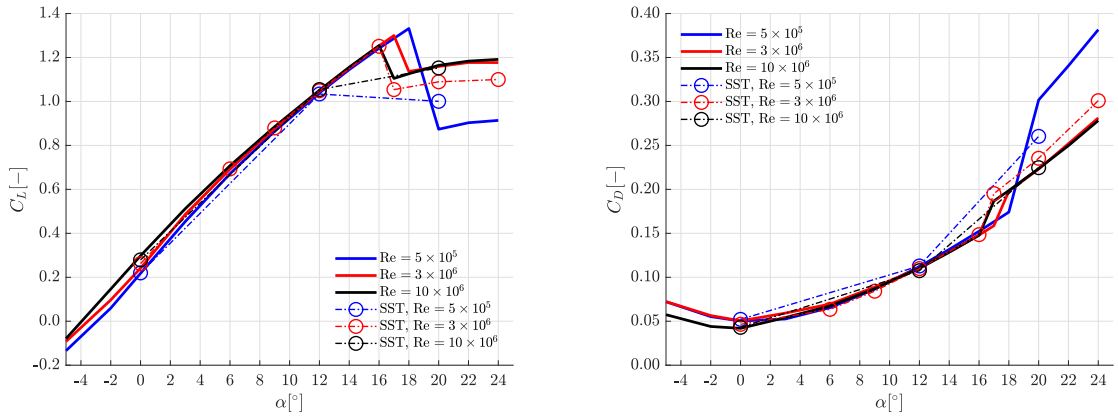

(a) **(b)**

Figure 5.17: Lift (a) and drag (b) polars for the LEI V3A kite computed at various Reynolds numbers with (solid line) and without transition modelling (dashed line).

Although the force coefficients results match fairly closely for different Reynolds numbers, it does not convey a whole lot of information about the flow field around the kite. Figure 5.18 presents skin friction coefficient surface plots for the kite at different Reynolds numbers with and without transition modelling, using the same colour scale for each of the

plots. The $\gamma - \widetilde{\mathrm{Re}}_{\theta t}$ transition model clearly distinguishes different flow features for low and high Reynolds numbers. For $\mathrm{Re} = 5 \times 10^5$ there is a distinct laminar separation bubble across the whole span of the kite that vanishes for $\mathrm{Re} = 3 \times 10^6$, where the boundary layer transitions before the separation. This is not the case for results obtained with $k - \omega$ SST. Since the turbulence model assumes the whole boundary layer is turbulent, there is hardly any difference in skin friction plots between low and high Reynolds numbers – only the magnitude varies, while trends remain the same. Only for $\mathrm{Re} = 10 \times 10^6$ the results with and without transition modelling are similar, because at such high Reynolds number boundary layer transitions very early on the suction side of the kite.

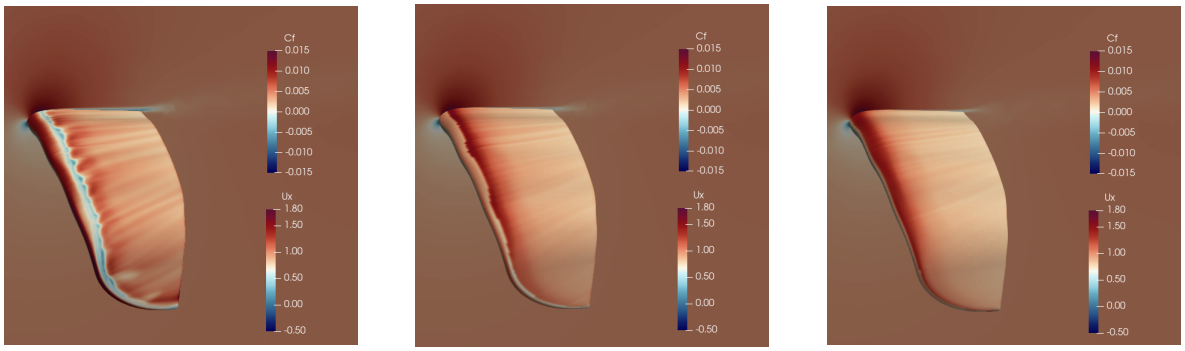

(a) $\mathrm{Re} = 5 \times 10^5$, $\gamma - \widetilde{\mathrm{Re}}_{\theta t}$ **(b)** $\mathrm{Re} = 3 \times 10^6$, $\gamma - \widetilde{\mathrm{Re}}_{\theta t}$ **(c)** $\mathrm{Re} = 10 \times 10^6$, $\gamma - \widetilde{\mathrm{Re}}_{\theta t}$

(d) $\mathrm{Re} = 5 \times 10^5$, $k - \omega$ SST **(e)** $\mathrm{Re} = 3 \times 10^6$, $k - \omega$ SST **(f)** $\mathrm{Re} = 10 \times 10^6$, $k - \omega$ SST

Figure 5.18: Skin friction coefficient at the suction side of the kite computed for various Reynolds numbers at 12° angle of attack with (a, b, c) and without (d, e, f) transition modelling.

Further differences between $\gamma - \widetilde{\mathrm{Re}}_{\theta t}$ and $k - \omega$ SST models become apparent when investigating regions of flow separation across the kite surfaces. For $\mathrm{Re} = 3 \times 10^6$, the flow separation zone on the suction side of the kite in stall conditions is larger without transition modelling (Figure 5.19) than with (Figure 5.14d), which explains increased lift coefficient drop during stall for $k - \omega$ SST. Spanwise shape of recirculation zone on the pressure side of the kite also differs between the two models. Figure 5.20 shows U_x, U_z and vorticity contours at $x = 0.3$ cross section of the flow field. The recirculation zone is thinner on average and the variation of its size occurs at different spanwise locations compared to results with transition modelling. It can be explained by different nature of the cross flow across the kite span. It is also reflected in differences in vorticity contours at $x = 0.3$ plane.

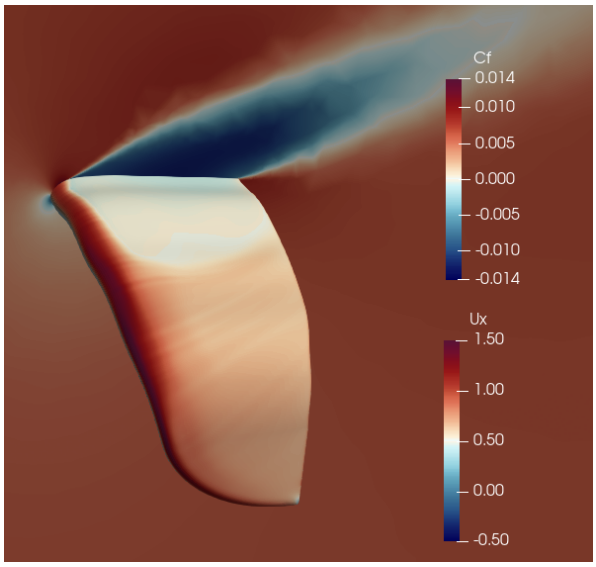

Figure 5.19: U_x contour near the symmetry plane and skin friction coefficient surface plot, computed for $\mathrm{Re} = 3 \times 10^6$ at $\alpha = 20°$ without transition modelling.

Similar to results obtained with transition modelling, the chordwise length of the recirculation zone on the pressure side decreases with increasing Reynolds number, as seen on Figure 5.21. Interestingly, the turbulence model is able to capture, to an extent, the drag crisis happening on the cylindrical LE of the kite. For $\mathrm{Re} = 5 \times 10^5$ the skin friction coefficient, on the pressure side up to $x = 0.1$, as well as the flow separation point, match perfectly for both $k-\omega$ SST and $\gamma - \widetilde{\mathrm{Re}}_{\theta t}$ at the particular cross section considered (Figure 5.21b). This is quite unexpected, given that in this case the separation from the bottom of the LE tube occurs from a laminar boundary layer. For $\mathrm{Re} = 10 \times 10^6$, the separation location matches too, although it is located further downstream, indicating separation from a turbulent boundary layer. There is a discrepancy for $\mathrm{Re} = 3 \times 10^6$, where at the given cross section, $\gamma - \widetilde{\mathrm{Re}}_{\theta t}$ predicts early, laminar, flow separation, while $k-\omega$ SST indicates a turbulent, delayed separation. However, it can be considered a local difference, as the location of flow separation from the LE tube is not uniform along the kite span at this Reynolds number.. Regions of delayed flow separation on the LE tube showed on Figure 5.21c match the results obtained with transition modelling approximately (Figure 5.15c).

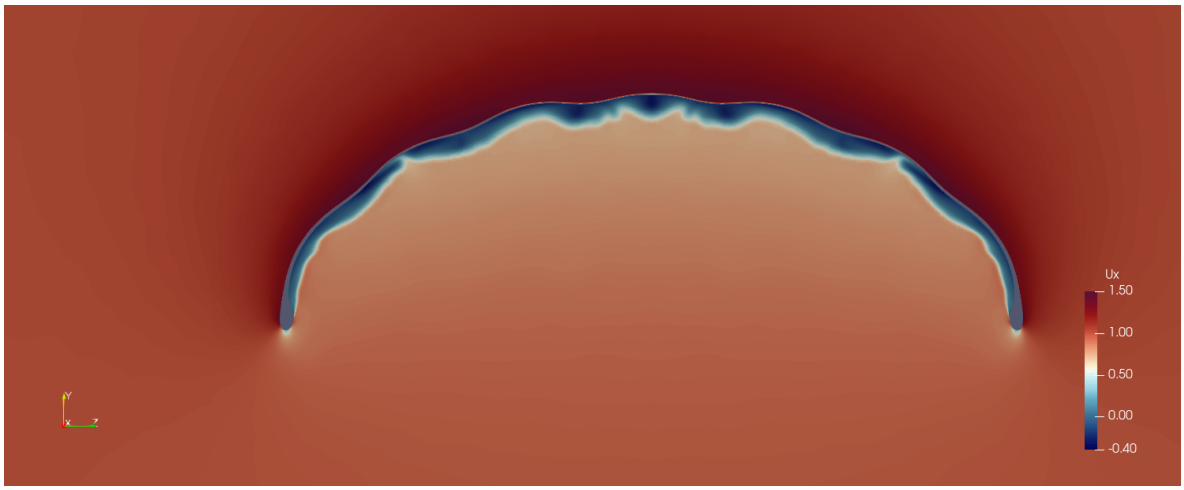

(a) U_x contour.

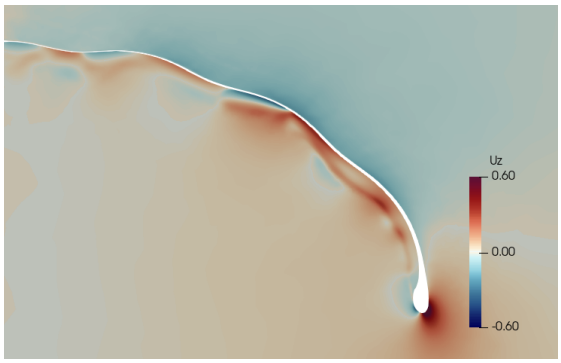

(b) U_z contour.

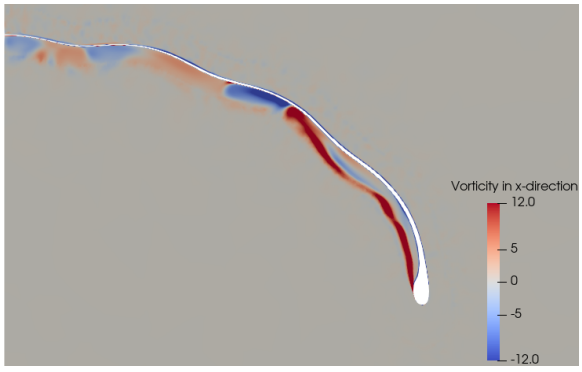

(c) Vorticity in chordwise direction contour.

Figure 5.20: U_x (a), U_z (b) and vorticity (c) contours at $x = 0.3$, computed for $\mathrm{Re} = 3 \times 10^6$ and 12° angle of attack without transition modelling.

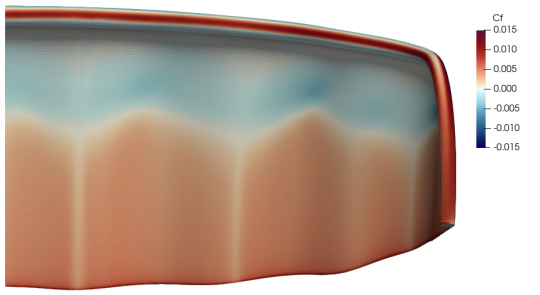

(a) $\mathrm{Re} = 5 \times 10^5$

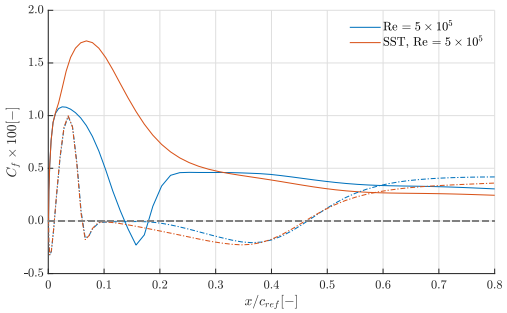

(b) $\mathrm{Re} = 5 \times 10^5$

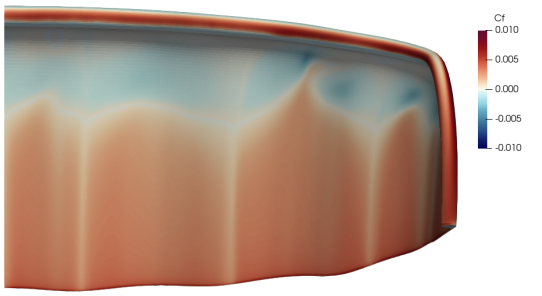

(c) $\mathrm{Re} = 3 \times 10^6$

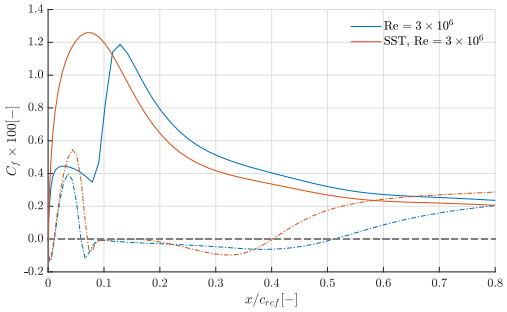

(d) $\mathrm{Re} = 3 \times 10^6$

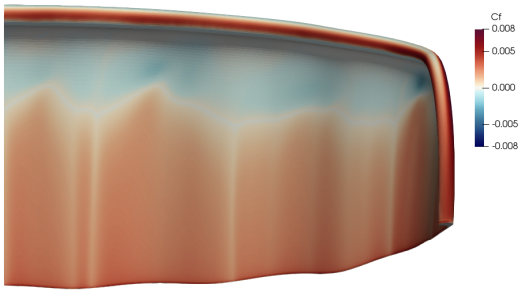

(e) $\mathrm{Re} = 10 \times 10^6$

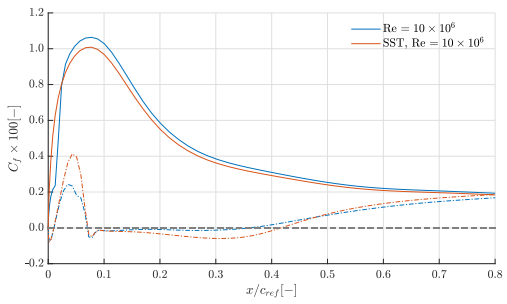

(f) $\mathrm{Re} = 10 \times 10^6$

Figure 5.21: Skin friction coefficient at the pressure side of the kite, computed without transition modelling (a, c, e), and corresponding graph over a chordwise cross section near the symmetry plane for the top (solid line) and bottom (dashed line) surface (b, d, f), computed for various Reynolds numbers at 12° angle of attack.

5.3 Comparison with literature

In this section the results obtained for LEI V3A kite using the $\gamma - \widetilde{\mathrm{Re}}_{\theta t}$ transition model will be compared to various numerical and experimental studies.

5.3.1 Numerical studies

The simulation setup in this thesis was based on the work of Folkersma et al [5], who conducted a similar study on a 2D LEI V3A kite airfoil. Lift and drag polars obtained for the 2D case using $\gamma - \widetilde{\mathrm{Re}}_{\theta t}$ transition model are compared to the results obtained in this work on Figure 5.22. The main differences include the magnitude of lift and drag coefficients. Increased drag and lowered lift is an expected result of extending the analysis from two to three dimensions, especially given that a kite geometry significantly deviates from an airfoil with infinite span. Folkersma indicates the following flow features on the polar curves:

1. Very early stall for $\mathrm{Re} = 1 \times 10^5$ caused by the laminar flow separation.
2. Existence of a laminar separation bubble that vanishes when Reynolds number reaches $\mathrm{Re} = 5 \times 10^6$, at which the stall angle is the highest.
3. Reduction of the maximum lift coefficient with increasing Reynolds number until $\mathrm{Re} = 20 \times 10^6$, when the majority of the boundary layer becomes turbulent.
4. Increase in the maximum lift coefficient once Reynolds number exceeds $\mathrm{Re} = 20 \times 10^6$.
5. A significant decrease in the drag coefficient at low angles of attack once Reynolds number exceeds $\mathrm{Re} = 2 \times 10^6$, due to drag crisis occurring at the pressure side of the cylindrical LE.

Although not apparent for Reynolds numbers showed on Figure 5.22, all the phenomena outlined above are also present in the current 3D analysis, as explained in Section 5.1.1. The 3D results are analogous to the 2D analysis and happen at corresponding, slightly different Reynolds numbers.

Another set of comparable data includes results obtained by Deaves [4], who conducted a similar study on a slightly different kite geometry (LEI V2 model), using the $k - \omega$ SST turbulence model. His analysis considered a full range of angles of attack (-6° to 24°) for a Reynolds number $\mathrm{Re} = 6 \times 10^6$. The results indicate a stall angle of 20°, but no sudden drop in the lift coefficient is present on the polar graph. The flow separation on the suction side is generally contained within the region from about 20% to 60% of the kite span, measuring from the symmetry to the tip. This is a different behaviour compared to the current work, where the flow separation during stall occurs near the symmetry plane. Zero-lift angle of attack for V2 was found to be equal to $\alpha_{L=0} = -3.54^\circ$, corresponding to $C_{D,L=0} = 0.0384$,

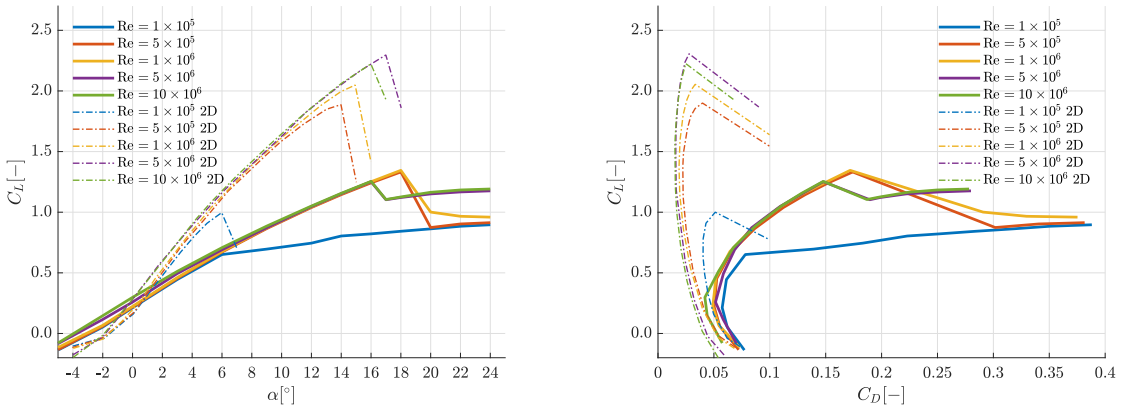

(a) **(b)**

Figure 5.22: Lift (a) and drag (b) polars for the LEI V3A kite computed for various Reynolds numbers (solid line) compared to 2D results from Folkersma et al [5] (dashed line).

while V3A displays $\alpha_{L=0} = -3.8°$ and $C_{D,L=0} = 0.065$ for $\mathrm{Re} = 5 \times 10^6$. These discrepancies could be attributed to geometry differences between V2 and V3A and the use of transition modelling, which was shown to increase the drag at low angles of attack for $\mathrm{Re} = 3 \times 10^6$ (refer to Section 5.2). Geometry differences make direct comparison to Deaves' work fairly difficult and unreliable, especially considering rather poor quality of his computational mesh that led to high amplitude variations of the results during the simulation time.

Multiple models exist that attempt to characterise the whole pumping kite power system through dynamic modelling of the wing, bridle lines, control unit and tether during traction and retraction phases. They often use certain assumed force coefficients that are based on experimental data as model inputs. Table 5.1 presents a comparison between traction phase force coefficients characterising various dynamic models and simulation results obtained in this work.

Van der Vlugt et al (2014) model [97] uses measurement data obtained by Ruppert [13] for LEI V2 kite as input to their power estimation model. Van der Vlugt et al (2019) [20] estimated force coefficients as time averages over traction and retraction phases obtained from two experimental data sets. Typical aerodynamic properties of a kite power system were used by Faggiani and Schmehl [11] as inputs to a pumping kite wind park model. Fechner et al [22] developed a dynamic model of a pumping kite power system and calibrated it to experimental tether force and power production data. Force coefficients in Table 5.1 represent their model output for a discretised tether model and simulated pumping cycle Sim. II.

The table also shows force coefficients obtained using the $\gamma - \widetilde{\mathrm{Re}}_{\theta t}$ model for $\mathrm{Re} = 3 \times 10^6$, taking $\alpha = 6°$ and $\alpha = 16°$ as upper and lower limits of the angle of attack during traction phase. The average lift coefficient within that range, after including the parasite drag of

Study	C_L	C_D	L/D
van der Vlugt et al (2014) [97]	1.0	0.2	5.0
Fechner et al (2015) [22] - Sim. II	0.98	0.21	4.64
Faggiani and Schmehl (2018) [11]	0.8	0.2	4.0
van der Vlugt et al (2019) [20]	0.59	0.15	3.6
V3A at $\alpha = 6°$	0.69	0.069	10.0
V3A at $\alpha = 16°$	1.253	0.148	8.5
V3A average between $\alpha = 6°$ and $16°$	1.00	0.109	9.17
V3A average with estimated parasite drag $C_{Dp} = 0.117$	1.00	0.226	4.42
V3A average with estimated parasite drag $C_{Dp} = 0.117$, $k-\omega$ SST	0.968	0.218	4.43

Table 5.1: Dynamic kite power system model parameters comparison to LEI V3A simulation results for $\mathrm{Re} = 3 \times 10^6$.

bridle lines, lies within 2% of values estimated by van der Vlugt et al [97] and Fechner et al [22]. The drag coefficient deviation is higher – up to 13%. The estimates of van der Vlugt et al [20] and Faggiani and Schmehl [11] appear to be more conservative regarding the lift coefficient magnitude. Computed lift-to-drag ratio $L/D = 4.42$ lies in between the values used in the numerical models. Average force coefficient values obtained without transition modelling are both about 3.5% lower than with transition modelling, resulting in a very similar lift-to-drag ratio $L/D = 4.43$.

To calculate the parasite drag coefficient, bridle lines drag force is estimated by the following formula obtained from [14]:

$$D_{bridle} = \frac{1}{2}\rho U_n^2 A_{eff} C_{Dcyl}, \tag{5.3}$$

where U_n is the velocity component normal to the bridle line system, assumed equal to the freestream velocity for all angles of attack. C_{Dcyl} is the drag coefficient of a cylinder, assumed to be equal to 1 in given flow regime.

A_{eff} is the effective area of bridle line system which is estimated by $A_{eff} = L_{tot}d$, with $L_{tot} = 95.726m$ being the total length of the V3A bridle line system. d denotes the diameter of a bridle line. In this analysis it is set as $d = 2.5mm$, which is a standard bridle diameter for similarly sized AWE systems. The contribution to overall drag coefficient of the kite can then be calculated as follows:

$$C_{Dbridle} = \frac{2D_{bridle}}{\rho U_\infty^2 A_{ref}} = 0.117, \tag{5.4}$$

which will further be referred to as parasite drag, $C_{Dp} = C_{Dbridle} = 0.117$. The drag contribution of the KCU is assumed to be negligible.

5.3.2 Experimental studies

Oehler et al [6] developed an experimental setup utilising in-situ flow measurements to characterize LEI V3A kite aerodynamics during traction and retraction phases. Measured data set consists of a large range of lift and drag values for various angles of attack and power settings. Figure 5.23 shows lift coefficient variation for a range of angles of attack isolated for the traction phase, when the kite deformation is limited. The data points represent values averaged for all flight conditions with given heading. There is a large difference in lift slope for kite going upwards and downwards. Oehler et al [6] explain the steep lift slope for downward movement of the kite by an increasing camber and enlargement of the wing surface area for higher angles of attack.

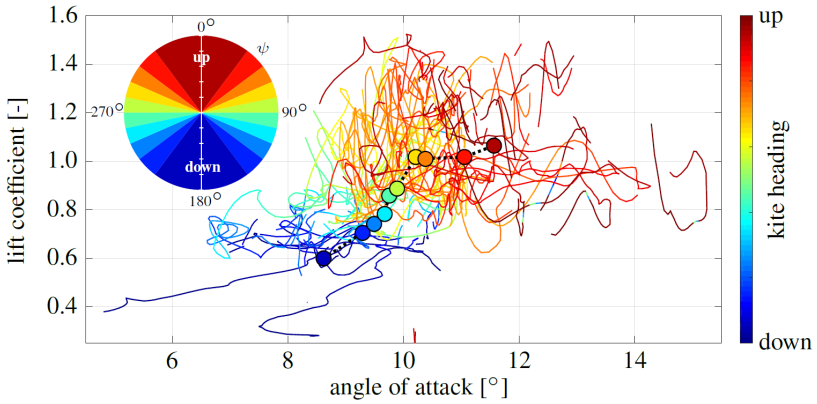

Figure 5.23: Lift coefficient for various angles of attack at constant power setting $u_p = 1$, coloured by kite heading, as measured by Oehler et al [6].

Constant power setting corresponds to the assumptions made for the analysis in this work. Figure 5.24 presents comparison of the numerical results obtained for $\mathrm{Re} = 3 \times 10^6$ and the experimental lift curve. There is a big discrepancy between data points for wing flying downwards and the simulated lift polar, while the data for wing flying upwards matches numerical results fairly well. During traction phase, the kite flies in a figure of eight, as shown on Figure 5.25. Due to the geometry of such a flight path, the kite experiences steadier loads with no centripetal forces while flying up. Flight downwards occurs primarily while it is being steered on a circular path. Steering manoeuvrers decrease lift-to-drag ratio [6], and are much more dynamic than flight in a straight line, introducing additional forces and structural deformations. Numerical analysis of Mutiny V2 kite [57] showed that kite deformation while turning can cause up to 20% lift reduction, without even accounting for the aeroelastic effects. Although kite power setting stays at unity during flight downwards, the assumption of limited kite deformation in that condition is not necessarily valid, as steering inputs inherently prompt kite deformation [65]. As such, only the data points representing kite heading up are directly comparable to current simulation results and those show good agreement on the lift coefficient magnitude for angle of attack between 10° and 12°.

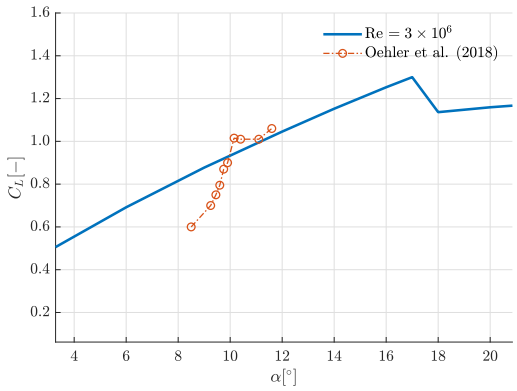

Figure 5.24: Computed lift coefficient for various angles of attack compared to the experimental data at constant power setting $u_p = 1$, as measured by Oehler et al [6].

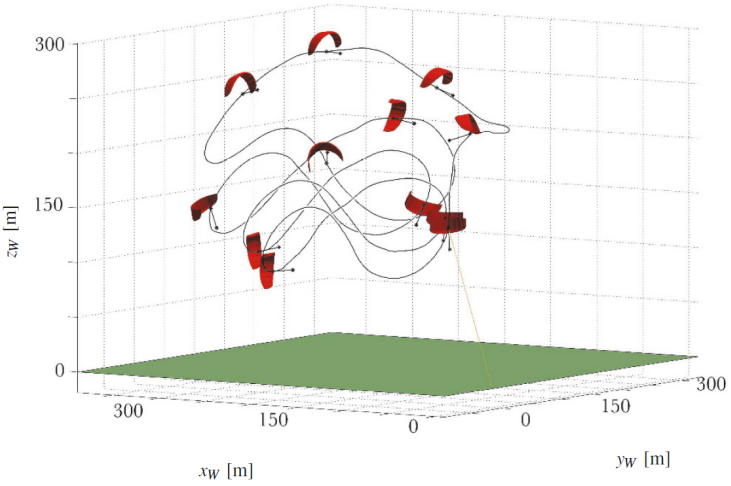

Figure 5.25: Kite trajectory and orientation for a pumping cycle, measured by van der Vlugt et al [97].

Figure 5.26 presents a comparison of experimental lift-to-drag ratio, corresponding values used in two numerical models, as well as results obtained in this work for $\mathrm{Re} = 3 \times 10^6$. Parasite drag is assumed to be constant for all angles of attack, hence the lift-to-drag ratio L/D can be calculated by:

$$L/D(\alpha) = \frac{C_L(\alpha)}{C_D(\alpha) + C_{Dp}}, \tag{5.5}$$

with $C_{Dp} = 0.117$, as estimated in the previous section.

Correlations of Ruppert [13] are based on the experimental data sets for LEI V2 and LEI V5 Hydra kites and have been adjusted based on theory and experience. Fechner et al [23]

established their lift and drag polars by adjusting 2D airfoil data to fit 3D LEI kite aerodynamics. Experimental data points obtained by Oehler et al [6] have been filtered to exclude data points associated with strong steering input. Angle of attack range of $-7°$ to $3°$ represents the retraction phase, while $7°$ to $15°$ indicate the traction phase. During retraction phase the kite experiences low aerodynamic loads and undergoes severe deformation, which is beyond the scope of this work. All models overestimate lift-to-drag ratio for the traction phase, compared to the experimental data from Oehler et al [6]. The difference becomes significant at higher angles of attack, $12°$ to $15°$, where the simulation results for $\mathrm{Re} = 3 \times 10^6$ are up to 30% higher than the experimental L/D. The trends are also different, as experimental L/D decreases with angle of attack increase from $12°$ to $15°$, while numerical L/D increases until $\alpha = 17°$. Arguably, this may not be a reliable comparison as the number of experimental data points for such angles of attack is rather scarce. For the most common flight conditions, $\alpha = 8°$ to $\alpha = 12°$, the simulation results slightly overestimate experimental measurements and show better agreement than other numerical models.

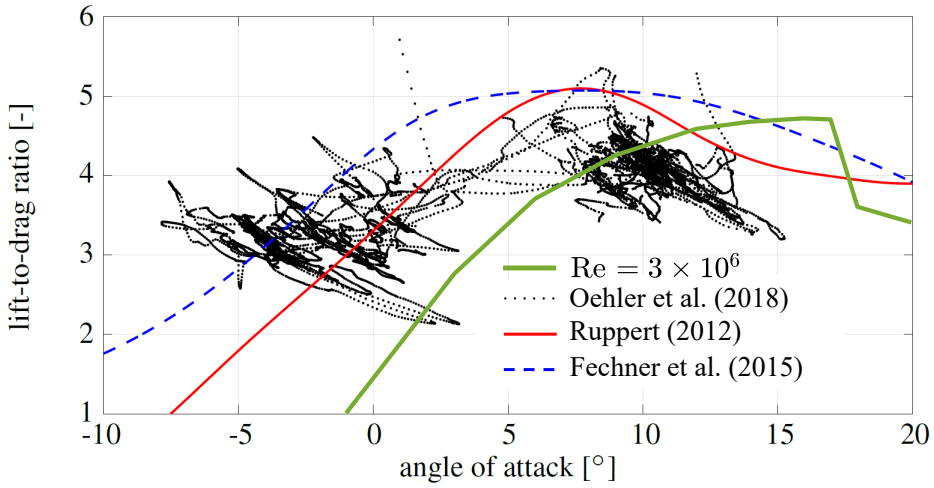

Figure 5.26: Lift-to-drag ratio comparison between different models and experimental measurements.

Chapter 6

Conclusions and Recommendations

Designing a pumping kite power system is a complex process involving numerous variables, such as cycle efficiency, tether forces and lift-to-drag ratio. Thorough understanding of the kite structural and aerodynamic properties is crucial to reduce uncertainties in the design process. Within this context, the aerodynamic analysis of energy generating kites at high Reynolds numbers poses itself a significant challenge for the following reasons. During each pumping cycle, the kite experiences persistent regions of flow separation, which combined with the bowed shape of the kite and its low aspect ratio cause multiple 3D flow phenomena. In the present work, the LEI V3A kite aerodynamics have been analysed for various Reynolds numbers and angles of attack using CFD. The kite geometry is assumed to be fixed and representative of the traction phase of the energy generation cycle. The effect of transition modelling was determined and the results have been compared with several numerical and experimental studies.

6.1 Conclusions

LEI kite aerodynamics have been evaluated for a rigid geometry using steady-state RANS solver simpleFoam within the open source CFD toolbox OpenFOAM. The computational mesh has been generated using Pointwise. The $\gamma - \widetilde{\mathrm{R}}\mathrm{e}_{\theta t}$ transition model, a modified version of the $k - \omega$ SST turbulence model, has been used to improve the accuracy of the results at low Reynolds numbers and to assess the significance of transition at high Reynolds numbers. Obtained force coefficients for a range of angles of attack have been compared with the values used in existing numerical models and measurements from experiments.

The methodology for mesh generation and sensitivity study is outlined in Chapter 4. The meshing process proved to be a challenging task, as the bowed shape of the kite prompted

use of hybrid meshing approach, which does not always yield satisfactory mesh quality. Pointwise T-Rex meshing algorithm was found to provide robust boundary layer cells extrusion with good quality at the interface of structured and unstructured regions of the computational domain. Simulation settings have been adapted from Folkersma et al [5] 2D cases and extended to three dimensions. The presented choice of numerical schemes and solution control parameters, coupled with a rather refined mesh consisting of roughly 6 million cells, provided manageable computational times and swift convergence. Even though at certain angles of attack and Reynolds numbers transient flow behaviour has been observed in the simulation residuals, the resultant lift and drag coefficients remained very stable throughout the simulation time. The influence of mesh resolution, growth ratio of the boundary layer cells and boundary conditions on the integral force coefficients was determined to be negligible.

The aerodynamic performance of the LEI V3A kite is presented in Chapter 5. Considered Reynolds numbers ranged from 10^5 to 15×10^6, while the angle of attack was varied from $-5°$ and $24°$. It was shown that at low Reynolds numbers, laminar separation occurs at both suction and pressure sides. A laminar separation bubble formed on the suction side for Reynolds numbers up to $\mathrm{Re} = 1 \times 10^6$. Above $\mathrm{Re} = 10 \times 10^6$, the transition occurs within 3% of the chord and the flow field can be approximated as fully turbulent. For lower Reynolds numbers, a significant portion of the boundary layer is laminar which increases the stall angle of attack. The phenomenon of drag crisis on the pressure side of the cylindrical leading edge has been observed for Reynolds numbers above $\mathrm{Re} = 10 \times 10^6$, delaying the flow separation. This results in reduced size of the recirculation zone behind the leading edge and decreased overall drag at low angles of attack. The aerodynamic efficiency across all angles of attack is the highest for $\mathrm{Re} = 15 \times 10^6$.

The investigation of the 3D flow effects indicated a large amount of cross flow across the span of the kite. The flow above the kite generally tends inwards, while the flow below tends outwards. This forms a region of high magnitude vorticity in the wake of the kite. The size of the recirculation zone behind the cylindrical leading edge was found to be varying across the kite span, which was linked to the existence of locally varying direction of the cross flow on the pressure side. The flow separation zone on the suction side in stall conditions reduces in size for increasing Reynolds numbers, which can be associated with decreasing drop of the lift cofficient once the critical angle of attack is exceeded.

Based on the comparison of the results obtained with and without transition modelling, it was determined that taking flow transition into account is required to accurately predict the stall angle of attack for Reynolds numbers up to at least $\mathrm{Re} = 3 \times 10^6$. Regular $k - \omega$ SST turbulence model was also found to slightly underpredict the drag coefficient prior to the stall angle for $\mathrm{Re} = 3 \times 10^6$. It also fails to capture the laminar separation bubble on the suction side at any Reynolds number. However, a comparison of the skin friction coefficient across a chordwise cross section close to the symmetry plane revealed that $k-\omega$ SST is capable of distinguishing laminar and turbulent separation off the pressure side of

the cylindrical leading edge with very good accuracy. The agreement was worse for $\mathrm{Re} = 3 \times 10^6$, where regions experiencing both laminar and turbulent separation are present.

The results have been compared to several numerical and experimental data sets. Various flow features identified by Folkersma et al [5] during a numerical analysis of the LEI V3A airfoil were also found in the 3D analysis conducted in this work and occur at analogous Reynolds numbers. Computed lift and drag coefficients, averaged for angles of attack common for the traction phase, remain within the range of typical values used as input to various numerical kite power system models. Extensive experimental studies are scarce and typically require measurements gathered in-situ during crosswind manoeuvrers to obtain any information about the local flow conditions. Not fully controlled nature of such experiments makes comparison with numerical results fairly difficult. Data gathered by Oehler et al [6] provided a good reference, thanks to filtering out data points characterised by either high steering input or power setting lower than 1. Computed lift coefficients are in very good agreement within the narrow range of 10° to 12° angle of attack. For angles 8° to 10° the agreement significantly diminishes, which may be caused by these data points representing kite heading downwards and experiencing deformation. Computed lift-to-drag ratio slightly overestimates results of Oehler et al [6], but shows better agreement than other numerical models. Any data related to the retraction phase of the kite system was not considered in this analysis.

6.2 Recommendations

Several recommendations can be formulated given the results obtained in this thesis, regarding the numerical setup, results validation and future aerodynamic analyses.

Although the computational mesh used in this work is of high quality overall, some low quality cells still exist and may introduce unquantifiable errors. It can be argued that the accuracy loss due to the assumption of steady-state and rigid geometry outweighs the numerical errors related to cell quality. Nevertheless, numerous meshing methods exist that were not investigated, such as overset or high order meshing, that may help reduce grid-related errors and improve convergence even further. Those methods can be very powerful once more complex geometries are analysed.

The biggest geometric simplification made to the current model is the removal of the chordwise struts, which are assumed to have a constraining effect on the cross flow at the pressure side of the kite. It was shown that cross flow can influence the size of the recirculation zone and, as a result, alter the drag coefficient. The drag contribution of other parts of the kite power system, such as bridle lines, was very roughly estimated. Quantification of the effect of the struts on the overall flow solution, as well as more precise formulation for the parasite drag of the whole system is left for future work.

Traditional way of setting the boundary conditions in RANS simulations is not very intuitive, as turbulence quantities prescribed at the inlet very quickly decay to values very close to 0. As shown in Section 4.4, the magnitude of turbulence quantities at the inlet had negligible effect on the flow solution in the centre of the domain. Spalart et al [98] proposed to prescribe floor values for the turbulence quantities across the whole domain. Although mostly useful for wind tunnel simulations to achieve certain turbulence intensity, this method can be applied to kite aerodynamics, provided experimental characterisation of these quantities is available.

Lack of reference data for validation of kite aerodynamics, as shown during the literature review, makes it difficult to thoroughly assess the quality of numerical results. Having access to more refined data about the local flow quantities around the kite during energy generation cycle should improve the numerical results validation process.

The impact of transition modelling on the LEI kite aerodynamics has been assessed both in this thesis and by Folkersma et al [5]. The results in both works are fairly similar, which is not very surprising, given that the same transition model was used. Some uncertainty still surrounds the stall angle behaviour for increasing Reynolds number, which was not found in other references. Using another popular, easy to implement transition model such as $k-k_L-\omega$ by Walters and Cokljat [77] can be used to compare the results for different models, verifying the stall angle behaviour. Conducting an analogous wind tunnel experiment to analyse the flow field around a rigid kite geometry at various Reynolds numbers should also be possible, as scaling the structural properties would not be necessary, and it would allow to increase confidence in numerical results.

The assumptions leading to the aerodynamic analysis in this work are quite specific and disregard certain flow conditions commonly encountered by the kite during the energy generation cycle. Variations in the sideslip angle are not considered, although were observed to vary by up to $\pm 10^{\circ}$ during traction phase. The simulations in this thesis are steady-state, which is not always the case during traction phase. Unsteady RANS should improve the fidelity of the results and provide insight on the transient flow features.

The results from this work cannot be used to represent the retraction phase of the kite energy generation cycle, since the assumption of rigid geometry is no longer valid. During the retraction phase, the kite is subjected to much lower aerodynamic loading, which prompts severe deformation. Since a kite is a lightweight, flexible structure, very strong coupling between the aerodynamic loads and structural dynamics forms an intricate aeroelastic system. There are two ways this problem can be tackled. An experimental study of in-flight kite deformation can be conducted and resultant kite shapes can be analysed using RANS. Additionally, a FSI solver can be developed to perform a real-time aeroelastic simulation of the full 3D kite geometry. Both of these approaches would be very challenging, while 3D FSI over a large computational grid is also extremely computationally expensive. A much more simplified geometry would likely be required.

Bibliography

[1] L. C. Archer and K. Caldeira. Global Assessment of High-Altitude Wind Power. *Energies*, 2(2), 2009.

[2] M. L. Loyd. Crosswind kite power. *Journal of Energy*, 4:106–111, 06 1980.

[3] J. Breukels. *An engineering methodology for kite design*. PhD thesis, Delft University of Technology, 2011.

[4] M. Deaves. An Investigation of the Non-Linear 3D Flow Effects Relevant for Leading Edge Inflatable Kites. Master's thesis, Delft University of Technology, 2015.

[5] M. Folkersma, R. Schmehl, and A. Viré. Boundary layer transition modeling on leading edge inflatable kite airfoils. *Wind Energy*, 22:908–921, 2019.

[6] J. Oehler and R. Schmehl. Aerodynamic characterization of a soft kite by in situ flow measurement. *Wind Energy Science*, 4(1):1–21, 2019.

[7] M. Diehl, U. Ahrens, and R. Schmehl. *Airborne Wind Energy*. Springer, Berlin Heidelberg, 2014.

[8] R. Schmehl. *Airborne Wind Energy: Advances in Technology Development and Research*. Springer, Singapore, 2018.

[9] M. Z. Jacobson and C. L. Archer. Saturation wind power potential and its implications for wind energy. *Proc Natl Acad Sci USA*, 109(39):15679–84, 2012.

[10] K. Marvel, B. Kravitz, and K. Caldeira. Geophysical limits to global wind power. *Nature Climate Change*, 3:118, 2012.

[11] P. Faggiani and R. Schmehl. *Design and Economics of a Pumping Kite Wind Park*, in R. Schmehl, ed. *Airborne Wind Energy: Advances in Technology Development and Research*, Section 16, pages 391–411. Springer, Singapore, 2018.

[12] U. Zillmann and P. Bechtle. *Emergence and Economic Dimension of Airborne Wind Energy*, in R. Schmehl, ed. *Airborne Wind Energy: Advances in Technology Development and Research*, Section 1, pages 1–25. Springer, Singapore, 2018.

[13] M. B. Ruppert. Development and validation of a real time pumping kite model. Master's thesis, Delft University of Technology, 2012.

[14] S. Dunker. *Tether and Bridle Line Drag in Airborne Wind Energy Applications*, in R. Schmehl, ed. *Airborne Wind Energy: Advances in Technology Development and Research*, Section 2, pages 29–56. Springer, Singapore, 2018.

[15] M. Diehl. *Airborne Wind Energy: Basic Concepts and Physical Foundations*, in R. Schmehl, ed. *Airborne Wind Energy*, Section 1, pages 3–22. Springer, Berlin Heidelberg, 2014.

[16] I. Argatov, P. Rautakorpi, and R. Silvennoinen. Estimation of the mechanical energy output of the kite wind generator. *Renewable Energy*, 34(6):1525–1532, 2009.

[17] J. Berens. Dynamic nonlinear aeroelastic behaviour of flexible wings in an airflow. Master's thesis, Delft University of Technology, 2015.

[18] R. Schmel and M. Folkersma. D1.2 improved kite design. Report, 2018.

[19] H. A. Bosch. Finite element analysis of a kite for power generation. Master's thesis, Delft University of Technology, 2012.

[20] R. van der Vlugt, A. Bley, M. Noom, and R. Schmehl. Quasi-steady model of a pumping kite power system. *Renewable Energy*, 131:83–99, 2019.

[21] J. Oehler. Measuring apparent flow vector on a flexible wing kite. Master's thesis, University of Stuttgart, 2017.

[22] U. Fechner, R. van der Vlugt, E. Schreuder, and R. Schmehl. Dynamic model of a pumping kite power system. *Renewable Energy*, 83:705–716, 2015.

[23] U. Fechner and R. Schmehl. *Model-Based Efficiency Analysis of Wind Power Conversion by a Pumping Kite Power System*, in R. Schmehl, ed. *Airborne Wind Energy*, Section 14, pages 249–269. Springer, Berlin Heidelberg, 2014.

[24] T. E. Sweeney. Exploratory sail wing research at princeton. technical report 578. Report, Princeton University, 1961.

[25] M. Fink. *Full-scale investigation of the aerodynamic characteristics of a sailwing of aspect ratio 5.9.* NASA technical note ; D-5047. NASA, Washington, 1969.

[26] E. Achenbach. Distribution of local pressure and skin friction around a circular cylinder in cross-flow up to Re $= 5 \times 10^6$. *Journal of Fluid Mechanics*, 34(4):625–639, 1968.

[27] P. Bot, M. Rabaud, G. Thomas, A. Lombardi, and C. Lebret. Sharp transition in the lift force of a fluid flowing past nonsymmetrical obstacles: Evidence for a lift crisis in the drag crisis regime. *Physical review letters*, 117(23):234501, 2016.

[28] J. Katz and A. Plotkin. *Low-Speed Aerodynamics*. Cambridge University Press, Cambridge, 2001.

[29] B. Thwaites. The aerodynamic theory of sails. i. two-dimensional sails. *Proceedings of the Royal Society of London. Series A, Mathematical and Physical Sciences*, 261(1306):402–422, 1961.

[30] B. G. Newman. Aerodynamic theory for membranes and sails. *Progress in Aerospace Sciences*, 24(1):1–27, 1987.

[31] R. Mendenhall, J. Nielsen, and S. Spangler. Review of methods for predicting the aerodynamic characteristics of parawings. *Journal of Aircraft*, 5(6):597–605, 1968.

[32] S. P. Fiddes and J. H. Gaydon. A new vortex lattice method for calculating the flow past yacht sails. *Journal of Wind Engineering and Industrial Aerodynamics*, 63(1):35–59, 1996.

[33] O. Lorillu, R. Weber, and J. Hureau. Numerical and experimental analysis of two-dimensional separated flows over a flexible sail. *Journal of Fluid Mechanics*, 466(1):319–341, 2002.

[34] K. Graf, A. Hoeve, and S. Watin. Comparison of full 3D-RANS simulations with 2D-RANS/lifting line method calculations for the flow analysis of rigid wings for high performance multihulls. *Ocean Engineering*, 90:49–61, 2014.

[35] K. Vimalakanthan, M. Caboni, J. G. Schepers, E. Pechenik, and P. Williams. Aerodynamic analysis of Ampyx's airborne wind energy system. *Journal of Physics: Conference Series*, 1037:062008, 2018.

[36] M. Gaunaa, P. F. Paralta Carqueija, P. M. Réthoré, and N. N. Sørensen. A computationally efficient method for determining the aerodynamic performance of kites for wind energy applications. In *Proceedings*. European Wind Energy Association (EWEA), 2011.

[37] R. C. Leuthold. Multiple-wake vortex lattice method for membrane wing kites. Master's thesis, Delft University of Technology, 2015.

[38] P. S. M. Mandru. Investigation on inviscid flow methods for 2D LEI tube kite. Master's thesis, Delft University of Technology, 2018.

[39] R. Smith. *A viscous flow based membrane wing model*. PhD thesis, University of Florida, 1994.

[40] A. N. Kolmogorov. The local structure of turbulence in incompressible viscous fluid for very large reynolds numbers. *Proceedings: Mathematical and Physical Sciences*, 434(1890):9–13, 1941.

[41] T. Coudou. Numerical modeling of inflatable airborne wind energy systems. Master's thesis, Faculté polytechnique de Mons, 2017.

[42] Joel H. Ferziger and M. Perić. *Computational methods for fluid dynamics*. Springer, Berlin, 3rd, rev. ed. edition, 2002.

[43] M. Lee and R. D. Moser. Direct numerical simulation of turbulent channel flow up to $\mathrm{Re}_\tau \approx 5200$. *Journal of Fluid Mechanics*, 774:395–415, 2015.

[44] M. Lee, N. Malaya, and R. D. Moser. Petascale direct numerical simulation of turbulent channel flow on up to 786k cores. In *Proceedings of the International Conference on High Performance Computing, Networking, Storage and Analysis*, pages 1–11, 2503298. ACM.

[45] W. P. Jones and B. E. Launder. The prediction of laminarization with a two-equation model of turbulence. *International Journal of Heat and Mass Transfer*, 15(2):301–314, 1972.

[46] B. E. Launder and D. B. Spalding. The numerical computation of turbulent flows. *Computer Methods in Applied Mechanics and Engineering*, 3(2):269–289, 1974.

[47] M. Kheiri, F. Bourgault, V. Saberi Nasrabad, and S. Victor. On the aerodynamic performance of crosswind kite power systems. *Journal of Wind Engineering and Industrial Aerodynamics*, 181:1–13, 2018.

[48] S. Collie, M. Gerritsen, and M. O'Sullivan. Numerical simulation of the turbulent flow past upwind yacht sails. *Journal of Wind Engineering and Industrial Aerodynamics*, 91(2):185–197, 2002.

[49] D. C. Wilcox. Reassessment of the scale-determining equation for advanced turbulence models. *AIAA Journal*, 26(11):1299–1310, 1988.

[50] F. Menter. *Improved two-equation k - [omega] turbulence models for aerodynamic flows*. NASA technical memorandum 103975. National Aeronautics and Space Administration, Ames Research Center, Moffett Field, California, 1992.

[51] J. Johansen and J. N. Sørensen. Prediction of laminar/turbulent transition in airfoil flows. *Journal of Aircraft*, 36(4):731–734, 1999.

[52] R. Smith and W. Shyy. Computation of aerodynamic coefficients for a flexible two-dimensional membrane wing in turbulent flow. *ASME-PUBLICATIONS-FED*, 234:3–10, 1995.

[53] R. Smith and W. Shyy. Computation of aerodynamic coefficients for a flexible membrane airfoil in turbulent flow: A comparison with classical theory. *Physics of Fluids*, 8(12):3346–3353, 1996.

[54] I. M. Viola, P. Bot, and M. Riotte. Upwind sail aerodynamics: A RANS numerical investigation validated with wind tunnel pressure measurements. *International Journal of Heat and Fluid Flow*, 39:90–101, 2013.

[55] J. Steiner. Towards the CSM-CFD modelling of membrane wings at high Reynolds numbers. Master's thesis, Delft University of Technology, 2018.

[56] A. de Wachter. Deformation and aerodynamic performance of a ram-air wing. Master's thesis, Delft University of Technology, 2008.

[57] S. Sachdeva. Impact of turning-induced shape deformations on aerodynamic performance of leading edge inflatable kites. Master's thesis, Delft University of Technology, 2017.

[58] R. B. Langtry and F. R. Menter. Correlation-based transition modeling for unstructured parallelized computational fluid dynamics codes. *AIAA Journal*, 47(12):2894–2906, 2009.

[59] G. Maneia, C. Tribuzi, D. Tordella, and M. Iovieno. Aerodynamics of a rigid curved kite wing, 2013.

[60] H. Babinsky. *Aerodynamic improvements of paraglider performance*. Fluid Dynamics and Co-located Conferences. American Institute of Aeronautics and Astronautics, 1999.

[61] G. M. Dadd, D. A. Hudson, and R. A. Shenoi. Comparison of two kite force models with experiment. *Journal of Aircraft*, 47(1):212–224, 2010.

[62] J. Hummel, D. Göhlich, and R. Schmehl. Automatic measurement and characterization of the dynamic properties of tethered membrane wings. *Wind Energy Sci.*, 4:41–55, 2019.

[63] B. Python. Methodology improvement for performance assessment of pumping kite power wing. Master's thesis, École polytechnique fédérale de Lausanne, 2017.

[64] J. Oehler, M. van Reijen, and R. Schmehl. Experimental investigation of soft kite performance during turning maneuvers. *Journal of Physics: Conference Series*, 1037:052004, 2018.

[65] M. van Reijen. The turning of kites. a quantification of known theories. Master's thesis, Delft University of Technology, 2018.

[66] S. C. Yen and Y. F. Fei. Winglet Dihedral Effect on Flow Behavior and Aerodynamic Performance of NACA0012 Wings. *Journal of Fluids Engineering*, 133(7):071302–071302–9, 2011.

[67] G. J. Walker. The role of laminar-turbulent transition in gas turbine engines: A discussion. *Journal of Turbomachinery*, 115(2):207–216, 1993.

[68] R. Mayle and A. Schulz. The path to predicting bypass transition. In *ASME. Turbo Expo: Power for Land, Sea, and Air. Volume 1: Turbomachinery*, page V001T01A065, 1996.

[69] R. E. Mayle. The role of laminar-turbulent transition in gas turbine engines. *ASME J. of Turbomachinery*, 113(4):509–537, 1991.

[70] E. Malkiel and R. Mayle. Transition in a separation bubble. *ASME J. of Turbomachinery*, 118(4):752–759, 1995.

[71] R. B. Langtry. *A correlation-based transition model using local variables for unstructured parallelized CFD codes*. PhD thesis, University of Stuttgart, 2006.

[72] R. Eymard, G. Thierry, and R. Herbin. *Finite Volume Methods*, volume 7 of *Handbook of Numerical Analysis*. 2000.

[73] S. B. Pope. *Turbulent flows*. Cambridge University Press, Cambridge ;, 2000.

[74] P. Spalart and S. Allmaras. *A One-Equation Turbulence Model for Aerodynamic Flows*, volume 439. 1992.

[75] B. E. Launder and B. I. Sharma. Application of the energy-dissipation model of turbulence to the calculation of flow near a spinning disc. *Letters in Heat and Mass Transfer*, 1(2):131–137, 1974.

[76] F. Menter, M. Kuntz, and R. B. Langtry. *Ten years of industrial experience with the SST turbulence model*. in: Hanjalic K., Nagano Y, Tummers M, eds.*Turbulence, Heat and Mass Transfer 4*. Antalya: Begell House, Inc.; 2003:625-632.

[77] D. K. Walters and D. Cokljat. A Three-Equation Eddy-Viscosity Model for Reynolds-Averaged Navier–Stokes Simulations of Transitional Flow. *Journal of Fluids Engineering*, 130(12):121401, 2008.

[78] V. Michelassi, J. Wissink, and W. Rodi. Analysis of DNS and LES of Flow in a Low Pressure Turbine Cascade with Incoming Wakes and Comparison with Experiments. *Flow, Turbulence and Combustion*, 69(3):295–329, 2002.

[79] D. C. Wilcox. Simulation of transition with a two-equation turbulence model. *AIAA Journal*, 32(2):247–255, 1994.

[80] C. L. Rumsey. Apparent transition behavior of widely-used turbulence models. *International Journal of Heat and Fluid Flow*, 28(6):1460–1471, 2007.

[81] F. Menter, R. Langtry, and S. Völker. Transition Modelling for General Purpose CFD Codes. *Flow, Turbulence and Combustion*, 77(1):277–303, 2006.

[82] J. L. van Ingen. A suggested semi-empirical method for the calculation of the boundary layer transition region. Report VTH-74, Technische Hogeschool Delft, Vliegtuigbouwkunde, 1956.

[83] A. M. O. Smith and N. Gamberoni. Transition, pressure gradient and stability theory. Report ES-26388, Douglas Aircraft Company, El Segundo Division, 1956.

[84] H. W. Stock and W. Haase. Navier-Stokes Airfoil Computations with eN Transition Prediction Including Transitional Flow Regions. *AIAA Journal*, 38(11):2059–2066, 2000.

[85] B. J. Abu-Ghannam and R. Shaw. Natural transition of boundary layers—the effects of turbulence, pressure gradient, and flow history. 22(5):213–228, 1980.

[86] F. Eulitz and K. Engel. Numerical investigation of wake interaction in a low pressure turbine. In *ASME 1998 International Gas Turbine and Aeroengine Congress and Exhibition*, volume Volume 1: Turbomachinery, V001T01A134.

[87] S. Medida and J. Baeder. *Application of the Correlation-based Gamma-Re Theta t Transition Model to the Spalart-Allmaras Turbulence Model*. Fluid Dynamics and Co-located Conferences. American Institute of Aeronautics and Astronautics, 2011.

[88] N. N. Sørensen. CFD modelling of laminar-turbulent transition for airfoils and rotors using the gamma-Re theta model. *Wind Energy*, 12(8):715–733, 2009.

[89] T-Rex hybrid meshing in Pointwise. https://www.pointwise.com/theconnector/2011-July/T-Rex-Hybrid-Meshing-Pointwise.html. Accessed: 2019-10-22.

[90] OpenFOAM Workshop 2014: Effects of grid quality on solution accuracy. https://afinemesh.files.wordpress.com/2014/07/ofw20141.pdf. Accessed: 2019-10-23.

[91] Pointwise – Examine functions. https://www.pointwise.com/doc/user-manual/examine/functions/index.html. Accessed: 2019-10-23.

[92] André Bakker, Lecture 7 – Meshing. http://www.bakker.org/dartmouth06/engs150/07-mesh.pdf. Accessed: 2019-10-23.

[93] Pointwise – T-Rex. https://www.pointwise.com/doc/user-manual/grid/solve/unstructured-blocks/t-rex.html. Accessed: 2019-10-25.

[94] OpenFOAM. https://www.openfoam.com/. Accessed: 2019-11-01.

[95] S. V. Patankar and D. B. Spalding. A calculation procedure for heat, mass and momentum transfer in three-dimensional parabolic flows. *International Journal of Heat and Mass Transfer*, 15(10):1787–1806, 1972.

[96] F. M. White. *Fluid Mechanics*. McGraw-Hill, 2003.

[97] R. van der Vlugt, J. Peschel, and R. Schmehl. *Design and Experimental Characterization of a Pumping Kite Power System*, in R. Schmehl, ed. *Airborne Wind Energy*, Section 23, pages 403–425. Springer, Berlin Heidelberg, 2014.

[98] P. Spalart and C. L. Rumsey. Effective inflow conditions for turbulence models in aerodynamic calculations. 45(10):2544–2553, 2007.

Appendix A

Kite CAD generation using Rhinoceros

The following procedure has been developed to convert SurfPlan kite geometry export to a smooth, watertight CAD model, ready for meshing in Pointwise or other similar software.

1. Import the geometry from SurfPlan to Rhinoceros 5.0.
2. Set model units to centimetres, tolerances to:
   (a) Absolute tolerance 0.00001 units.
   (b) Relative tolerance 0.1 percent.
   (c) Angle tolerance 0.1 degrees.
3. Consider half of the kite only. Do the following procedure up to a profile extending past the symmetry plane. The geometry will eventually be trimmed using a plane passing through the origin of the coordinate system.
4. Remove unnecessary features from layers containing the canopy, LE and struts (like nuts etc). See Figure A.1.
5. Duplicate required edges – canopy and LE cross section profiles:
   (a) The LE cross section profiles near the tip can be located in the layer with struts.
   (b) Make sure to also duplicate the LE and TE of the canopy surface at the tip. They will be used to generate tip geometry. See Figure A.2.
6. Join resulting polylines, so that each profile is a single polyline. LE and canopy cross sections should be kept separate.

7. Rebuild the curves with minimum number of control points (10-15) and minimum degree (3-5), while attempting to preserve the trends of original geometry. This step is crucial to achieve good LE curvature.
   (a) Plot curvature graph and ensure its smoothness.
   (b) Focus on matching correct shape of the new curve at the LE end.
   (c) For the canopy profiles near the tip degree 5-6 might be necessary.
   (d) Curvature graph of each LE cross section should be a near perfect circle.
8. For each cross section (canopy + LE curves, up to the tip) do the following:
   (a) Offset the canopy cross section by about 10 units downwards (depends on the scale of the model), in the plane of the cross section. Loft through the existing canopy profiles and use the 'Offset curve normal to the surface' option.
   (b) Make an 'Arc blend' between the two new curves to form a circular trailing edge.
   (c) Use 'Adjustable curve blend' feature to create a LE fillet on the pressure side of the airfoil. Ensure it is done in a consistent fashion.
   (d) One approach is to create a blend that originates from the LE tube at about 60 degrees and reaches the canopy curve at 20% chord. Alternatively, it is possible to find a point at 30% of curve length by making a new subcurve on top of an existing curve – it indicates normalized curve length. Set up an arc blend up to that point. See Figures A.3 and A.4.
   (e) Use tangency condition at both ends of the blend. Do not join any curves yet.
   (f) Now it is required to convert the LE cross section from a closed curve into an open curve. You can use the 'Delete sub-curve' function to delete the part of the LE cross section that would be inside the airfoil.
   (g) Join the two pressure side canopy curves (blend curve and the straight curve).
   (h) Use 'Match curve' to match the end of the pressure side fillet TO the nearest LE curve end. Use tangency conditions, average curves if necessary, do not join.
   (i) Use 'Match curve' to match the end of the suction side to the nearest LE curve end. Use constant curvature condition on the canopy curve, average curves, do not join. If resultant geometry is too distorted, consider rebuilding the original duplicated edge and matching the original geometry better. Example end result can be seen on Figure A.5.
   (j) For the last cross section (at the start of the tip), join the suction side curve with the LE half circle curve. Next, split it at the point where it meets the LE tip curve obtained in Step 5. See Figure A.6.
9. There should be now 4 curves in each cross section – suction side, half circle of the LE, pressure side, trailing edge. Rebuild the curves:
   (a) suction side and pressure side – 80 control points, degree 4.

(b) LE half circle – 12 control points, degree 5 (ensure smooth curvature and reasonable curvature at the LE/suction side curve connection).

(c) TE – 8 control points, degree 4.

10. Cross sections for the main structure loft are ready, now it is time to prepare the tip. Make a 'Loft' (normal, do not rebuild) through the suction side profiles.

11. Copy and paste the last created cross section at the tip boundary (without the trailing edge half circle). Join the copied curves.

12. Use 'Rotate 3D' function to rotate those curves in a way that they line up with the TE. Use the LE tip curve obtained in Step 5 to correctly position the rotated curves. The centre of rotation should be the point where suction or pressure side meets with TE curve. See Figures A.7 and A.8.

13. Use 'Scale 3D' and 'Rotate 3D' fuctions to align the suction side of the rotated curve with the end of the LE tip curve. Try to also match the slope of the loft from Step 10, for a smooth transition between the tip and main part of the kite. Let's call this curve the TE tip curve.

14. Use 'Sweep 1 Rail' (cross section – LE half circle of the last cross section at the tip, rail – LE tip curve).

15. Duplicate the edges of the newly created surface.

16. Delete the half circle LE curve from the TE tip curve. It is to be replaced with the duplicated edge of the swept surface created in step 14.

17. Match the TE tip curve ends with the new half circle LE curve and and the 2 LE tip curves duplicated from the swept surface created in step 14. You can split the curve near the end and use 'Match curves' to get good curvature, as well as rebuild parts of the curves with low degree and/or number of control points to smooth them out. See Figure A.9.

18. Delete the swept surface.

19. Rebuild all tip curves with degree 4 and about 80 control points.

20. Use 'Sweep 2 rails' (cross section – LE half circle of the last cross section at the tip, rails – both LE tip curves), maintain height if necessary, do not rebuild.

21. Use 'Edge curves' to create suction and pressure side surfaces of the tip. Select the curves in an order that creates a surface that originates from the right angle of the tip.

22. Delete the suction side loft created in step 10.

23. Make a 'Loft' through the suction and pressure side profiles of the main part of the kite. Start from the edges of surfaces created in Step 21 and then choose remaining cross sections. Ideally, tick 'Match start/end tangent', if it does not distort the loft too much.

24. 'Sweep 2 rails' both half circle LE and circular TE, with suction/pressure side surface edges as rails.

25. 'Sweep 2 rails' with maintain height ticked, cross section – circular TE at the start of the tip, rails – TE tip curves. This will create a circular TE at the tip and close the geometry.

26. Create a vertical plane crossing the origin to split the model and cut off what extends past the plane.

27. Optionally resize the model to normalise its dimensions against a chosen length scale.

28. Export the final surfaces in a desired format.

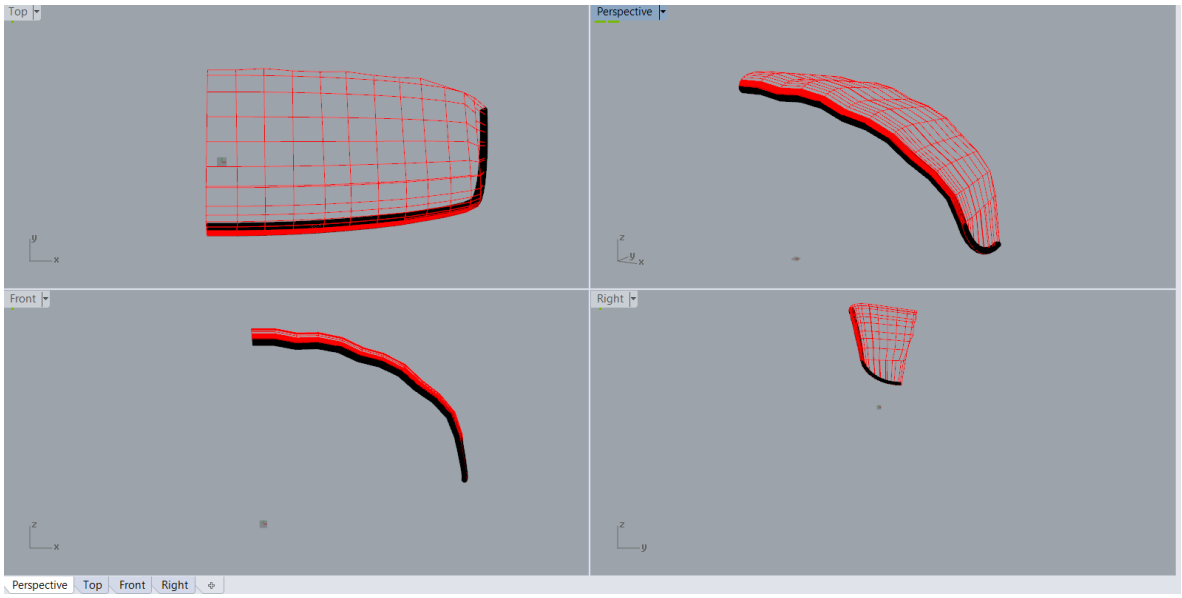

Figure A.1: Half geometry with the unnecessary elements removed.

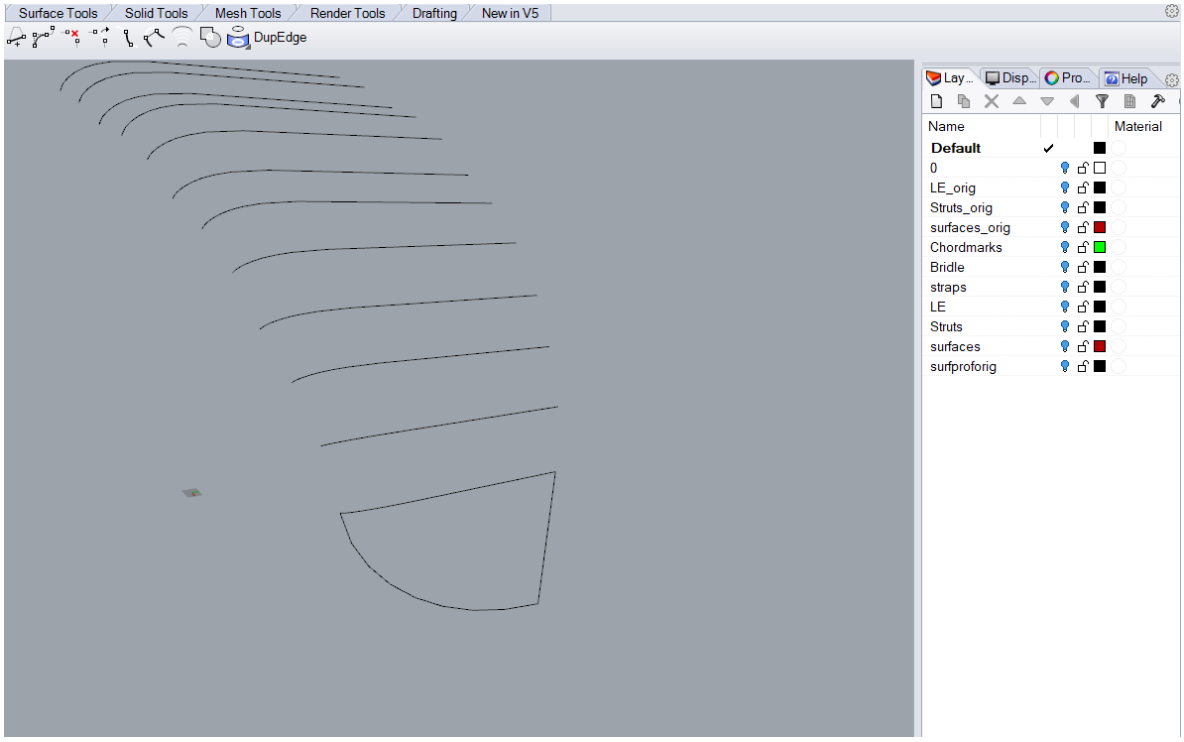

Figure A.2: Duplicated edges of the canopy.

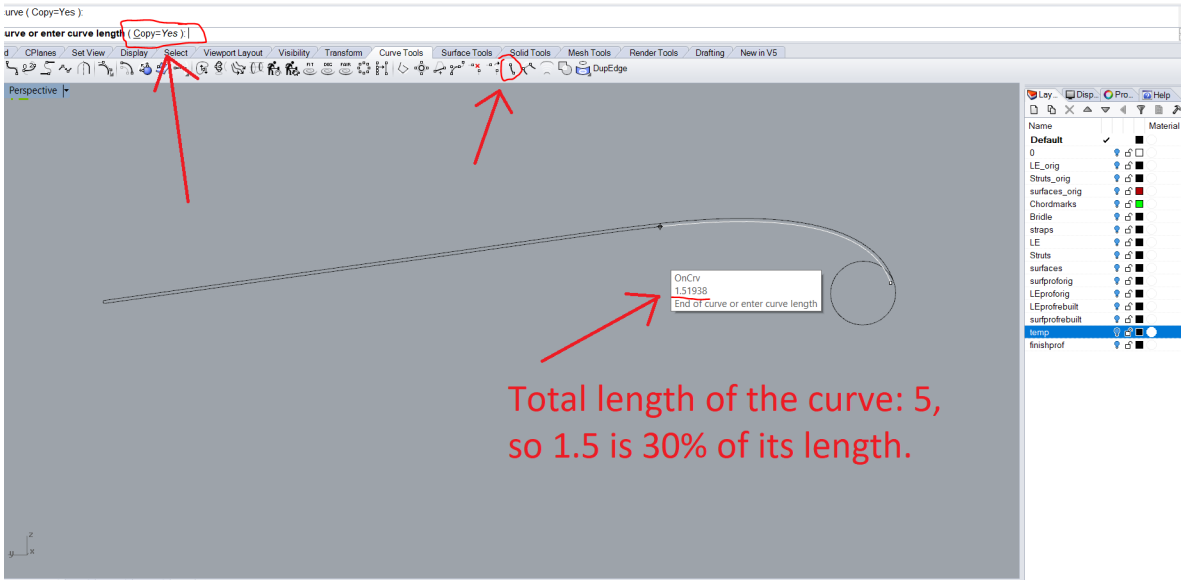

Figure A.3: 30% curve length location.

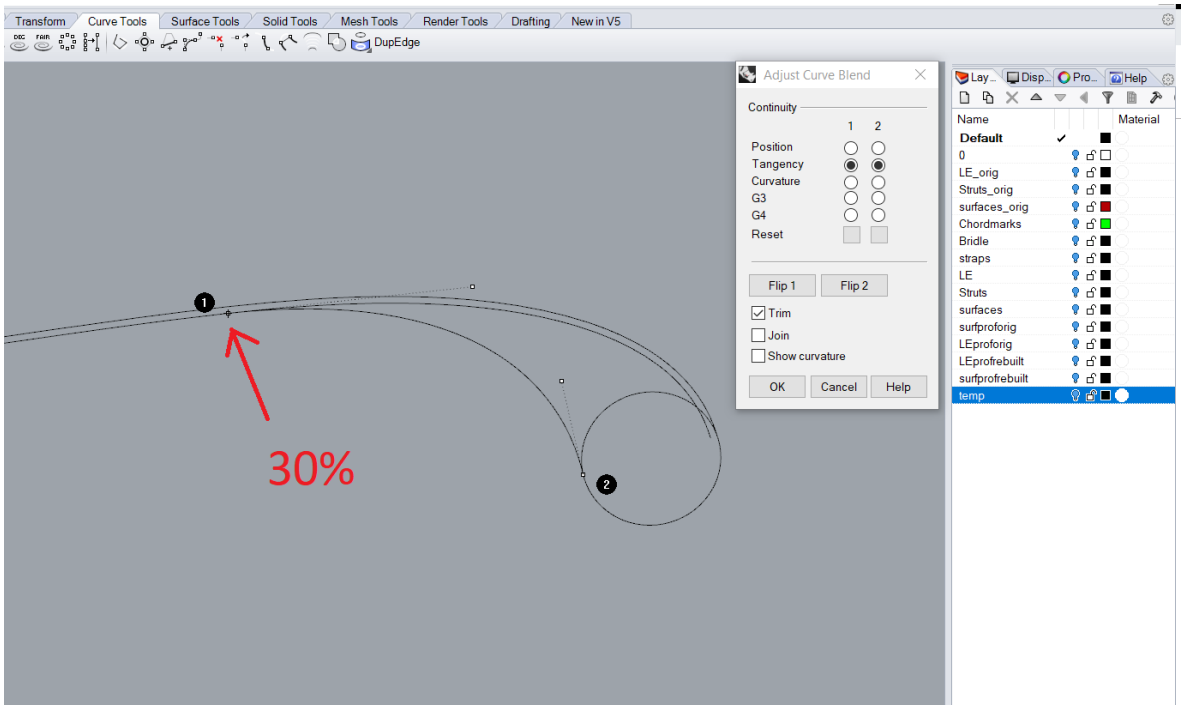

Figure A.4: Adjustable arc blend set up.

Figure A.5: Example finished cross section profile compared to the original.

Figure A.6: Profile intersection location at the tip.

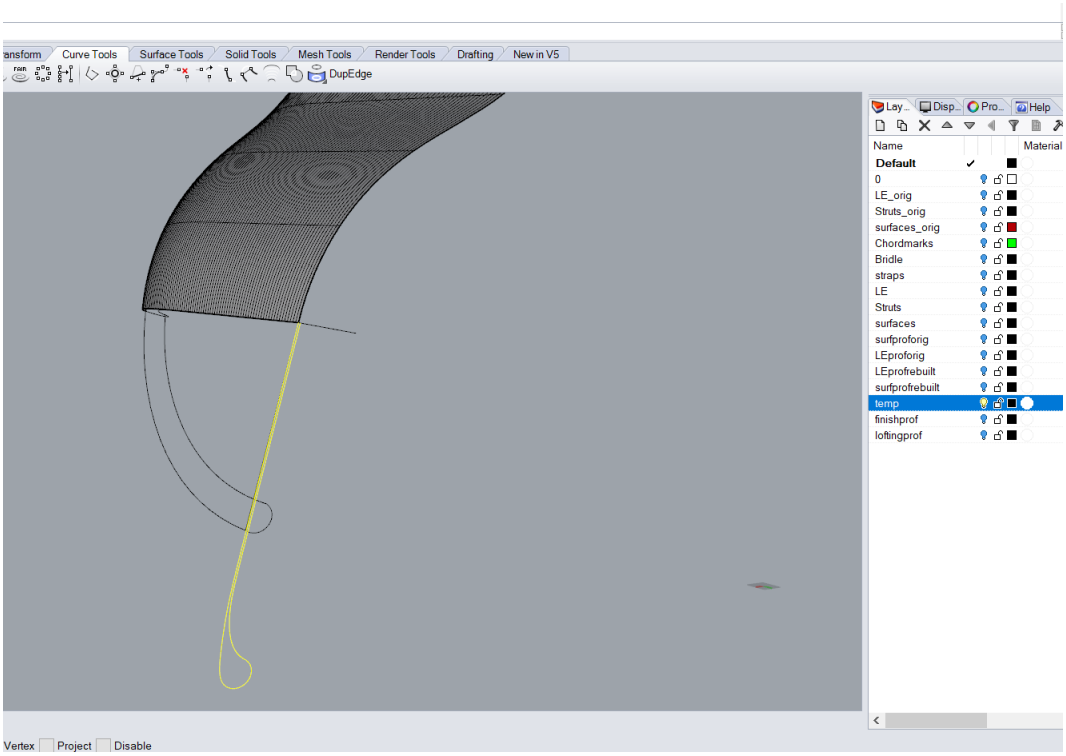

Figure A.7: Rotated cross section to build the tip.

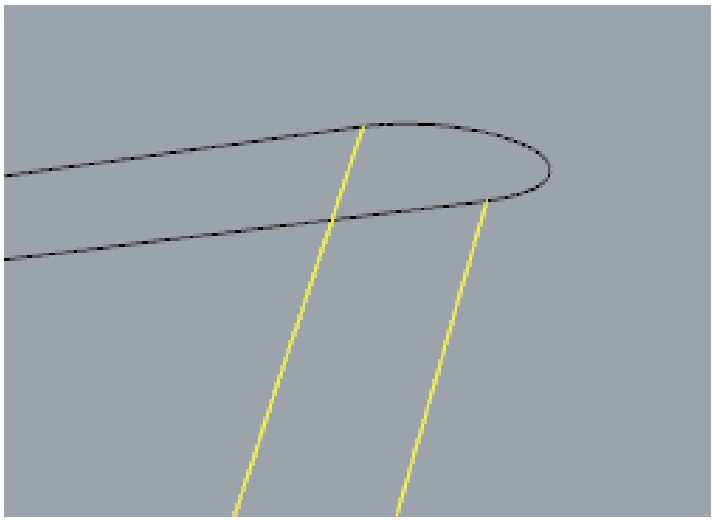

Figure A.8: Centre of rotation of the tip cross section.

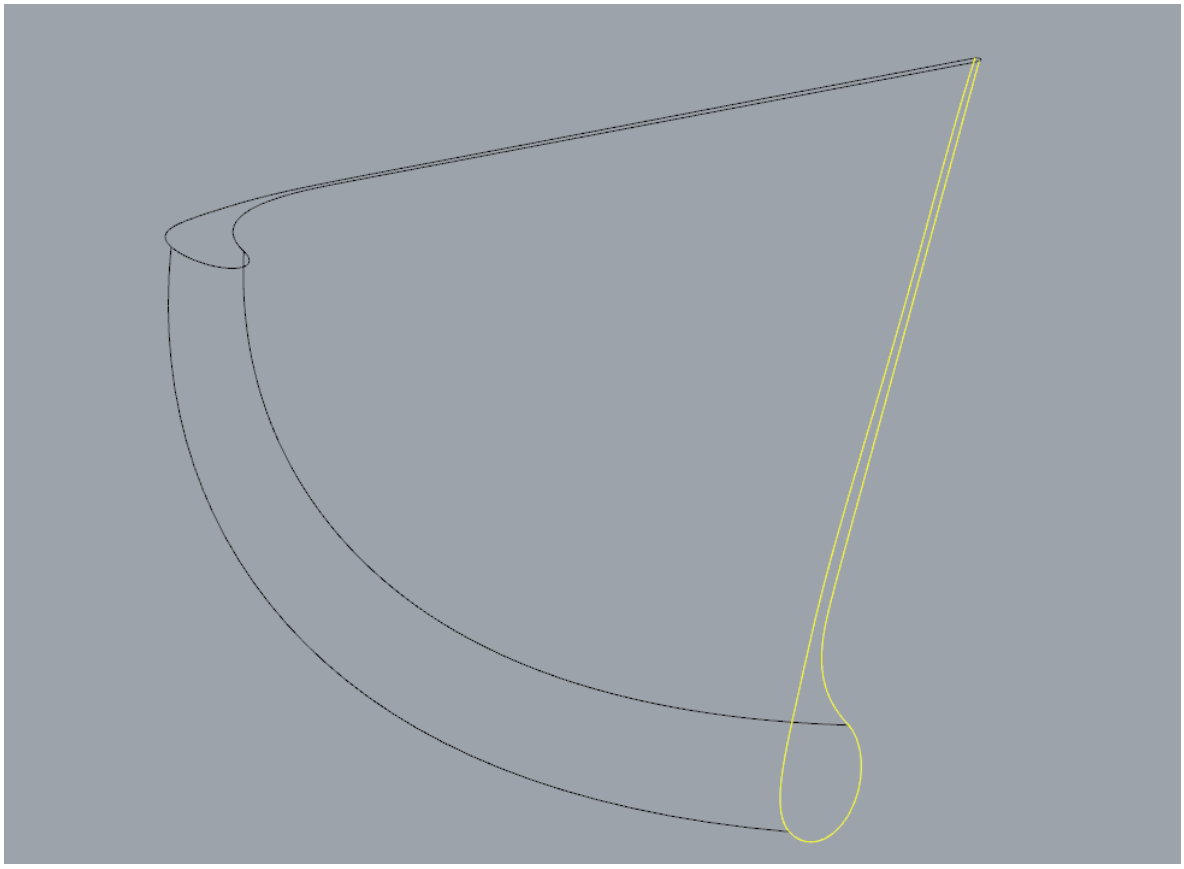

Figure A.9: Finished TE tip curve that can be used to generate the surfaces.